Journal of Advanced Ceramics
2022, **11**(1): 1–56
https://doi.org/10.1007/s40145-021-0550-6
ISSN 2226-4108
CN 10-1154/TQ

Review

Advances in ultra-high temperature ceramics, composites, and coatings

Dewei NI[a,†], Yuan CHENG[b,†], Jiaping ZHANG[c,†], Ji-Xuan LIU[d,†], Ji ZOU[e,†], Bowen CHEN[a,f], Haoyang WU[e], Hejun LI[c], Shaoming DONG[a], Jiecai HAN[b], Xinghong ZHANG[b,*], Qiangang FU[c,*], Guo-Jun ZHANG[d,*]

[a]*State Key Laboratory of High Performance Ceramics & Superfine Microstructure*, *Structural Ceramics and Composites Engineering Research Center*, *Shanghai Institute of Ceramics*, *Chinese Academy of Sciences*, *Shanghai 200050*, *China*
[b]*National Key Laboratory of Science and Technology on Advanced Composites in Special Environments*, *Center for Composite Materials and Structures*, *Harbin Institute of Technology*, *Harbin 150001*, *China*
[c]*Shaanxi Key Laboratory of Fiber Reinforced Light Composite Materials*, *Northwestern Polytechnical University*, *Xi'an 710072*, *China*
[d]*State Key Laboratory for Modification of Chemical Fibers and Polymer Materials*, *Institute of Functional Materials*, *Donghua University*, *Shanghai 201620*, *China*
[e]*State Key Laboratory of Advanced Technology for Materials Synthesis and Processing*, *Wuhan University of Technology*, *Wuhan 430070*, *China*
[f]*University of Chinese Academy of Sciences*, *Beijing 100049*, *China*

Received: September 9, 2021; Revised: October 12, 2021; Accepted: October 16, 2021

Abstract: Ultra-high temperature ceramics (UHTCs) are generally referred to the carbides, nitrides, and borides of the transition metals, with the Group IVB compounds (Zr & Hf) and TaC as the main focus. The UHTCs are endowed with ultra-high melting points, excellent mechanical properties, and ablation resistance at elevated temperatures. These unique combinations of properties make them promising materials for extremely environmental structural applications in rocket and hypersonic vehicles, particularly nozzles, leading edges, and engine components, etc. In addition to bulk UHTCs, UHTC coatings and fiber reinforced UHTC composites are extensively developed and applied to avoid the intrinsic brittleness and poor thermal shock resistance of bulk ceramics. Recently, high-entropy UHTCs are developed rapidly and attract a lot of attention as an emerging direction for ultra-high temperature materials. This review presents the state of the art of processing approaches, microstructure design and properties of UHTCs from bulk materials to composites and coatings, as well as the future directions.

† Dewei Ni, Yuan Cheng, Jiaping Zhang, Ji-Xuan Liu, and Ji Zou contributed equally to this work.
* Corresponding authors.
E-mail: G.-J. Zhang, gjzhang@dhu.edu.cn;
X. Zhang, zhangxh@hit.edu.cn;
Q. Fu, fuqiangang@nwpu.edu.cn

Keywords: ultra-high temperature ceramics (UHTCs); coatings; composites; high-entropy ultra-high temperature ceramics

1 Introduction

Ultra-high temperature ceramics (UHTCs) refer to a number of special materials which are chemically stable at ultra-high temperatures (above 2000 ℃) and in reactive atmosphere (i.e., atomic oxygen environment), usually including borides, carbides, and nitrides of transition metals, and other high-melting point compounds [1–5]. The UHTCs generally have melting points higher than 3000 ℃ and excellent oxidation ablation resistance [1–3], which can maintain non-ablative properties and structural integrity in an oxidizing environment above 1800 ℃ for longer period. This makes them very promising for applications in extreme conditions. Existing high-temperature alloy materials have poor oxidation resistance and their application temperatures are generally lower than 1200 ℃; long-term application temperature of C/SiC composites could not exceed 1650 ℃ due to the active oxidation of the SiC matrix; C/C composites begin to be oxidized sharply above 500 ℃ without a protective layer. Therefore, the previous thermal protection material system could no longer meet the needs of hypersonic vehicle thermal protection. Due to the excellent combined properties, UHTCs are considered as the candidates for a new generation of high-temperature thermal protection materials. In more specific terms, transition-metal diborides are characterized by tuneable densities (4.5–12.5 $g \cdot cm^{-3}$), moderate coefficient of thermal expansion (CTE; 6.3×10^{-6}–8.6×10^{-6} K^{-1}), high thermal conductivity (60–120 $W \cdot m^{-1} \cdot K^{-1}$), low electrical resistivity (10–30 μΩ·cm), relatively good mechanical properties, and oxidation resistance. Compared to borides, carbide-based UHTCs, such as HfC, have similar CTE, but higher electrical resistivity (109 μΩ·cm) and slightly lower mechanical properties. However, carbide-based UHTCs are easier to be oxidized at low temperatures in oxygen containing environment, limiting their application to some extent. Compared with carbides or borides, the mechanical properties of nitride-based UHTCs are lower. They normally possess high CTE (7×10^{-6}–10×10^{-6} K^{-1}) and low thermal conductivity (19–23 $W \cdot m^{-1} \cdot K^{-1}$).

1.1 History of UHTC studies

The earliest research on UHTCs can be traced back to the 1950s. HfB_2 and ZrB_2 have been attracted and used as nuclear reactor materials because of their excellent high-temperature corrosion resistance [6–8]. Incrementally, potentials of UHTCs as the high-temperature thermal protection materials have been recognized. In the 1960s and 1980s, there was an upsurge in the research relating to hypersonic aircraft in USA. In order to develop new ultra-high temperature materials, which meet the thermal protection requirements of nose cone and fuselage front edge, Air Force Materials Laboratory (AFRL) funded the ManLabs laboratory to explore the potential of ultra-high temperature ceramic materials in anti-oxidation and ablation resistance [9–13]. In the 1990s, NASA Ames Glenn Research Center further carried out systematic basic research on the mechanical properties and oxidation resistance of HfB_2–SiC and ZrB_2–SiC [14–17]. By the end of the 1990s and the beginning of the 21st century, the Ames Glenn Research Center together with Sandia National Laboratory and the Air Force Space Command, carried out flight demonstration test of the thermal protection structure of UHTCs. Although it exposed the intrinsic brittleness of UHTCs, this flight test proved the great potential of UHTCs in extreme environments, from the viewpoint of ablation resistance [18,19]. The Ames Glenn Research Center led the follow-up research, and continuously invested in the research on the strengthening and toughening technology for UHTCs.

The design and implementation of strengthening and toughening have therefore become research hotspots in the field of UHTCs. With particulate, whisker, or platelet as reinforcements, the fracture toughness of bulk UHTCs was improved to a certain extent, even though the intrinsic brittleness could not be eliminated completely. A better solution to toughen the UHTCs is to introduce continuous fibers into their matrix. Continuous fiber-reinforced UHTC matrix composites (UHTCMCs) overcome the inherent brittleness and poor thermal shock resistance of bulk UHTCs [20–23]. Compared to the traditional aerospace composites of C or SiC matrices, the UHTCMCs seek to provide higher-

temperature capability and enhanced ablation resistant performance. As shown in Fig. 1, the publications about UHTCMCs appear in ~2005, on the development of 2.5D-C_f-reinforced HfC and 2.5D-C_f-reinforced ZrB_2–SiC composites [24,25]. Since then, UHTCMCs have stirred up a spree of researches, with a rapid increase in the number of relevant publications every year.

1. 2 Challenges

Thermal environments for hypersonic vehicles include ultra-high temperatures (> 2000 ℃), large thermal gradients and stresses, highly chemically active airflows (> 10 $MW \cdot m^{-2}$), and complex thermal–mechanical loads [26]. As mentioned above, monolithic UHTCs are susceptible to catastrophic failure during their services. Various approaches have been applied to improve the fracture toughness and thermal shock resistance of UHTCs.

(1) Particulate [27–29], chopped fiber, and whisker reinforced UHTCs

The effects of particles on the reinforcing of UHTCs are rather limited [30]. For this concern, carbon nanotubes, chopped fibers, and whiskers have been adopted as reinforcing elements to improve the fracture toughness of UHTCs. The previous work demonstrated that HfB_2 matrix incorporated with carbon nanotube exhibited excellent fracture toughness of 7.8 $MPa \cdot m^{1/2}$ and strength of 894 MPa [31]. Nevertheless, the reaction between carbon nanotube and oxide impurities in the UHTCs might be a problem as it can deteriorate the mechanical performance. The homogenization of these additives in the UHTCs was also challenging [32]. SiC whiskers (SiC_w) showed a better role in hardening and toughening of ZrB_2-based composites, compared to SiC particulates [33]. Investigations demonstrate that SiC_w exhibited greater degradation than SiC fibers, as the easy conversion of SiC_w into SiC particles during the sintering process [34]. During sintering, strong interactions between fibers and matrix are occurred inevitably, limiting the degree of fiber pullout during failure. The problem could be solved either by introducing a soft interphase layer on the fibers or by developing new technologies to manufacture UHTCs in which sintering is no longer needed.

(2) Continuous fiber-reinforced UHTC matrix composites (UHTCMCs)

The poor thermal shock resistance of bulk UHTCs could be improved by loading UHTCs into the fiber preforms. Carbon fibers are the most used fibers for UHTCMCs, and it has been suggested that the effects of carbon fiber types on the fracture toughness of UHTCMCs are rather limited [35]. Various processing methods, such as chemical vapor infiltration (CVI), precursor infiltration and pyrolysis (PIP), slurry infiltration (SI), and reactive melt infiltration (RMI), have been developed for the fabrication of UHTCMCs. Denser UHTCMCs could be obtained by combining these approaches with a further heat treatment with pressure.

(3) UHTC coatings

An alternative approach to avoid the catastrophic failure of large monolithic UHTC component is to deposit them on tough and heat resistant substrates [36–42], i.e., carbon fiber-reinforced composites and graphite. Since the 2000s, especially after X-43A completed its flight test, interests on UHTC ceramic coatings have become one of the research focuses. To survive in harsh aerothermal heating, the basic requirements of UHTC coatings are as follows: good expansion coefficient match with the substrate; good integrity/uniformity and strong interface bonding. In real working conditions, the preparation of UHTC

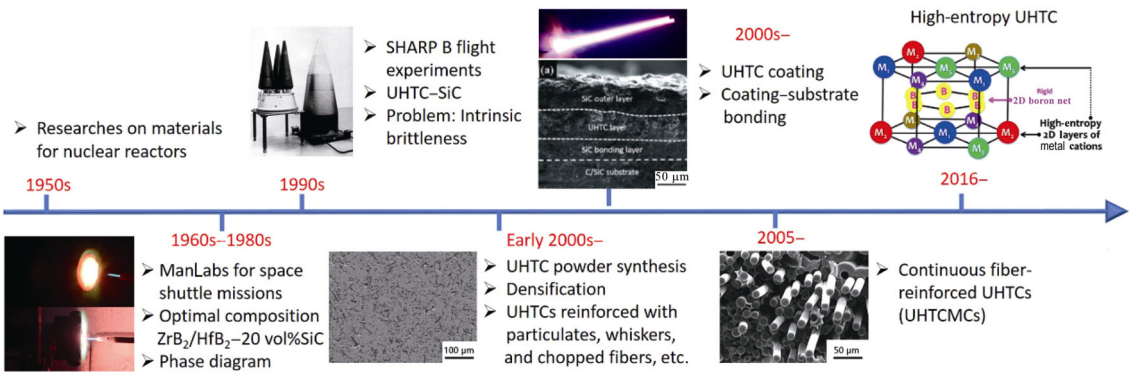

Fig. 1 Historical perspective on research related to ultra-high temperature ceramics and composites.

coating necessarily involves a mechanism which can coordinate the usage of the aforementioned requirements. Therefore, the reported UHTC coatings usually present different compositions and structures.

In this review, processing and properties of bulk UHTCs will be first detailed, followed by the processing of UHTCMCs. The focus here would be limited to processing routes of these composites with particular discussion on their mechanical behavior and ablation resistance. In the coating section, the UHTC coatings are divided according to their composition and structure differences, and their performances are discussed based on the design rules of the coating. By applying the entropy-stabilization concept to UHTCs, a number of multicomponent carbide/borides were recently fabricated, as an emerging direction for the development of ultra-high temperature ceramics and composites. The recent progresses on the processing and properties of high-entropy UHTCs are also included in this review. By combining the progress on ceramics, composites, and coatings, this review tries to provide guidelines for the researchers to design, select, and manufacture suitable forms of ultra-high temperature materials for demanding environments.

2 Bulk UHTCs: Composition, microstructure, and performance

2.1 Lattice structure of UHTCs

UHTCs all exhibit strong covalent bonding which gives them structural stability at high temperatures. Metal carbides are brittle due to the strong bonds between carbon atoms. The largest class of carbides, including Hf, Zr, Ti, and Ta carbides have high melting points due to covalent carbon networks although carbon vacancies often exist in these materials [60]. Nitrides such as ZrN and HfN have similarly strong covalent bonds [59] but their refractory nature makes them especially difficult to synthesize and process. The stoichiometric nitrogen content can be varied in these complexes and relates to their synthetic techniques [63–65]. Boride UHTCs, such as HfB_2 and ZrB_2, benefit from very strong bonding between boron atoms as well as strong metal to boron bonds; the hexagonal close-packed structure with alternating two-dimensional (2D) boron and metal sheets gives these materials high and anisotropic strength as single crystals (Fig. 2) [66]. The crystal structures, and basic physical and mechanical properties of the main UHTCs are shown in Table 1.

Table 1 Basic physical and mechanical properties of boride, carbide, and nitride-based UHTCs

Material	Crystal structure	Melting temperature (℃)	Density ($g \cdot cm^{-3}$)	CTE, α (10^{-6} K^{-1})	Thermal conductivity ($W \cdot m^{-1} \cdot K^{-1}$)	Electrical resistivity ($\mu\Omega \cdot cm$)	Elastic modulus (GPa)		Hardness (GPa)	Ref.
							Cal.	Exp.		
Boride										
TaB_2	HCP	3040	12.5	8.2–8.8	10.9–16.0	33	497	551	19.6	[18,43–50]
TiB_2	HCP	3225	4.5	7.6–8.6	64.4	16–28.4	583	575	24.0	[17,18,47,50–55]
ZrB_2	HCP	3245	6.1	5.5–8.3	57.9	9.2	523	489	23.0	[17,18,46,50–52,56]
HfB_2	HCP	3380	11.2	6.3–7.6	51.6	8.8–11	535	451	28.0	[17,18,50–52,57,58]
Carbide										
TiC	FCC	3100	4.9	7.5–7.7	17–21	52.5	455	437	30.0	[44,51,52,59–62]
ZrC	FCC	3530	6.6	6.82	20.61	68.0	436	387	25.0	[51,52,59,61,63–65]
TaC	FCC	3800	14.5	6.6–8.4	22.2	30–42.1	550	537	17.0	[44,51,52,59,66–68]
HfC	FCC	3900	12.8	6.3	22.2	45.0	537	461	24.2	[17,44,51,52,59,61,69,70]
Nitride										
TaN	FCC	2900	13.4	3.2	8.3	128–135	490	490	10.8	[43,44,51,52,71–73]
TiN	FCC	2950	5.4	9.35	29.1	21.7	463	400	18.6	[51,52,72,74–79]
ZrN	FCC	2950	7.3	7.24	20.9	13.6	390	384	15	[51,52,64,78,80,81]
HfN	FCC	3385	13.9	6.5	21.6	33	411	398	16.1	[12,51,52,72,76,78,80,82]

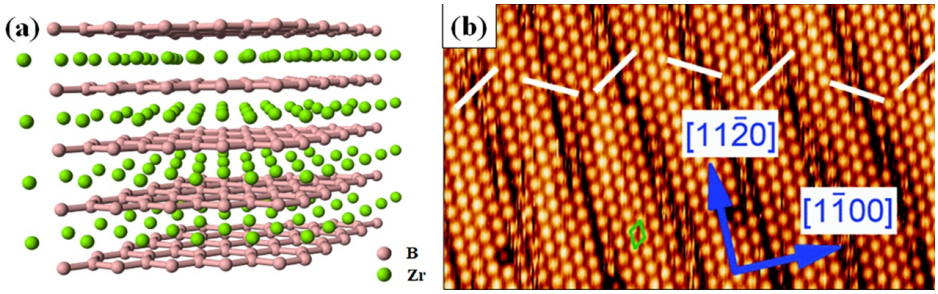

Fig. 2 Hexagonal close-packed structure (a) and STM image (b) of the (2×2)-reconstructed ZrB_2 (0001) surface. Reproduced with permission from Ref. [66], © The American Physical Society 2012.

2. 2 Processing technology of bulk UHTCs

Bulk ceramics are the initial application form for UHTCs, which can be densified by various methods, including hot pressing (HP) [67–72], spark plasma sintering (SPS) [73,76,79], reactive hot-pressing (RHP) [74,75,77,78], and pressureless sintering (PLS) [80–85], etc. The following part focuses on the various densification processes, as well as the sintering aids on the densification behavior of UHTCs.

(1) Hot pressing (HP)

Due to the strong covalent bonds, low volume, and grain boundary diffusion rates, UHTCs generally need to be sintered at a very high temperature assisted with pressure. HP has been the dominant method for the densification of UHTCs. For single-phase ZrB_2, high temperature (≥ 2100 ℃) and low pressure (20–30 MPa) or lower temperature (~1800 ℃) and extremely high pressure (> 800 MPa) are usually needed to achieve densification [4]. Besides the inherent properties of its own crystal structure, the surface oxide impurities of UHTC powder also limit its densification to some extent. Studies have shown that oxide impurity layer can be formed on the surface of ZrB_2 powder when exposed to air, including B_2O_3 and ZrO_2 [86]. During sintering, the B_2O_3 with low melting point will turn to liquid or gas phase, which promotes the surface diffusion of ZrB_2, resulting in coarsening of the grains. At the same time, the presence of B_2O_3 and ZrO_2 will reduce the activity of B atoms to some extent and hinder the densification of ZrB_2 [87]. To promote the densification of UHTCs, it is usually necessary to introduce appropriate sintering aids, which mainly include deoxidizing aids, liquid phase aids, solid solution aids, etc. The main deoxidizing aids are Si_3N_4, AlN, WC, VC, B_4C, etc. [88,89]. The chemical reaction between the sintering aids and the oxide impurities can realize deoxidization. The liquid phase aids are mainly composed of metals such as Fe and Ni, which turn into liquid phase and promote the rearrangement and mass transfer of ZrB_2 particles during sintering. The solid solution aids are mainly composed of Mo and other elements. During sintering, the solid solution of Mo and ZrB_2 particles occurs, which activates the lattice to enhance the sintering driving force and promote densification [90]. The introduction of sintering aids can significantly reduce the HP temperature of ZrB_2 ceramics.

SiC is the most commonly used second phase additive for UHTCs particularly for borides. The addition of SiC can improve the sinterability and inhibit grain growth of UHTCs. Plastic deformation of SiC at high temperatures can promote the slip and rearrangement of ZrB_2 particles and fill the voids left by ZrB_2 particles' slip and rearrangement, thus promoting the densification of ZrB_2. The addition of SiC can also improve the oxidation and ablation resistance of UHTCs. Table 2 lists the densification behavior of ZrB_2-based UHTCs prepared by HP under different conditions [91–100].

Table 2 Densification behavior of ZrB_2-based UHTCs by HP

Material	HP conditions (℃, MPa, min)	Relative density (%)	Ref.
ZrB_2	2000, ~17, 260	99	[100]
ZrB_2	1900, 30, 30	86.5	[99]
ZrB_2–25Nb	1800, 30, 60	99.1	[91]
ZrB_2–5Si_3N_4	1700, 30, 15	98	[98]
ZrB_2–5AlN	1850, 30, 60	97.2	[95]
ZrB_2–20$MoSi_2$	1850, 30, 60	98.5	[94]
ZrB_2–20$ZrSi_2$	1550, 30, 15	99.1	[96]
ZrB_2–10Mo	1950, 20, 60	98.9	[92]
ZrB_2–20SiC	1900, 30, 60	98	[97]
ZrB_2–20SiC_{nano}	1900, 30, 60	~100	[93]

With the development of sintering technology in recent years, SPS technology has begun to be widely used for the densification of UHTCs. SPS is a rapid sintering technology in which sintering current and pressure are applied to ceramic powder through electrodes to generate high temperature and pressure in a short time. SPS is also a pressure assisted high-temperature sintering method, but compared with traditional HP, SPS has a faster heating rate, which can effectively avoid grain growth and obtain dense and fine-grained ceramic materials in a very short time.

(2) Pressureless sintering (PLS)

PLS is a traditional sintering method for ceramic materials. It can produce near-net ceramics with complex shapes. Therefore, it is a low-cost producing technology for bulk UHTCs. However, full densification is difficult to be achieved for UHTCs by PLS. Sintering aids are usually introduced during the PLS, which mainly include two types. The first is low melting point phases, such as metals Ni, Fe, Mo, etc. [101–103] and transition metal disilicides $MoSi_2$, $ZrSi_2$, etc. [104,105]. They can form a liquid phase during sintering to promote the densification of ZrB_2-based UHTCs. The second category can react with oxide impurities on the surface of UHTC particles. For the first time, Zhang *et al*. [86] realized that oxide impurities on the surface of ZrB_2 powder will cause rapid growth of grains at the initial stage of sintering and hinder the densification. This kind of sintering aid can consume the oxide impurities on the powder surface and improve the sintering activity of powders [106–108]. Nitrides (such as AlN and Si_3N_4) can consume B_2O_3 impurities on the surface of ZrB_2 powder; carbon and boron compounds (such as B, B_4C, C, WC, and phenolic resin) can consume ZrO_2 impurities on the surface of ZrB_2 powder [85,109–111]. B_4C can react with ZrO_2 above 1200 ℃ [86,112], which not only promotes the densification of ZrB_2, but also keeps the high-temperature strength of ZrB_2, and the microstructure is shown in Fig. 3. So, it is widely used as a sintering aid for PLS of ZrB_2. The introduction of carbon (granular or precursor) can also significantly improve the sintering performance of ZrB_2. Adding 2 wt%B_4C+1 wt%C mixed sintering aid to micron ZrB_2 powder, it can realize the densification at 1900 ℃ by PLS [106]. Jafari *et al*. [113] found that using part of HfB_2 to replace ZrB_2 in the ZrB_2–SiC system is conducive to promote the densification during PLS.

(3) Reactive sintering (RS)

RS has been identified as an effective approach to produce UHTCs with high density and low impurity at relatively low temperatures. Generally, two processes are involved in RS, *in-situ* reactions of raw materials and densification, which are completed simultaneously during heating and subsequent holding.

The reactive sintering of UHTCs is first realized and reported by Zhang *et al.* [114] in 2004. Using Zr/Hf and B/C powders as raw materials, monolithic ZrB_2, HfB_2, HfC, and ZrC ceramics can be produced by RS. ZrB_2-based composites with SiC and/or ZrC can be produced by using Zr, B_4C, and Si as raw materials, and the related reaction is shown below [114–116]:

$$x\mathrm{Zr} + y\mathrm{B_4C} + (3y–x)\mathrm{Si} \rightarrow 2y\mathrm{ZrB_2} + (x–2y)\mathrm{ZrC} + (3y–x)\mathrm{SiC} \quad (1)$$

It can be seen that the composition of the product can be tailored by designing the ratio of the original powders. Figure 4 shows the typical microstructure of ZrB_2–ZrC–SiC produced by RS at 1800 ℃. The improvement of densification by RS process can be attributed to the formation of nano-sized particles during the reactive process. As the densification is generally driven by minimization of the surface free

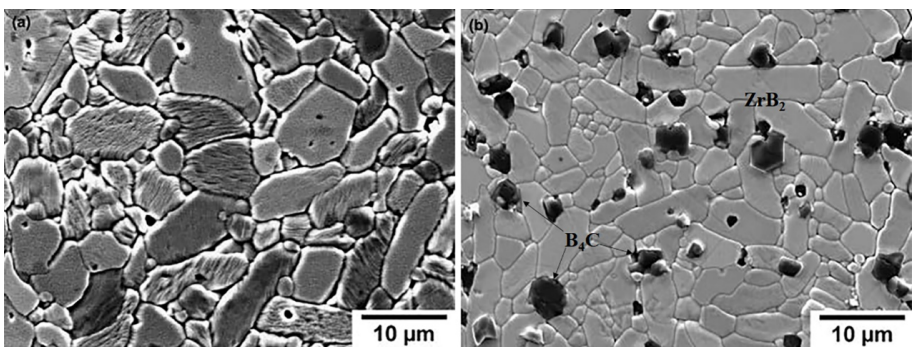

Fig. 3 Microstructures of pressureless sintered ZrB_2 with B_4C addition at 1850 ℃/1 h in vacuum: 2 wt% B_4C (a) and 4 wt%B_4C additions (b). Reproduced with permission from Ref. [86], © The American Ceramic Society 2006.

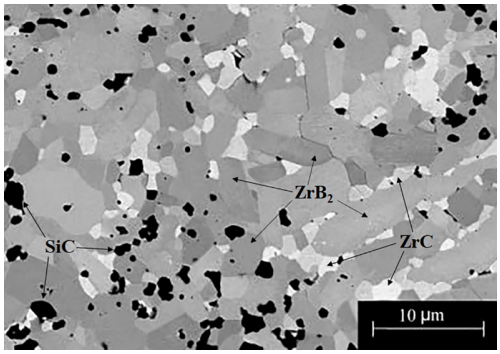

Fig. 4 Typical microstructure of ZrB_2–ZrC–SiC produced by reactive sintering. Reproduced with permission from Ref. [115], © The American Ceramic Society 2006.

energy, the fine crystalline size can enhance the driving force for densification accordingly. Carbothermal reduction method is also applied for preparing ZrB_2 ceramics by RS. ZrO_2, B_4C, and C are used as raw materials to produce ZrB_2 by RS [117]. However, due to the formation of gaseous byproduct during the reaction process, the ceramics prepared by carbothermal reduction reaction have low densification and poor mechanical properties. The UHTC materials prepared by reactive sintering are generally characterized with fine grain size. Kannan and Rangaraj [118] used Zr and B_4C powders with different proportions, to obtain ZrB_2–ZrC_x UHTCs through reactive sintering. The sintering temperature was reduced to 1200 ℃ by using this process. The material exhibits excellent mechanical properties.

2. 3 Mechanical properties and thermal shock resistance of bulk UHTCs

(1) Mechanical properties of bulk UHTCs

Mechanical properties are the key indicators for the use of UHTCs. Table 3 lists the mechanical properties of typical UHTCs at room temperature [119]. The elasticity and hardness of ZrB_2 and HfB_2 based ceramics are closely related to the samples' density. The room-temperature flexural strength is strongly related to the grain size, which in turn depends on the initial powder particle size, reinforcement phase content, and sintering parameters. Refinement of the matrix (ZrB_2 or HfB_2) and reinforcement phase (such as SiC) particles are beneficial to the densification and mechanical properties of the material. The reduction of the original particle size is conducive to the refinement

Table 3 Mechanical properties of typical UHTCs at room temperature [119]

Composition (vol%)	Sintering conditions (℃, MPa, min)	Original particle size (μm)		Elastic modulus (GPa)	Hardness (GPa)	Flexural strength (MPa)	Fracture toughness ($MPa·m^{1/2}$)	Grain size after sintering (μm)	
		$Zr(Hf)B_2$	SiC					$Zr(Hf)B_2$	SiC
ZrB_2	1900, 30, 30	6.0	—	346	8.7±0.4	351±31	3.5±0.3	6.0	—
ZrB_2	1900, 32, 45	2.0	—	489	23±0.9	565±53	3.5±0.3	6.0	—
ZrB_2–10%SiC	1900, 32, 45	2.0	0.7	450	24±0.9	713±48	4.1±0.3	3.0	—
ZrB_2+15%SiC+4.5%ZrN	1900, 50, 20	2.0	0.45	467±4	15.6±0.3	635±60	5.0±0.1	3.0	0.8
ZrB_2–20%SiC	1900, 32, 45	2.0	0.7	466	24±2.8	1003±94	4.4±0.2	3.0	1.0
ZrB_2–20%SiC–6%ZrC (HP)	1850, 30, 60	2.0	1.0	—	19.4±0.4	681±67	5.7±0.2	3.0	1.5
ZrB_2–20%SiC–6%ZrC (RHP)	1850, 30, 60	—	—	—	19.9±0.3	652±21	7.3±0.3	3.0	1.5
ZrB_2–30%SiC	1900, 32, 45	2.0	0.7	484	24±0.7	1089±152	5.3±0.5	3.0	1.0
ZrB_2–30%SiC	1850, 32, 45	2.0	0.7	516±3	20±2	1063±91	5.5±0.3	2.2	1.2
ZrB_2–30%SiC	1950, 32, 45	2.0	0.7	507±3	22±2	1060±59	5.2±0.4	2.5	1.7
ZrB_2–30%SiC	2050, 32, 45	2.0	0.7	505±2	23±1	854±88	4.3±0.2	3.5	2.0
ZrB_2–30%SiC	2050, 32, 180	2.0	0.7	505±1	22±1	804±73	4.5±0.2	4.7	2.7
ZrB_2–30%SiC	1850, 32, 45	6.0	0.7	503±6	22±2	888±151	3.9±0.1	2.1	1.5
ZrB_2–30%SiC	1950, 32, 45	6.0	0.7	501±1	22±2	770±133	4.0±0.2	3.3	2.5
ZrB_2–30%SiC	2050, 32, 45	6.0	0.7	503±1	23±2	720±38	4.3±0.2	3.7	3.1
ZrB_2–30%SiC	1900, 32, 45	6.0	0.45	520±7	20.7±1.0	909±136	4.5±0.1	1.2	1.0
ZrB_2–30%SiC	1900, 32, 45	6.0	10.0	479±5	17.5±0.4	389±45	4.6±0.1	3.0	6.3
ZrB_2–20%SiC–15%G	1900, 30, 60	3.0	2.0	—	—	481±28	6.11±0.24	3.0	2.0
HfB_2–20%SiC	2200, 32, 45	4.1	1.6	549±8	17±0.7	453±46	4.1±0.2	7.0	5.0
HfB_2–30%SiC–2%$TaSi_2$	1900, 42, 35	1.7	1.0	489±4	—	665±75	3.6±0.5	2.0	2.0

of UHTC grains and the strength of the materials follows the Hall–Petch relationship with the grain size [120]. Moreover, refinement of the reinforcement phase (SiC particles) has a more significant impact on the mechanical properties. The study by Zhang *et al.* [121] noticed that reducing the size of the starting SiC particles decreased the ZrB_2 grain size and changed the morphology of the final SiC grains from equiaxed to whisker-like. The highest flexure strength is obtained for the ZrB_2–SiC prepared from middle starting powder with an equiaxed SiC grain morphology, compared with ceramics prepared from finer or coarser SiC powders. In certain content, too fine SiC particle will be over a threshold and cause elongated morphology of SiC second phase and worsen the mechanical properties. It is indicated that the addition of SiC has a significant inhibitory effect on the grain growth of the matrix ZrB_2 and HfB_2. When the volume content of SiC reaches 20%, the inhibitory effect on grain growth is obvious. Further addition of SiC has little effect on the grain growth and strength.

On the contrary, the refinement of grain size has a very limited positive effect on the improvement of toughness, while grain morphologies of UHTCs have a significant effect on the fracture toughness. Compared with the equiaxed ZrB_2 obtained by hot-pressing, the fracture toughness of the long rod-shaped ZrB_2 by RHP is significantly improved up to 7.3 $MPa \cdot m^{1/2}$ [122]. To improve the fracture toughness of UHTCs, there are generally two main approaches. One is to introduce toughening phases (such as SiC whiskers [123], graphite [124], ZrO_2 [125], and ductile metals [126]), and the other is microstructure design (such as layered structure [127], and fiber monolithic structure [128]). The effect of the former is limited, and its fracture toughness is generally difficult to get 8 $MPa \cdot m^{1/2}$, while the latter can exceed 10 $MPa \cdot m^{1/2}$.

The high-temperature mechanical properties and fracture modes of UHTCs are very important research focus. High-temperature mechanical properties of UHTCs are mainly determined by the material composition, purity, and grain size. The high-temperature fracture mode is mainly intergranular fracture [129], which is different from that at room temperature. Therefore, the high-temperature flexural strength of the material is strongly dependent on the characteristics of grain boundaries. The improvement of material density and room-temperature mechanical properties could be realized by introducing low melting point substances (such as Fe, Ni, $ZrSi_2$, Al_2O_3, and Y_2O_3) into UHTCs matrix; however, it has a significant negative impact on the high-temperature mechanical properties, where the performance degradation is generally severe above 1000 ℃. The room-temperature flexural strength of UHTCs based on highly pure raw material powder can be maintained to 1500 ℃ with almost no reduction [130]. Using tungsten carbide to remove the oxide impurities in borides, ZrB_2–20%SiC–5%WC, HfB_2–20%SiC–5%WC with flexure strength up to 670 MPa could be achieved when they were tested at 1600 ℃ [88,131,132]. The materials with WC addition remained transgranular at 1600 ℃, while the others become fully intergranular fracture mode (Fig. 5). Apart from much less oxide contamination in the unique ceramic body, the high strength at elevated temperatures was also considered to be a result from the following two characteristics in ZSW: 1) the ZrB_2 grains with core–shell structure and 2) the tungsten segregation at the ZrB_2/ZrB_2 grain boundary [133,134]. Both of them might act as the barriers for the dislocation movement during fracture, therefore avoiding the strength degradation of ZSW at higher temperatures [133]. First-principles calculations by Dai *et al.* [135,136] also support such experimental observations, which suggest that the short equilibrium W–B bonds induce local contractions around the core–shell interface and the grain boundaries, therefore strengthening the grain boundaries.

In addition, SPS is beneficial to obtain UHTCs with excellent high-temperature flexural strength. This is because the low melting point impurities on the surface of the particles can be partially removed at the initial stage of SPS, thereby improving the grain boundary characteristics [137]. The refinement of grain size is beneficial to the room-temperature strength, but it is harmful to the high-temperature strength. The flexural strength of the ZrB_2 (2 μm)–15 vol%SiC (0.5 μm) material at 1800 ℃ is 112 MPa, and the flexural strength retention rate is only 12.9%. While the ZrB_2 (5 μm)–15 vol%SiC (2 μm) material at this temperature is 217 MPa, and the flexural strength retention rate is 43.4% [129].

Li *et al.* [138] assumed that breaking down the entire structure of a material can be considered as severing all the bonds between its atoms either by applying work or by heat transfer. Because bond-breaking is indifferent to either means, there is a kind of equivalence between heat energy and strain energy.

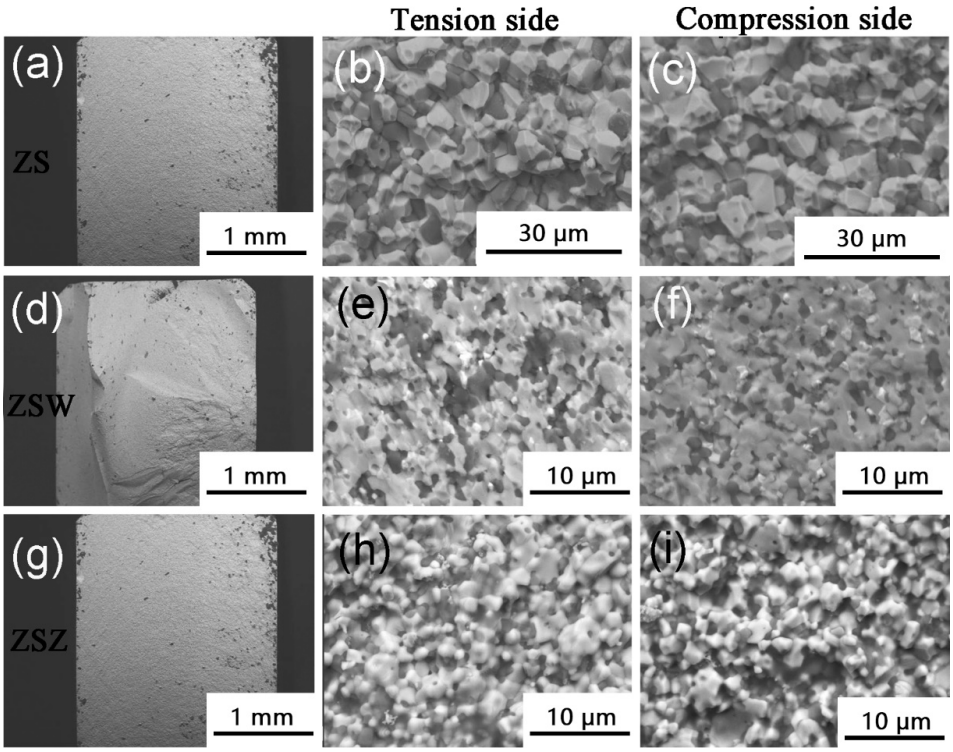

Fig. 5 Flexural surfaces of ZrB_2–SiC (ZS) (a–c), ZrB_2–SiC–WC (ZSW) (d–f), and ZrB_2–SiC–ZrC (ZSZ) (g–i) at 1600 ℃. Reproduced with permission from Ref. [131], © The American Ceramic Society 2012.

Accordingly, there should be the existence of a constant maximum storage of energy for a particular material that includes both the strain energy and the corresponding equivalent heat energy. Based on this assumption, a temperature dependent fracture strength model is developed for UHTCs. Model predictions for HfB_2, TiC, and ZrB_2 single-phase UHTCs are largely consistent with experimental results. Based on this temperature dependent fracture surface energy model and the traditional Griffith fracture theories, a temperature dependent fracture strength model is further developed for ZrB_2–SiC composites [139,140]. The combined effects of temperature, grain size, micro-flaw size, and residual stress on the strength of ZrB_2–SiC composites are included in this model. According to the model, the temperature dependent fracture strength of materials can be easily predicted using some basic material parameters. The model is verified with excellent agreement at different temperatures by comparison with experimental data of different ZrB_2–SiC composites. The developed model offers a mechanism of monitoring the strength of UHTCs at different temperatures by testing the change of flaw size, which provides a quantitative tool for design, evaluation, and monitoring of the fracture properties of UHTCs at high temperatures.

(2) Thermal shock resistance of bulk UHTCs

Bulk UHTCs are a typical brittle material, and it is prone to thermal shock failure under extreme heating environment, leading to catastrophic damage, so it is particularly important to improve its thermal shock resistance. For bulk UHTCs, we concern about crack initiation and crack propagation mostly, which can be expressed by thermal shock fracture parameters (R'''') and thermal shock damage parameters (R) [141–143]:

$$R'''' = \frac{E\gamma_s}{\sigma_f^2(1-\upsilon)} = \frac{K_{IC}^2}{2\sigma_f^2(1-\upsilon)} \quad (2)$$

$$R = \frac{\sigma_f(1-\upsilon)}{E\alpha} \quad (3)$$

where σ_f is the fracture strength of the material, υ is the Poisson's ratio, E is the elastic modulus of the material, α is the thermal expansion coefficient of the material, γ_s is the fracture surface energy, and K_{IC} is the fracture toughness of the material. It can be seen from Eq. (2) that under the condition that the elastic modulus, thermal expansion coefficient, and Poisson's ratio remain unchanged, increasing the flexural strength of UHTCs is beneficial to improve its thermal shock resistance. Since the thermal expansion coefficients of ZrB_2, HfB_2, and SiC are quite different,

huge thermal tension stress will be generated on ZrB_2/HfB_2 grains after high-temperature sintering, which will adversely affect the thermal shock resistance. Therefore, the material design needs to consider reducing thermal stress, by adding a high melting point soft phase such as graphite, etc. The thermal shock resistance of bulk UHTCs can be greatly improved by microstructure design, such as layered structure and fiber monolithic structure. ZrB_2-based fibrous monolithics have a critical thermal shock temperature difference of 1400 ℃ compared with ZrB_2 and ZrB_2–30 vol%SiC material, which increased by 250% [144].

2. 4 Microstructure design and performance regulation of bulk UHTCs

Symmetrically distributed strong covalent bonds lead to intrinsic brittleness and low damage tolerance of UHTCs, which has always been the core problem and bottleneck of bulk UHTCs. Research on the strengthening and toughening technology of UHTCs has become the most concerned topic when discussing the performance regulation of UHTCs. In the traditional sense, the strengthening and toughening technology of UHTCs has evolved to find the best balance between strength and toughness, considering the oxidation ablation resistance. Figure 6(a) shows the Ashby diagram of the yield strength and fracture toughness of typical engineering materials [145]. By tailoring the composition of the material, the fracture toughness can be gradually improved along the direction indicated by the white arrow. Figure 6(b) shows the effects of intrinsic ductility (plasticity) and non-intrinsic ductility (shielding against cracks) of the material on the strength and toughness behavior of the material during crack propagation [145]. Intrinsic toughening mainly comes from the plasticity of the material itself, where the damage tolerance of the material is improved by affecting the crack initiation and propagation. Non-intrinsic toughening relies on the suppression of crack propagation after crack initiation. In this case, the toughness of the material is improved by reducing the local stress and strain field at the crack tip. For the toughening of UHTCs, the toughening phases such as particles, whiskers, carbon nanotubes, and graphene are introduced to induce crack deflection and bifurcation by pulling out and bridging the ductile phases, thereby inhibiting the forward transfer of the crack tip, and thus achieving the toughening effect, which is extrinsic toughening as shown in Fig. 6(b). The microstructure design and performance regulation of UHTCs will be described in detail in the following section.

(1) Particle toughening

The method of improving mechanical properties, impact resistance, and corrosion resistance of composites by addition of second-phase dispersion particles is called particle toughening.

The strength and fracture toughness of UHTCs can be improved by particle toughening, and the common additive is silicon-containing compounds. Among these silicon-containing compounds, the addition of SiC can maximize the comprehensive properties of UHTCs. The addition of SiC can effectively hinder grain growth, and improve the sintering activity and fracture toughness of the UHTCs. By controlling the size of SiC particles, the maximum strength and toughness of the material can be achieved. Generally speaking, Vickers hardness and tensile strength gradually

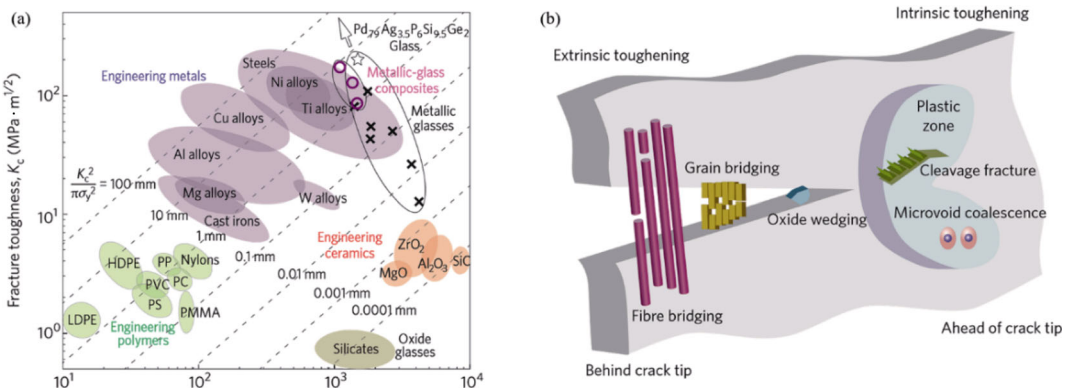

Fig. 6 Conflicts of strength versus toughness: Ashby plot showing strength–toughness relationships for engineering materials (a); schematic of intrinsic versus extrinsic toughening (b). Reproduced with permission from Ref. [145], © Nature Publishing Group, a division of Macmillan Publishers Limited 2011.

decrease with the increase of grain size [146]. The content of reinforcement is also an important factor affecting the toughening effect. Asl *et al.* [147] studied the effect of SiC_p content on the relative densities and mechanical properties of ZrB_2–SiC_p prepared by hot-pressing (2000 ℃/30 min/10 MPa). When the content of SiC_p increases from 10 vol% to 30 vol%, the grain growth of ZrB_2 is inhibited, and the relative density increases from 98.3% to 99.8%. At the same time, the mechanical properties show an increasing trend and the fracture toughness increases from 3.5±0.1 to 3.8±0.2 MPa·$m^{1/2}$, which is mainly attributed to the coupling toughening mechanisms such as transgranular fracture and crack deflection. Figure 7 shows a typical crack propagation path in ZrB_2–SiC after indentation, showing crack deflection near SiC particles and predominantly transgranular fracture for ZrB_2 grains [148].

(2) Whisker toughening

As a kind of fibrous single crystal material, whiskers have small diameter, large aspect ratio, high tensile strength, and elastic modulus due to few surface defects, so they have wide application prospects in ceramic toughening [149]. SiC whisker has a cubic lattice structure, which has the highest hardness, maximum modulus, maximum tensile strength, and the highest heat resistance temperature. As a result, SiC whiskers are widely used as toughening phase. Due to its large aspect ratio, it can effectively inhibit the grain growth when it is evenly distributed around the ceramic grains, thus refining the grains and improving the mechanical properties of the materials [150]. Zhang *et al.* [151] studied the effect of the addition of SiC_w on the mechanical properties of ZrB_2. The results show that the fracture toughness of ZrB_2–20 vol%SiC_w ceramic is as high as 5.97±0.3 MPa·$m^{1/2}$. It is much higher than traditional ZrB_2 ceramic (2.3–3.5 MPa·$m^{1/2}$) and ZrB_2–SiC ceramic (4.0–4.5 MPa·$m^{1/2}$). From study of the micro-morphology of crack propagation after nano-indentation, it can be seen that the whisker pull-out and whisker bridging phenomenon during the crack propagation process are promoted due to the whisker self-height aspect ratio and moderate interface bonding with ZrB_2 matrix, and the crack deflection is accompanied around the whiskers. The synergistic effect of these toughening mechanisms can absorb a large amount of crack propagation energy, and improve the fracture toughness of the materials.

(3) Carbon nanotube toughening

Carbon nanotubes (CNTs) have attracted the attention of many scientists since their unique structure and excellent mechanical, electrical, and chemical properties were discovered by Dr. Iijima from the NEC corporation in 1991 [152]. The fracture toughness of UHTCs can be improved by adding a small amount of carbon nanotubes. The study by Tian *et al.* [153] indicated that the addition of 2 wt% CNTs into ZrB_2–20 vol%SiC increases the fracture toughness by about 15%. Lin *et al.* [154] systematically studied the effect of sintering temperature (1600–1800 ℃) on ZrB_2–10 vol%CNTs prepared by SPS (Fig. 8). The results show that the maximum fracture toughness of ZrB_2–CNT ceramic material (7.2 MPa·$m^{1/2}$) is achieved at the sintering temperature of 1650 ℃, which is much higher than that of single-phase ZrB_2 ceramic material (3.3 MPa·$m^{1/2}$). The synergistic effect of carbon nanotube pull-out and crack deflection mechanisms greatly increases the damage tolerance of ZrB_2 ceramics.

(4) Graphene toughening

Graphene is a 2D carbon nanomaterial whose carbon atoms form hexagonal lattices with sp^2 hybrid

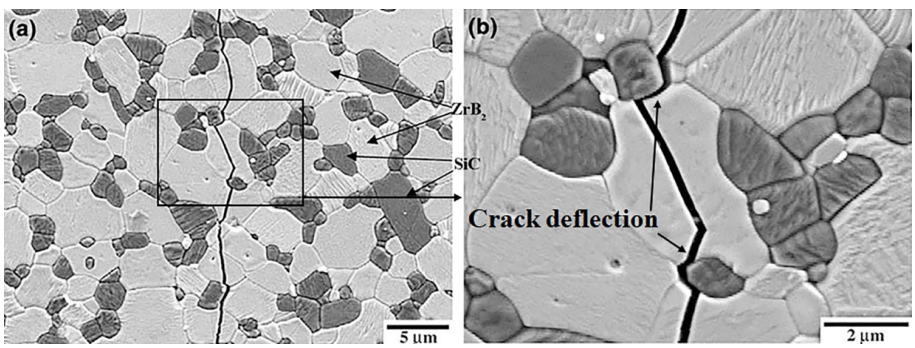

Fig. 7 Typical crack propagation path of ZrB_2–SiC after indentation at low (a) and high (b) magnification showing crack deflection near SiC particles and predominantly transgranular fracture for ZrB_2 grains. Reproduced with permission from Ref. [148], © Springer Science Business Media, LLC 2007.

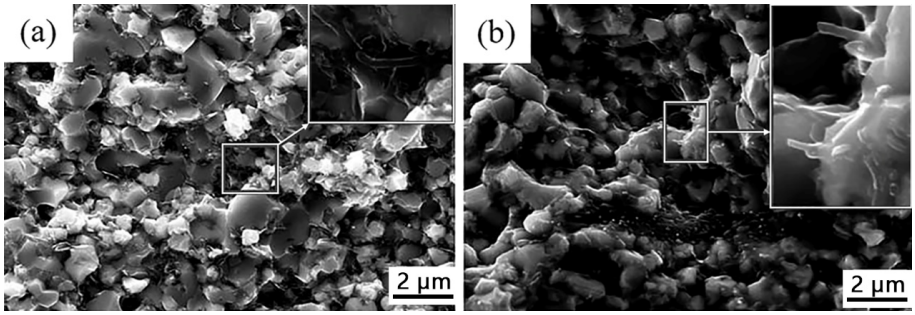

Fig. 8 Fracture morphologies of ZrB_2–CNT ceramics sintered at 1600 ℃ (a) and 1650 ℃ (b). Reproduced with permission from Ref. [154], © Maney Publishing 2016.

orbitals [155]. Ocak *et al.* [156] introduced graphene nano-sheets (GNP) with different volume contents from 0 vol% to 9 vol% into TiC–ZrC ceramics by SPS. The results show that the relative density of 3 vol% GNP–TiC–ZrC is higher than 99%, and the maximum fracture toughness is 5.17 $MPa \cdot m^{1/2}$. Cheng *et al.* [157] reported ZrC–SiC–graphene composites preparing by mud impregnation into macroporous graphene network structure, followed by SPS. The microstructure is shown in Fig. 9. The graphene lamella is parallel to the compressed surface, and the fracture toughness of the material is improved from 3.82 to 4.26 $MPa \cdot m^{1/2}$, although the flexural strength of ZrC–SiC ceramics with graphene decreases from 416 to 220 MPa. This is mainly due to crack deflection and bridging induced by macroporous graphene (Fig. 9).

Overall, the above-mentioned toughening designs can improve the toughness and thermal shock resistance of UHTCs to some extent. However, the reliability of bulk UHTCs still cannot match the requirements of engineering applications. Generally, the practical applications of UHTCs are in forms of fiber-reinforced UHTC composites or coatings, which will be discussed in Sections 3 and 4 in detail.

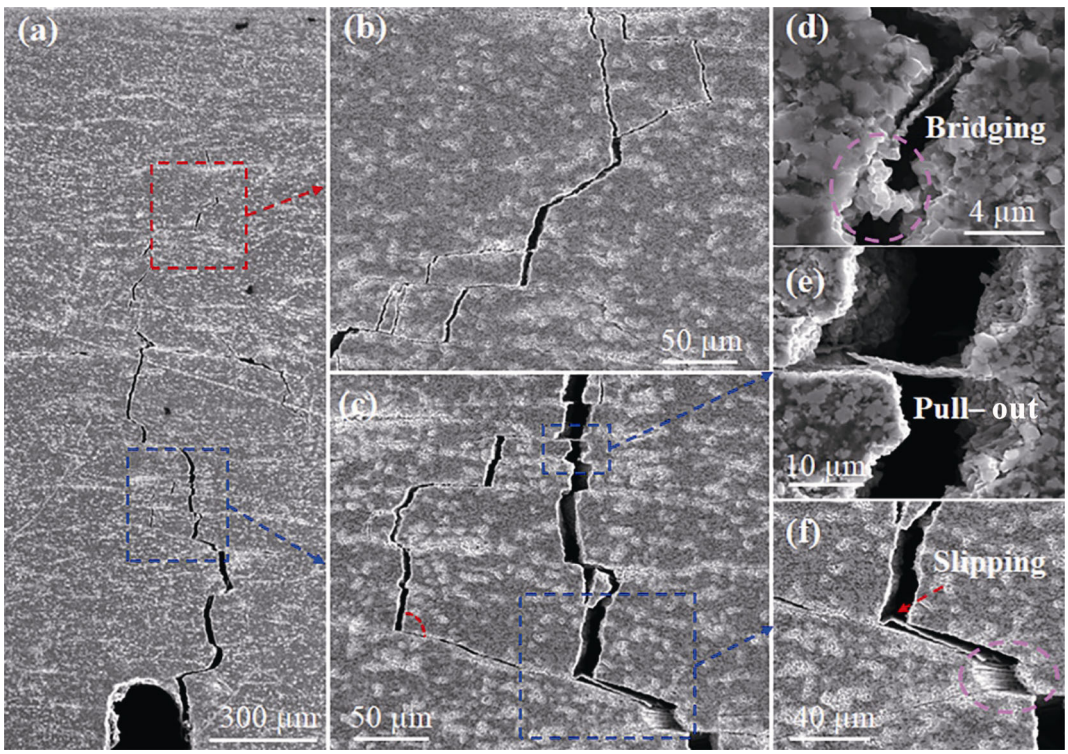

Fig. 9 Crack propagation of ZrC–SiC–graphene composites (a); crack deflection and crack branching in the partially enlarged view of the red (b) and blue (c) square dashed frames in (a); bridging (d), pull-out (e), and slipping (f) of graphene sheets. Reproduced with permission from Ref. [157], © Elsevier Ltd. 2018.

2. 5 Thermal response, oxidation/ablation behavior, and mechanisms of bulk UHTCs

Thermal response, oxidation/ablation behavior, and mechanisms are also complicated but play an important role in the characterization and evaluation of UHTCs. There are many factors related to the thermal response of UHTCs such as thermal conductivity, volumetric heat capacity, catalytic efficiency, emissivity, and oxidation characteristic. The surface temperature rising rate of UHTCs during initial heating stage and temperature gradient strongly depends on the thermal conductivity and volumetric heat capacity. The surface temperature evolution and the maximum surface temperature are closely associated with environmental parameters, oxidation reaction models, and physico-chemical properties of the oxidation products. Oxidation of UHTCs is a comprehensive process in which oxygen diffuses inward and gaseous or liquid oxidation products diffuses outward. The oxidation/ablation performance and mechanisms of UHTCs system are not the same for different components and environmental conditions. Therefore, it is required to fully understand the oxidation and ablation process of UHTCs, before we can design and control the composition, microstructure, and key properties of UHTCs according to the requirements of different service environments. In the following section, oxidation/ablation process and mechanisms of typical UHTC materials are introduced to lay the foundation for the design of ultra-high temperature thermal protection materials.

For carbide UHTCs, the oxidation process is mainly characterized by the outward diffusion of inner metal atom Me (metal) and the inward diffusion of outer oxygen atom [158]. A large number of oxygen atoms diffuse into the MeC lattice and form an oxide layer in the interior, which is composed of a loose outer layer and a dense inner layer. Figure 10 shows the mechanistic model for the oxidation of ZrC to ZrO_2.

Voitovich and Pugach [159] focused on the static oxidation behavior of ZrC and HfC in the temperature range of 500–1200 ℃, and the involved oxidation reactions are as follows:

$$\mathrm{MeC} + \mathrm{O_2} \rightarrow \mathrm{Me}_x\mathrm{O}_y + \mathrm{CO_2} \quad (4)$$

$$\mathrm{MeC} + \mathrm{O_2} \rightarrow \mathrm{Me}_x\mathrm{O}_y + \mathrm{CO} \quad (5)$$

$$\mathrm{MeC} + \mathrm{O_2} \rightarrow \mathrm{Me}_x\mathrm{O}_y + \mathrm{C} \quad (6)$$

$$2\mathrm{MeC} + \mathrm{N_2} \rightarrow 2\mathrm{MeN} + 2\mathrm{C} \quad (7)$$

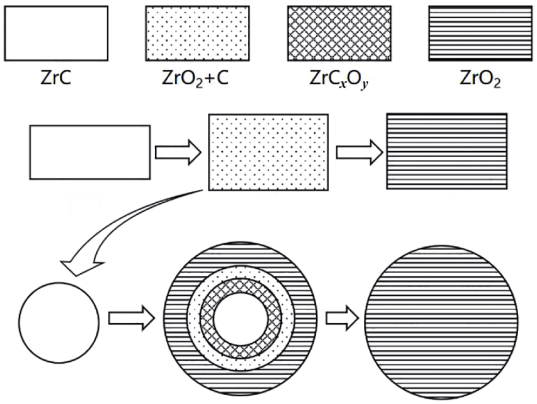

Fig. 10 Mechanistic model for the oxidation of ZrC to ZrO_2. Reproduced with permission from Ref. [158], © Elsevier B.V. 1994.

Voitovich and Pugach [159] found that the occurrence of reactions closely related to oxygen partial pressure and temperature. At the initial stage of oxidation, the Reaction (4) occurs on the surface of the materials due to the sufficient oxygen partial pressure. With the diffusion of oxygen into the material, the Reactions (5) and (6) start. At higher temperatures, N_2 in the air can also combine with Me, which is Reaction (7). Under oxidation at 900 ℃, an oxide layer with a higher sintering degree can be formed on the surface of ZrC [160], which is closely bound to the substrate, and the vacancy concentration of the oxidized phase ZrC_xO_y formed inside is low. At low temperature oxidation stage, the oxidation resistance of ZrC is slightly better than that of HfC. It is revealed that the oxide layer thickness of HfC at 1400 ℃ increases linearly with time. However, the oxide layer thickness of HfC shows a parabola relationship with time at 1400–2100 ℃, and the oxide layer structure evolves into a complex multi-layer structure: the outer layer of porous HfO_2, the middle layer of dense HfC_xO_y, and the inner layer of residual carbon. The dense structure of the intermediate HfC_xO_y layer can well prevent the inward oxygen diffusion. Below 1500 ℃, the oxidation layer of HfC has a poor sintering degree and easily peels off from the substrate. At temperatures above 1800 ℃, HfO_2 can be sintered to form a dense oxide film, showing good oxidation resistance. The oxidation resistance mechanisms of MeC mainly depend on the formation of dense oxidation layer with good adhesion to the substrate by sintering of the oxide phase at high temperatures. Since the oxide phase sintering behavior of MeC is closely related to temperature, the practical applications of MeC are limited, such as insufficient

oxidation performance caused by the mismatch between the actual temperature and the service temperature. Many studies have shown that the introduction of SiC into the UHTCs can improve the mechanical properties, thermal shock resistance, and oxidation ablation resistance [161–164]. The introduced SiC can form silicate glass phase covering material with high viscosity, high melting point, low oxygen diffusion velocity, and low vapor pressure at high temperature, which prevents the further invasion of oxygen and can play a good protective role below 1600 ℃ [165]. UHTCs–SiC have become the focus of current research. By introducing the SiC phase, the oxidation resistance of MeC ceramics can be effectively improved [166].

Boride UHTCs have excellent oxidation resistance at low temperatures, but their oxidation resistance mechanism is completely different from that of carbides [167]. ZrB_2 begins to oxidize obviously at 700 ℃, and the formed oxide layer (B_2O_3) has good oxidation resistance below 1100 ℃. However, B_2O_3 will volatilize due to high vapor pressure when the temperature is higher than 1200 ℃, and the oxidation resistance will gradually lose. Parthasarathy *et al.* [168] developed a mechanistic model to interpret the oxidation behavior of the diborides of Zr, Hf, and Ti in the temperature range of 1000–1800 ℃ (Fig. 11). Good correspondence was obtained between the theory and experiments for weight gain, recession, and scale thickness as functions of temperature and oxygen partial pressure. It is revealed that at temperatures below about 1400 ℃, the rate-limiting step is the diffusion of dissolved oxygen through a film of liquid B_2O_3 in capillaries at the base of the oxidation product. While at higher temperatures, the B_2O_3 is lost by evaporation, and the oxidation rate is limited by Knudsen diffusion of molecular oxygen through the capillaries between nearly columnar blocks of the oxide, MO_2.

For ZrB_2–SiC, the main reactions involved during oxidation are as follows:

$$ZrB_2(s)+\frac{5}{2}O_2(g)\rightarrow ZrO_2(s)+B_2O_3(l) \quad (8)$$

$$SiC(s)+\frac{3}{2}O_2(g)\rightarrow SiO_2(s,l)+CO(g) \quad (9)$$

$$SiC(s)+O_2(g)\rightarrow SiO(g)+CO(g) \quad (10)$$

$$B_2O_3(l)\rightarrow B_2O_3(g) \quad (11)$$

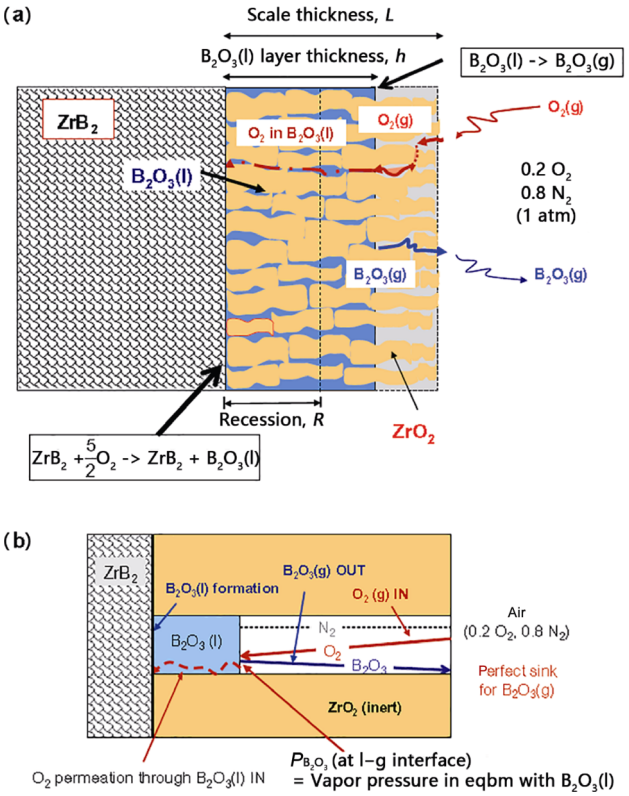

Fig. 11 Schematic diagram of mechanisms involved oxidation of ZrB_2 in air in the temperature range of 1000–1800 ℃ (a); schematic of the mechanistic steps considered in the oxidation model (b) developed by Parthasarathy *et al.* Reproduced with permission from Ref. [168], © Acta Materialia Inc. Published by Elsevier Ltd. 2007.

$$SiO_2(s,l)\rightarrow SiO_2(g) \quad (12)$$

$$ZrO_2(s)\rightarrow ZrO_2(g) \quad (13)$$

The oxidation reactions of SiC are relatively complex [169], and the transition temperature of SiC from passive to active oxidation in air is ~1734 ℃, which decreases significantly with the decrease of oxygen partial pressure. SiO_2 generated by passive oxidation has good antioxidant protection ability below 1850 ℃, and SiO_2 will fail because of rapid volatilization at a higher temperature. The introduction of 10–30 vol% SiC can significantly improve the oxidation resistance of UHTCs [170,171]. The refinement of grain size will lead to the improvement of the distribution uniformity of SiC, thus improving the oxidation resistance of the materials. In this way, SiO_2 can fill the pores more effectively and bridge the defects to block the entry of oxygen, thus improving the oxidation resistance of the material [172].

Fahrenholtz [164] developed a thermodynamic model to explain the formation of a SiC-depleted layer

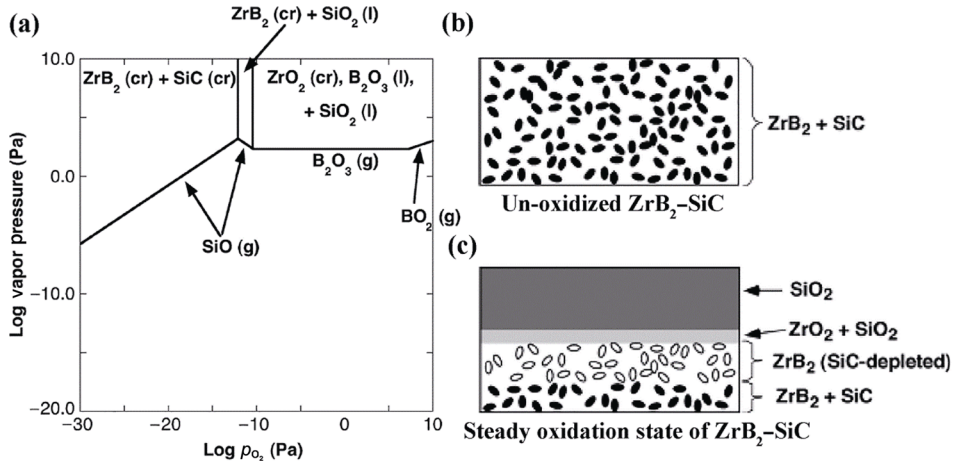

Fig. 12 Volatility diagram of ZrB_2–SiC at 1500 ℃ (a), schematic diagram of un-oxidized ZrB_2–SiC (b), and the steady oxidation state of ZrB_2–SiC at 1500 ℃ (c). Reproduced with permission from Ref. [164], © The American Ceramic Society 2007.

during ZrB_2–SiC oxidation in air at 1500 ℃. Based on the volatility diagrams (Fig. 12(a)), a thermodynamically stable structure (Fig. 12(c)) consisting of 1) a silica-rich layer, 2) a Zr-rich oxidized layer, and 3) a SiC-depleted zirconium diboride layer, was proposed to form for ZrB_2–SiC during oxidation. This is consistent with the experimental results very well. The SiC-depleted layer developed due to active oxidation of SiC. Diffusion of oxygen through the SiO_2-rich scale and the ZrO_2–SiO_2 layer is the rate limiting step of the overall process. Accordingly, the thickness of the outer scale should continue to increase with time due to the continued oxidation of SiC, which, in turn, increases the thickness of the SiC-depleted region in the underlying ZrB_2–SiC. The experimental research by Ni *et al.* [173] revealed that the formation of the SiC-depleted layer during oxidation is resulted from the active oxidation of SiC with C as an initial product. Lu *et al.* [174] further developed the volatility diagram of a ternary ZrB_2–SiC–ZrC (ZSZ) system to interpret the oxidation behavior of ZSZ ceramics. Based on the volatility diagram, the formation of ZrC-corroded and SiC-depleted layers and the oxidation sequence of each component in ZSZ during oxidation and ablation were well understood.

At ultra-high temperature oxidation environment (~2200 ℃), the oxide layer formed on ZrB_2–SiC shows a multi-layered structure [175] (Fig. 13). It includes: 1) oxidized outer layer, 2) dense ZrO_2 recrystallization layer, 3) porous oxide layer, 4) SiC depletion layer, and 5) unreacted bulk material. The outer layer is a porous ZrO_2 layer, and the second layer is a dense ZrO_2 layer formed by the recrystallization and sintering of ZrO_2 grains at high temperatures, which can effectively prevent the entry of oxygen and protect the inner bulk material from rapid oxidation. The third layer is a porous oxide layer, which is caused by the generation of high vapor pressure gas. The generated gas cannot be discharged in time, when its pressure exceeds the ambient pressure, it will form pores. This layer is the transition layer between the ZrO_2 recrystallization layer (the second layer) and the SiC depletion layer (the fourth layer). Due to the existence of a large number of pores and high vapor pressure gaseous oxides, coupled with the mismatch of thermal expansion coefficient between ZrO_2 and ZrB_2, the bonding strength between this layer and the SiC depletion layer is the weakest among all layers, and it is easy to crack and delaminate here. Therefore, this layer plays a key role in the high-temperature oxidation performance of the material. Below this layer, it is the SiC depletion layer, which is mainly composed of unreacted ZrB_2. During the oxidation process, its structure does not change significantly, and the original continuity does not change. The fifth layer is the unoxidized ZrB_2–SiC bulk material [163,176,177].

HfB_2 has higher melting point and thermal conductivity than ZrB_2, and the melting point of its oxidation product HfO_2 is also higher than that of ZrB_2 oxidation product ZrO_2. Accordingly, HfB_2 shows good oxidation resistance under ultra-high temperature environment [178]. Similar to ZrB_2-based UHTCs, the introduction of SiC into HfB_2 can effectively improve the mechanical properties and oxidation resistance of the materials [179,180]. Similar to ZrB_2–SiC composites, HfB_2–SiC and HfB_2–SiC–AlN after oxyacetylene test

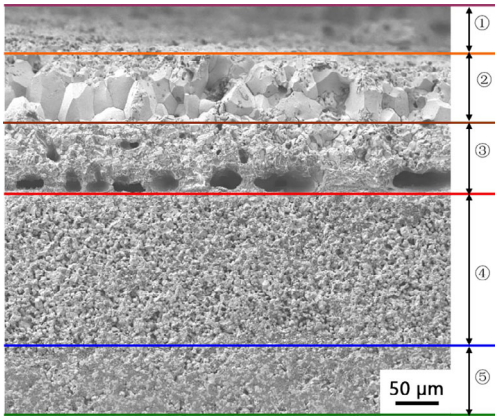

Fig. 13 Cross-section of ZrB_2–SiC after oxidation at 2200 ℃ for 10 min. Reproduced with permission from Ref. [175], © Elsevier Ltd. 2007.

also have an obvious layered structure: The entire oxide layer can be divided into three layers from surface: 1) outermost oxide layer, 2) oxide sub-layer, and 3) unreacted bulk [181]. Fahrenholtz *et al.* [18,164] pointed out that the oxygen atom transport into the SiC depletion layer is mainly by permeation, where active oxidation of SiC is occurred, with gaseous CO and SiO as the main products. Due to the existence of many pores, the structure of the SiC depletion layer is very loose, which is very easy to fall off under the action of external force, resulting in the absence of oxidation layer, adverse to the oxidation resistance of the materials [182].

The addition of AlN can promote the densification of HfB_2–SiC by removing the oxide layer on the surface of HfB_2 powders and inhibiting the grain growth of HfB_2 during sintering [181]. AlN can be oxidized to Al_2O_3 with a higher melting point than SiO_2, which can cover the surface of the material to play an oxidation resistance role at a higher temperature. Besides, Al_2O_3 and SiO_2 can form an aluminosilicate melt to fill the pores in the oxide layer formed by SiC active oxidation. The study by Zhang *et al.* [183] revealed that the addition of a W compound (i.e., WC) can improve the oxidation resistance of ZrB_2 remarkably. During oxidation, the presence of WO_3 in the oxide scale resulted in liquid phase sintering of ZrO_2, which modified the microstructure of the scale and increased its relative density. As a result, WC-containing ZrB_2 had improved oxidation resistance compared with nominally pure ZrB_2. This provides a new approach for UHTC design with improved oxidation resistance.

On the other hand, Ni *et al.* [184,185] developed highly textured MB_2-based UHTCs based on strong magnetic field alignment, which present anisotropic oxidation resistant properties due to the intrinsic anisotropy of diborides. Better oxidation resistance is achieved on the sample surface perpendicular to the *c*-axis of MB_2 [184–187]. Preliminary investigation suggests that mass transmission (such as oxygen and SiO) anisotropy is an important factor for the anisotropic oxidation resistance. This provides a new selection for the design and application of UHTCs.

With the continuous improvement of hypersonic technology, the thermal protection systems and materials have become key factors restricting the further development of hypersonic vehicle. UHTCs are receiving more and more attention due to their excellent high-temperature comprehensive performance. However, in order to truly achieve engineering application, the inherent brittleness of UHTC is the core scientific problem that must be solved. The introduction of particles, whiskers, and short fibers cannot provide a stable toughened skeleton, and the toughening effect cannot meet the service requirements. The UHTCMCs combining UHTCs and continuous fibers are expected to fundamentally overcome the inherent brittleness of bulk UHTCs, and have become the main development trend and research hotspot at present and in the future, which is the focus of the subsequent section.

3 Ultra-high temperature ceramic matrix composites (UHTCMCs): Components, processing, and properties

Combining the unique properties of the UHTCs with the concepts of ceramic matrix composites, a new class of materials known as fiber reinforced UHTCMCs are developed. The UHTCMCs are endowed with excellent mechanical properties and ablation resistance at ultra-high temperatures, and furthermore, overcoming the inherent brittleness and poor thermal shock resistance of bulk UHTCs. Therefore, UHTCMCs are currently considered as the most potential candidates for applications in thermal structures and anti-ablation components of hypersonic vehicles, such as sharp noses, leading edges, and combustor of solid rockets.

3.1 Components of the UHTCMCs

Generally, UHTCMCs are composed of fiber reinforcements, interphase/interface, and UHTC matrix, which need to be selected and combined properly to

achieve the desired properties. This section focuses on the properties and compatibility of fibers, interphase, and matrix for UHTCMCs.

(1) Fiber reinforcements

In fiber-reinforced UHTCMCs, fibers are designed to overcome the brittleness and poor thermal shock resistance of the monolithic UHTCs. Furthermore, the fibers must also be able to withstand the extremely high temperature and harsh environment, in which thermal and oxidation stability are required. The type of fiber reinforcements influences the mechanical properties significantly, especially fracture toughness, and it also affects the fabrication processing. Due to the relatively low cost and better ultra-high temperature properties, carbon fibers are the most commonly reinforcements for UHTCMCs currently. Very few works have also been conducted on the SiC fiber-reinforced UHTCMCs. However, the poor oxidation resistance properties of carbon fibers and the limited high-temperature resistance of SiC fibers intrinsically restrict the performance of UHTCMCs under more extreme conditions. Developing UHTC fibers with superior thermal and oxidation stability becomes critical for further improving the properties of UHTCMCs [188,189]. Up to now, only the US Matech GSM (Matech Global Strategic Materials Inc., California, USA) has reported their development of UHTC fibers, such as HfC fibers, TaC fibers, and UHTC fibers reinforced UHTC matrix composites [190]. However, the commercially available UHTC fibers have rarely been reported.

Earlier research paid some attention to the chopped fiber-reinforced composites due to the simple fabrication process (Fig. 14). However, chopped fibers are vulnerable when mixing with ceramic powders. And, the poor dispersibility of fibers results in limited

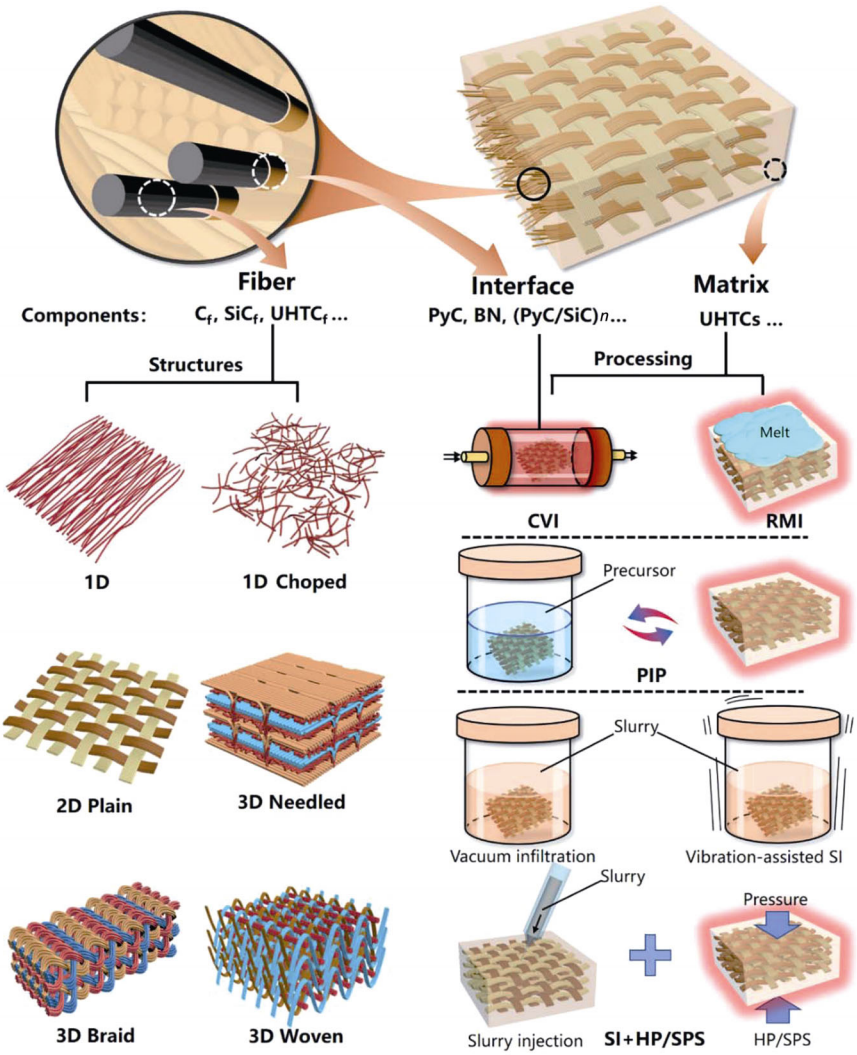

Fig. 14 Schematic diagram of the components and processing of UHTCMCs.

mechanical properties of the composites [191–193]. Accordingly, continuous fiber reinforcements with different weaving modes are developed for high-performance UHTCMCs. The fibers in 2D preform are usually stacked in different directions. The composites with 2D fiber reinforcements present higher mechanical strength along the fiber directions but poor interlayer shear strength [163,194–198]. 3D fiber preforms, mainly contain needled, woven, braid fiber preforms, etc. (Fig. 14), exhibit better mechanical properties. Currently, 3D preforms are the most widely used reinforcements for UHTCMC fabrication [199–203].

Even though the composites are reinforced with continuous fibers, the inter-bundle and the inter-laminar matrix also show a brittle behavior at the micron scale. Accordingly, some research has been conducted by introducing one-dimensional nanostructure, such as carbon nanotubes (CNTs), boron nitride nanotubes (BNNTs), and SiC nanowire (SiCNWs), into the matrix to develop hierarchically reinforced composites [204,205].

(2) Interphase/interface

Interphase/interface between fibers and matrix is another key component of UHTCMCs, which determine the mechanical behavior and oxidation resistance properties of UHTCMCs to a certain extent. Generally, the interface on fibers is deposited by chemical vapor infiltration before introducing ceramic matrix. The vulnerable fibers can be protected by interphase. Moreover, weak interphase is necessary to toughen the composites by crack deflection, interface debonding, and fiber pull-out when the load is applied on the composites. Pyrolytic carbon (PyC) with layered structure and PyC/SiC are the most widely used interphase for UHTCMCs, which play a critical role in damage tolerance of the composites [206]. h-BN has very similar layered structure, elasticity, and fracture properties to PyC. Recently, the BN/SiC multilayer interphase has also been developed to improve the oxidation resistance of the composites by forming borosilicate glass which can seal the cracks and prevent the inward diffusion of oxygen in oxidized environment. However, the oxidized product of BN, B_2O_3, volatilizes violently at temperatures higher than 1100 ℃, resulting in the decrease of oxidation resistance [207]. To further improve the oxidation resistance of the BN interphase, NASA modified BN with Si and fabricated Si-doped BN interphase [208]. More researchers prefer to fabricate multilayer interphase to improve the properties of composites. Take PyC and PyC/SiC multilayer interphase in C_f/SiBCN composites as an example, PyC interface reacts with SiBCN matrix and forms ring-like defects at temperatures higher than 1600 ℃, leading to the serious degradation of mechanical properties (from 370 MPa at room temperature to 92 MPa at 1600 ℃). For the C_f/SiBCN composites with $(PyC/SiC)_3$ multilayer interphase, the reactions can be retarded effectively and the intact interphase ensures the excellent properties of the composites. The flexural strength of the composites is maintained to 330±10 MPa at 1600 ℃ [200,209]. In summary, the development of proper interphase is critical for performance optimization of UHTCMCs.

(3) UHTC matrix

UHTC matrix are the main components of UHTCMCs, where the carbides and borides of Zr, Hf and Ta have been extensively studied. In particular, Zr and Hf-based UHTCs are the most used matrix due to the high melting points of themselves and their oxides. For Ta-based UHTCs, the low melting point of their oxides (~1800 ℃ for Ta_2O_5) restrict their ultra-high temperature applications to some extent. The oxidation and ablation resistance of UHTCMCs not only depends on the composition of the matrix, but also depends on the microstructure of the formed oxide layer. Compared to the carbide UHTCs, borides possess better oxidation resistance in a wide temperature range below 1100 ℃ due to the formation of glassy B_2O_3 [195,210–215].

A dense oxide layer with limited oxygen diffusion rate is necessary to maintain an effective protection. Therefore, additives into the UHTC matrix to modify the oxide layers have been investigated. Based on the results of bulk UHTCs, SiC is the most used second phase to improve the oxidation and ablation resistance of the UHTCMCs, which can form a dense glassy SiO_2 layer during oxidation and ablation. The glassy phase with a low viscosity can fill in the cracks or pores in oxide layer and prevent oxygen inward diffusion [198,216,217]. However, the vast evaporation of SiO_2 at ablation temperature above 2200 ℃ results in failure of the oxide protective layer. In recent years, rare earth oxides and TiC are introduced into the matrix to stabilize the ablation oxides and increase the melting point of silica to further improve the ablation resistance of UHTCMCs [218–220]. In addition, SiBCN-based composites have also been studied for high-temperature

structural applications. However, the ablation resistance is limited due to the lack of UHTC components [200,221–224]. Recently, a novel $C_f/Zr_{0.8}Ti_{0.2}C_{0.74}B_{0.26}$ composite is reported with superior ablation resistance [210].

3. 2 Processing and microstructures of UHTCMCs

Various processing methods have been developed for UHTCMC fabrication. Chemical vapor infiltration/deposition (CVI/CVD), precursor infiltration and pyrolysis (PIP), slurry infiltration (SI), and reactive melt infiltration (RMI) are the most commonly used methods. Slurry infiltration combined with subsequent sintering treatment, such as HP and SPS, have also been developed recently to fabricate dense UHTCMCs. The advantages and disadvantages of the different processing routes are discussed in this section.

(1) Chemical vapor infiltration/deposition (CVI/CVD)

CVI/CVD is a process which introduces reactive gases into porous fiber preforms to form the ceramic matrix of fiber-reinforced composites (Fig. 15). By introducing various reactive gases, CVI/CVD can be widely applied to fabricate C, SiC, and other UHTC matrix, such as HfC, ZrC, and ZrB_2 [5,225]. The CVI/CVD process is generally a relatively low temperature (900–1400 ℃) and low-pressure densification processing route compared with other advanced manufacturing methods and can be very versatile, which prevents the heat damage to fibers [226]. The CVI/CVD-derived ceramic matrix with high purity, high crystallinity, and near stoichiometry generally possesses more excellent mechanical, anti-oxidation and anti-ablation properties [227]. However, the CVI/CVD process typically takes 2–3 months to achieve required densities and is therefore highly expensive [228,229]. As a result, almost no UHTCMCs fabricated completely by CVI/CVD have been reported, but it is a very common method for interphase and partial matrix fabrication.

(2) Precursor infiltration and pyrolysis (PIP)

PIP is a green-forming procedure to introduce UHTC matrix involving infiltration of a low viscosity liquid chemical precursor into fiber preforms and subsequent pyrolysis at elevated temperatures to yield ceramics (Fig. 16(a)). Compared with CVI, PIP has a larger infiltration depth and lower cost [230], and is the most widely used processing for UHTCMCs, particularly for large-size component fabrication. Due to the evolution of gaseous byproduct and volume shrinkage from precursor to ceramic, the formed ceramic matrix generally appears a porous structure (Figs. 16(b) and 16(c)) [231,232]. Generally, the infiltration and pyrolysis must be performed iteratively many times, until a matrix of the desired or otherwise limiting density is achieved [229]. Polycarbosilane (PCS) is the most common precursor used for SiC matrix [233]. Recently, the precursors for UHTCs matrix, such as zirconium butoxide for ZrC [234,235]

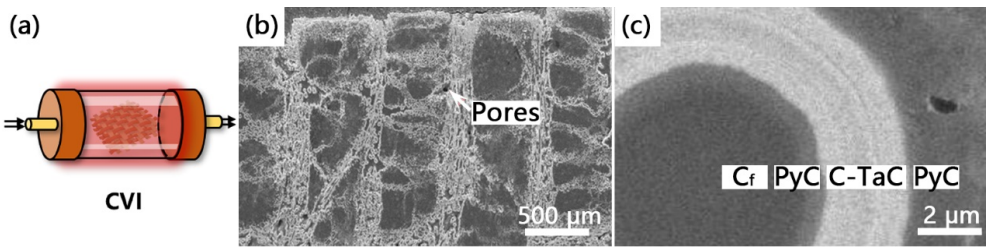

Fig. 15 Schematic diagram of CVI (a); microstructure of CVI–C_f/C–TaC (b, c). Reproduced with permission from Ref. [214], © Elsevier B.V. 2013.

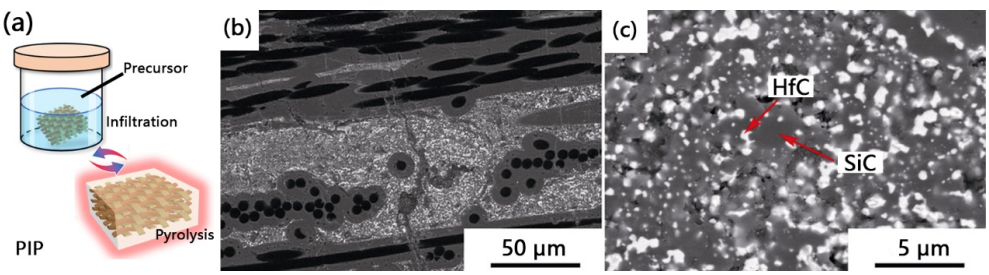

Fig. 16 Schematic diagram of PIP (a); microstructure of PIP–C_f/HfC–SiC composites (b, c). Reproduced with permission from Ref. [232], © The Author(s) 2020.

and organic zirconium-containing polymer for ZrB_2 [236], have also been developed, which makes PIP more flexible to fabricate UHTCMCs. A high ceramic yield from precursors is important and the precursor choice is critical for PIP processing optimization.

(3) Slurry infiltration (SI)

For SI processing, slurry composed of ceramic powders, solvent, and dispersant is impregnated into the porous preform. Then, the solvent and organic components are removed during drying and de-binding. The quick and simple process makes SI the cheapest method for UHTCMC fabrication. However, due to the hindering effect of fibers, ceramic powders cannot be infiltrated uniformly into fiber preform and the infiltration depth of the powders is very limited. To improve the infiltration efficiency, slurry injection and vibration-assisted slurry impregnation were developed. Baker *et al.* [228] reported the slurry injection firstly (Fig. 17(a)), where the slurry penetrates much deeper in the preform than conventional vacuum impregnation (Figs. 17(b) and 17(c)). However, the injection process presents limited filling effect at the edges of the preform. Therefore, the joint process of vacuum impregnation and slurry injection can get a denser composite with homogenous matrix distribution. Hu *et al.* [176,237] reported vibration-assisted slurry impregnation for 3D needled-punched carbon fiber preforms (Fig. 18(a)). The process is conducted in a vacuum tank, and the vibrating frequency is 60 Hz. The as-fabricated UHTCMCs show uniform component distribution and less open porosity (Figs. 18(b) and 18(c)). Consequently, the mechanical properties of composites fabricated by vibration-assisted slurry impregnation are improved as expected.

(4) Reactive melt infiltration (RMI)

RMI is another common method used to introduce UHTC matrix into porous preforms by infiltrating molten metals/alloys and *in-situ* reactions with the pre-matrix carbon or boron phase [238]. The process can get a near fully dense matrix with limited pores (Fig. 19). Therefore, composites usually perform better ablation resistance [209,239]. Compared with CVI and PIP methods, the RMI process is more efficient and costs less, which is beneficial for commercialization production [240,241]. Based on RMI processing route, mass production of SiC_f/SiC composite and components have been reported by General Electric for advanced CFM LEAP engine since 2016 [5]. However, fiber/interphase degradation is very common during RMI, which results in poor mechanical properties [242]. For the first time, Chen *et al.* [243] analyzed the interphase degradation behavior of RMI-UHTCMC systematically. It is revealed that chemical reaction and physical melting are the main interphase degradation

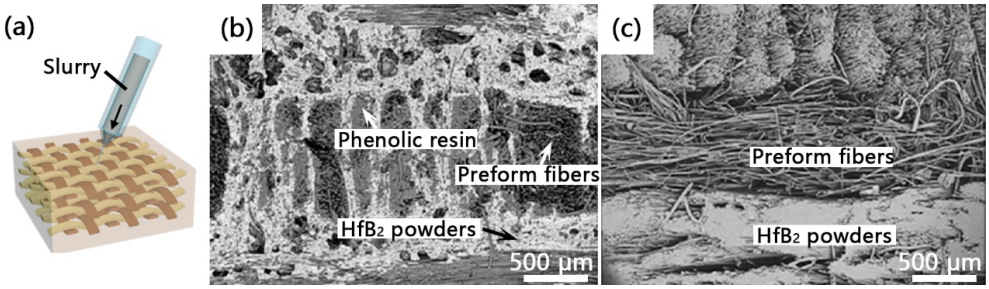

Fig. 17 Schematic diagram of slurry injection (a), microstructure of the C_f/HfB_2 composites fabricated by slurry injection (b), and slurry impregnation (c). Reproduced with permission from Ref. [228], © Elsevier Ltd. 2019.

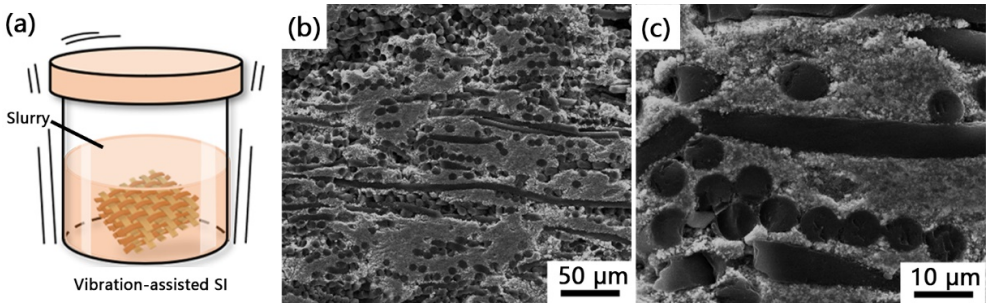

Fig. 18 Schematic diagram of vibration-assisted slurry impregnation (a); microstructures of the C_f/ZrB_2–SiC composites fabricated by vibration-assisted slurry impregnation (b, c). Reproduced with permission from Ref. [176], © Elsevier Ltd. 2018.

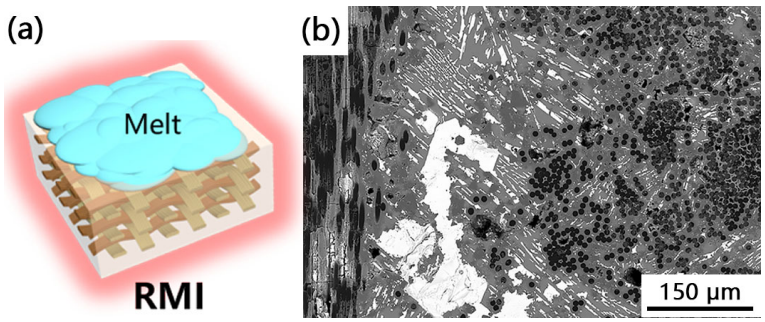

Fig. 19 Schematic diagram of RMI (a); typical microstructure of RMI–C_f/ZrC–SiC composites (b). Reproduced with permission from Ref. [209], © The American Ceramic Society 2018.

mechanisms involved during RMI. Besides, residual metallic phase results in the decrease of mechanical and anti-ablation properties when the composites are operated at high temperatures [244].

The melt infiltration kinetics in terms of porous preform structure can be established to quantitively evaluate the microstructure evolution of the composites. Levenspiel [245] developed a mathematical model to express the relationship between pore size and infiltration time by assuming the reduction of pore size during RMI is a diffusion-limited process:

$$t=\frac{M_{\mathrm{M}}\cdot\rho_{\mathrm{A_PB_M}}\cdot r_0^2}{6\cdot M_{\mathrm{A_PB_M}}\cdot\rho_{\mathrm{M}}\cdot D_{\mathrm{A_P/A_PB_M}}}\left[1-3\left(\frac{r}{r_0}\right)^2+2\left(\frac{r}{r_0}\right)^3\right] \quad (14)$$

where M_{M}, $M_{\mathrm{A_PB_M}}$, ρ_{M} and $\rho_{\mathrm{A_PB_M}}$ are the molar weights of melt (M) and A_PB_M, densities of melt (M) and the reaction product (A_PB_M), respectively. $D_{\mathrm{A_P/A_PB_M}}$, t, r, and r_0 are the diffusion coefficient of reaction atoms in reaction layer, reaction time, transient, and initial pore radius of the preform, respectively. r_0 is calculated based on Dullien formula:

$$r_0=\frac{1}{3}\left(\sum_{i=1}^{k}r_i\right)^2\left[\sum_{i=1}^{k}r_i\sum_{j=1}^{k}\left(\frac{r_i}{r_j}\right)^3\right]^{-1} \quad (15)$$

where r_i (i = 1, 2,..., k) is the characteristic pore radius measured by mercury porosimeter. The r–t curves of the particular composites can be calculated by Eqs. (14) and (15). The critical time (t_c) is determined by r–t curves at r = 0. The longer the t_c is, the kinetically more favorable the melt infiltration is. Consequently, more sufficient melt can be infiltrated into the preform to form a more uniform phase distribution. Accordingly, the microstructure of the RMI-derived composites can be approximately predicted by r–t curves [246].

(5) Slurry infiltration combined with subsequent sintering

Generally, UHTCMCs are not compulsorily required to sinter/consolidate like bulk ceramics. Recently, pressure assisted sintering processes like HP and SPS (Fig. 20(a)) are also used for the subsequent consolidation of UHTCMCs to improve their densification [247,248]. However, high temperature and pressure can lead to the damage of fibers and interphase (Figs. 20(b) and 20(c)) [248,249]. Zhang *et al.* [163] reduced the sintering temperature to 1450 ℃ by using nanosized ceramic powders and prevented the degradation of fibers to some extent. Zoli *et al.* [250] pointed out that the degradation of fibers caused by SPS can be alleviated by optimizing the interphase layer and the sintering parameters.

To avoid the disadvantages of the different processing methods, more researchers prefer to fabricate UHTCMCs using hybrid processing route. Servadei *et al.* [229]

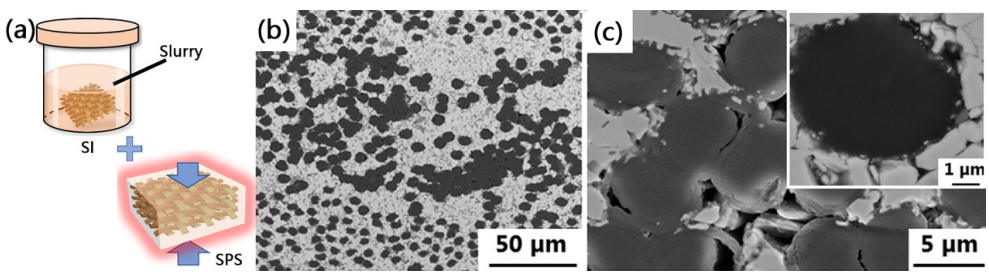

Fig. 20 Schematic diagram of vacuum slurry impregnation and SPS (a); microstructure of the polished SPS–C_f/ZrB_2–SiC composites (b, c). Reproduced with permission from Ref. [250], © Elsevier Ltd. 2019.

fabricated dense C_f/ZrB_2–SiC composites with low defectiveness by ZrB_2 slurry infiltration coupled with polymer infiltration and pyrolysis. Yao *et al.* [251] fabricated C_f/C–SiC–ZrC composites by a joint CVI and PIP process, and the composites show better mechanical, anti-oxidation and anti-ablation properties. Zhang *et al.* [163,252,253] fabricated C_f/ZrB_2–SiC composites by SI, PIP, and HP processes which avoid the fiber/matrix reactions and improve the fracture toughness. Ni *et al.* [209,239] fabricated C_f/ZrC–SiC composites by sol–gel and RMI which effectively improves the mechanical and ablation resistance of the composites.

3. 3 Microstructure, mechanical and thermal properties of UHTCMCs

Composites are toughened by fiber pull-out and crack deflection at the interphase. When the force is applied on the UHTCMCs, the load is transferred from the matrix to the fibers. For the 2D laminated C_f/ZrB_2–SiC, the special distribution of fibers and matrix induces higher residual stress in the matrix, which increases the number of cracks and reduces the matrix modulus [249]. Due to the weak bond among fiber layers, composites reinforced with 2D fiber preform generally show low interlaminar shear strength. This can be improved by adding vertical fibers or using 3D fiber preforms [254,255]. In addition, an intact interphase with suitable thickness is also required for excellent mechanical properties [256]. Multi-layer interphase has been proved beneficial for fibers protection and mechanical property improvement of the composites [257]. Typical properties of UHTCMCs fabricated by various processing routes are summarized in Table 4.

Table 4 Typical properties of UHTCMCs fabricated by various processing routes

Material	Processing	Density ($g\cdot cm^{-3}$)	Open porosity (%)	Flexural strength (MPa)	Elastic modulus (GPa)	Ablation method	Temperature (℃)		Ablation time (s)	Heat flux ($MW\cdot m^{-2}$)	Ablation rate	Ref.
							Flame	Surface				
3D-C_f/C–TaC	CVI	5.48	5	196.8								[214]
3D-C_f/ZrB_2–SiC	SI+HP	2.93	3.7	169±12								[176]
1D-C_f/ZrB_2–SiC	SI+HP	3.8	10	320±10								[250]
1D-C_f/ZrB_2–SiC	SI+SPS	4.0	5	260±20								
2.5D-C_f/HfB_2–C	Slurry injection + CVI	3.2±0.16	16	121.4±18.3	28.3±3.2							[196]
2D-C_f/ZrB_2–SiC	SI+PIP	3.2	6	491±44	220±9							[229]
3D-C_f/ZrB_2–SiC	Vibration-assisted SI+HP	4.10	2.6	204±18								[176]
2.5D-C_f/C–ZrC–SiC	CLVD					OAT	~3000		60	4.18	1210 $mg\cdot s^{-1}$ 1160 $\mu m\cdot s^{-1}$	[258]
2D-C_f/C–HfB_2	PIP+CVI	1.77–1.84				OAT		~2150	90	4.18	2.75 $g\cdot m^{-2}\cdot s^{-1}$ 3.14 $\mu m\cdot s^{-1}$	[211]
2D-C_f/ZrB_2–SiC	SI+PIP	2.15	~8.6			Plasma torch		2500	300		3.07 $g\cdot m^{-2}\cdot s^{-1}$ 1.05 $\mu m\cdot s^{-1}$	[259]
3D-C_f/C–SiC–ZrC	PIP	1.94	8.5			Plasma torch		2300	60		0.56 $mg\cdot s^{-1}$ 16.33 $\mu m\cdot s^{-1}$	[260]
3D-C_f/ZrC–SiC	PIP	2.11	15	136.0±13.1	31.8±2.6	OAT	~3000		40	4.2	8.8±0.4 $mg\cdot s^{-1}$ 23±1 $\mu m\cdot s^{-1}$	[230]
3D-C_f/ZrC–SiC	PIP	2.13	18	142.4±17.5	19.2±2.9	OAT	3000		80	4.2	11.7 $mg\cdot s^{-1}$ 31.8 $\mu m\cdot s^{-1}$	[231]
3D-C_f/HfC–SiC	PIP	3.18±0.04	13.2±0.4			Plasma wind tunnel		1706–2454	600		0.87 $mg\cdot s^{-1}$ 0.067 $\mu m\cdot s^{-1}$	[232]
3D-C_f/ZrC–SiC	PIP	2.18	4.9	749±15	141±12							[233]
3D-C_f/ZrC–SiC	RMI	2.64	3.5			Plasma torch		~1890	60	4.02	6.97 $mg\cdot s^{-1}$ 0.29 $\mu m\cdot s^{-1}$	[239]
3D-C_f/ZrC–SiC	RMI	2.52	1.7	380	61							[209]
3D-C_f/SiC–ZrC–TiC	RMI	3.25	9.7			OAT		2500	60		0.008 $mg\cdot s^{-1}$ 0.000 $\mu m\cdot s^{-1}$	[219]
3D-C_f/C–SiC–ZrC	RMI	2.42	5.0	143.5±11.2	13.4±3.3	OAT		~2400	60	4.18	1.21±0.33 $mg\cdot s^{-1}$ 5.90±0.90 $\mu m\cdot s$	[240]

The microstructure and mechanical properties of UHTCMCs depend greatly on the processing methods and the form of the reinforcements. Introducing ceramic powders into fiber preforms does not always result in a homogeneous distribution of the UHTC phase. This is very common for the composites reinforced with 2D plain cloth or more complex fiber preform. UHTC powders prefer to concentrate among fiber bundles due to the poor infiltrating effect inside the fiber bundles. Therefore, composites fabricated by SI generally need to be further densified and the as-fabricated composites possess an inhomogeneous phase distribution in the matrix area. For example, 2D plain cloth infiltrated with ZrB_2 slurry is densified by PIP process which results in the concentration of ZrB_2 in inter-bundle area and SiC in intra-bundle area (Fig. 21) [198,261]. This particular microstructure results in weak interlaminar bonding strength and thermal mismatch between the fiber bundles and matrix.

The UHTC matrix formed by PIP experiences volume shrinkage combining with the gas release. As a result, pores and cracks are very common in the composites [237,262]. Take the C_f/C–ZrC–SiC–ZrB_2 composites fabricated by SI and PIP as an example. The CTE of PyC interphase is higher than that of carbon fibers. Carbon fibers are compressed by PyC interphase at ambient temperature and are stretched at the temperature above 1100 ℃ along the radial and axial directions. Therefore, the bond of fiber and interphase is enhanced at ambient temperature and weakened at the temperatures above 1100 ℃ (Fig. 22(a)). The weaker bond of fiber-interphase at high temperatures benefits to the crack deflection, fiber breakage, and pull-out. Consequently, the tensile strength of the composites at 1700 ℃ is higher than that at ambient temperature (Figs. 22(b)–22(d)). However, the mechanical properties of the composites decrease above 1800 ℃ due to the fiber damage and looser matrix at elevated temperature [263].

The composites fabricated by SI and further densified by subsequent HP or SPS possess higher density and lower porosity [264–266]. Due to the high sintering temperature and pressure (up to 1900 ℃, 40 MPa), the reactions between oxide impurity on the powder surface and fibers cannot be ignored. Generally, the fibers react with oxide impurities and result in chemical etching. Strong bonding between fibers and matrix is formed (Fig. 20(c)), which results in the failure of fiber pull-out and crack deflection. As a result, the composites possess a low flexural strength and fracture toughness. Coating PyC interphase with a suitable thickness on the fibers is an effective way to mitigate the chemical etching and offers a weak bonding to improve the toughness [249,267,268]. On the other hand, the high sintering temperature and pressure result in high residual stress in the composites, which can be released at high temperatures. Therefore, the mechanical properties increase with the increase of temperature. Furthermore, the grain boundary of the ceramic matrix tends to slide at high temperatures, which results in the plastic deformation of the composite [265].

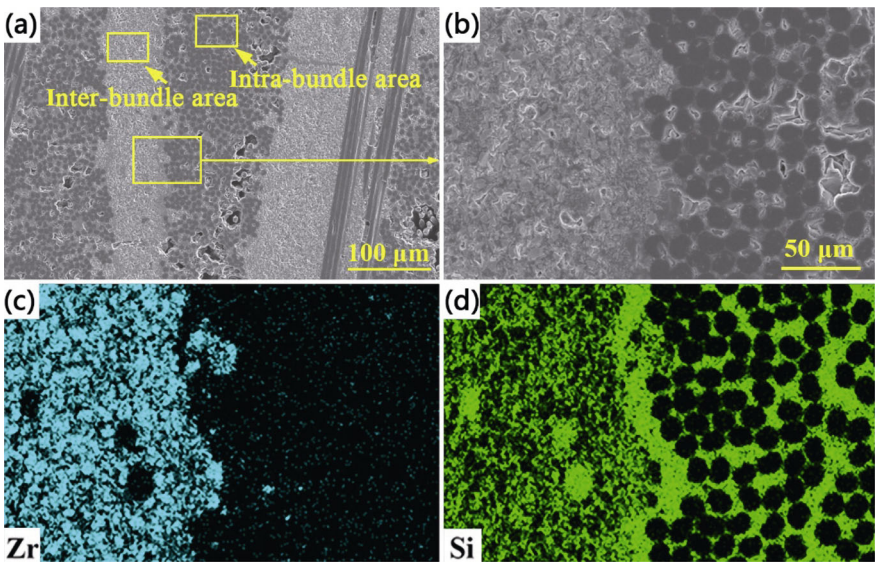

Fig. 21 Microstructures of 2D-C_f/ZrB_2–SiC composites (a, b), and the EDS analysis of (b) (c, d). Reproduced with permission from Ref. [198], © Elsevier Ltd. 2020.

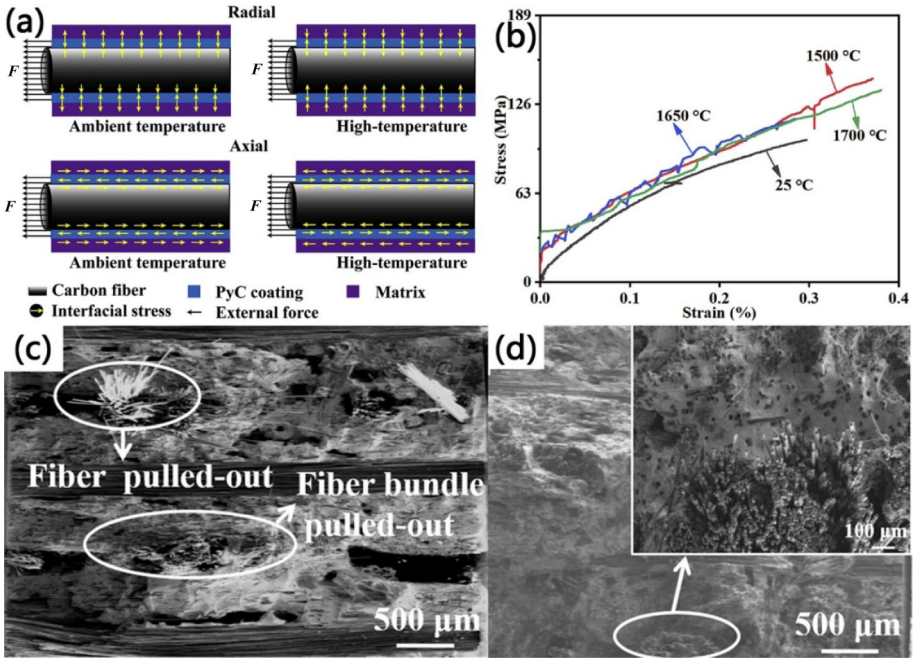

Fig. 22 Interphase stress distribution at ambient temperature and high temperature (a), stress–strain curves of C_f/C–ZrC–SiC–ZrB_2 composites during tensile test at different temperatures (b), and fracture surfaces of C_f/C–ZrC–SiC–ZrB_2 composites after tensile test at ambient temperature (c) and 1700 ℃ (d). Reproduced with permission from Ref. [263], © Elsevier B.V. 2019.

As discussed above, UHTCMCs fabricated by CVI are rarely reported. The limited infiltration depth results in large pores in the UHTCMCs (Fig. 15) [269,270]. For the UHTCMCs fabricated by RMI, they normally show high matrix density and low porosity. However, bulk metal and carbon residues generally exist in the composites due to kinetic factors. Moreover, the metal melt usually erodes fibers and interphase during RMI. As a result, the composites exhibit brittle fracture characteristics. Therefore, optimizing interphase structure and RMI kinetics are critical for enhanced mechanical properties of the UHTCMCs fabricated by RMI [271]. Ni *et al.* [209] developed a novel RMI route for C_f/ZrC–SiC fabrication by infiltrating Si melt into nano-porous C_f/ZrC–C preforms, where the nano-porous C_f/ZrC–C preforms were prepared through a colloid process, with a ZrC "protective coating" formed surrounding the carbon fibers. The ZrC "coating" can protect the fibers and interphase to a certain extent from high-temperature Si melt erosion during RMI process (Fig. 23). Besides, the well distributed nano-porous structure is beneficial to forming a dense composite with limited Si residue during RMI process. Moreover, the needle-shaped $ZrSi_2$ grains formed during the cooling stage which act as reinforcement of the matrix (Fig. 19(b)). Consequently, flexural strength of the composites is as high as ~380 MPa, which is much higher than those UHTCMCs fabricated by conventional RMI method.

Chen *et al.* [272] fabricated C_f/ZrC composites by introducing Zr melt into C_f/C preform through RMI. It is indicated that there is ~4.2 vol% residual Zr is present

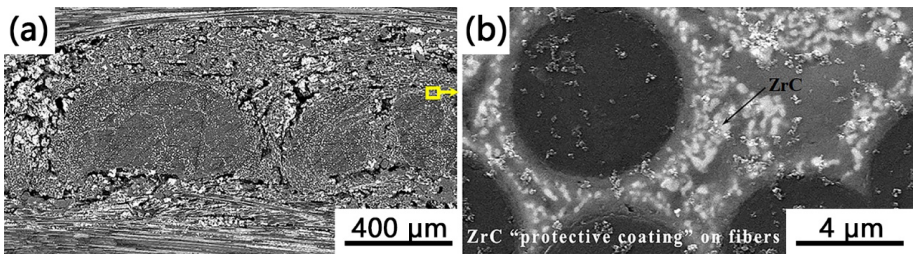

Fig. 23 Microstructure of the nano-porous C_f/ZrC–C preforms, with a ZrC "protective coating" formed surrounding the carbon fibers: low magnification of C_f/ZrC–C preform (a) and ZrC "protective coating" surrounding carbon fibers (b). Reproduced with permission from Ref. [209], © The American Ceramic Society 2018.

in the RMI–C_f/ZrC, which is harmful to the high-temperature mechanical properties. Subsequent high-temperature annealing at ~1600 ℃ can properly consume the residual Zr and get an optimum flexural strength of 192 MPa. However, at higher heat-treatment temperatures, fiber deterioration will become serious and lead to the decrease of strength.

Thermal properties, such as thermal expansion coefficient (CTE), thermal diffusivity, thermal conductivity, and specific heat, are critical to UHTCMCs and are significantly affected by phase content and microstructure of the composites. The vast difference of CTE between fibers and ceramic matrix induces residue stress and cracks in composites after the fabrication process. As a result, the strength and elastic modulus of conventional UHTCMCs are relatively lower than SiC_f/SiC composites. Chen *et al.* [273] designed a porous SiC coating in C/ZrC to mitigate the CTE mismatch and thermal stress between C fibers and ZrC matrix, which effectively enhanced the mechanical properties of the composites. Carbon fibers have highly anisotropic thermal properties along different directions. Generally, the axial CTE of carbon fibers is negligible and the radial CTE is ~10×10^{-6} ℃$^{-1}$. Due to the anisotropic 3D stacked structure in the fiber preforms, the thermal properties of the composites show significant differences among different directions. UHTCMCs with particular thermal properties can be designed by modifying microstructure and components [21].

3. 4 Oxidation and ablation behavior of UHTCMCs

(1) Oxidation behavior and mechanisms of UHTCMCs

Oxidation and ablation resistant properties are critical for the practical application of UHTCMCs. Generally, the oxidation and ablation resistance of UHTCMCs are dependent much on the composition and microstructure of the oxide layers formed on the surface, which might protect the composites from further oxidation/ablation damage. The UHTCMCs with ZrB_2–SiC matrix show familiar oxidation behavior with bulk UHTCs which form a dense outside layer, ZrO_2–SiO_2 middle layer and SiC depleted layer [274]. Tang *et al.* [24] analyzed the oxidation behavior of C_f/ZrB_2–SiC composites. It is indicated that B_2O_3 formed from the oxidation of ZrB_2 matrix under 1000 ℃. The glassy B_2O_3 phase plays a positive role in oxidation resistance by covering the underneath composites and filling the pores and microcracks. However, the vast evaporation of B_2O_3 and limited SiO_2 formation under 1200 ℃ result in the less protection capability of the oxide layer. With the increase of temperature, adequate glassy SiO_2 with low viscosity formed which can also cover the composites, fill the pores and cracks to reduce the oxygen diffusivity of the oxide layer. Consequently, the oxidation resistance of the composites remains stable at 1200–1400 ℃ (Fig. 24) [24,275].

Vinci *et al.* [216] investigated the influence of SiC content on the oxidation behavior of C_f/ZrB_2–SiC

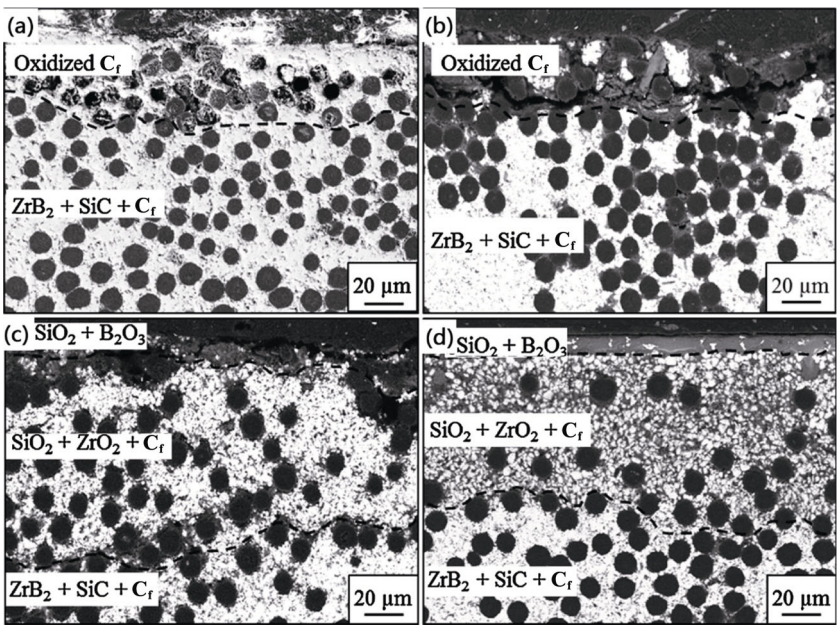

Fig. 24 Cross sections of C_f/ZrB_2–SiC after 6-h oxidation in flowing air at 800 ℃ (a), 1000 ℃ (b), 1200 ℃ (c), and 1400 ℃ (d). Reproduced with permission from Ref. [275], © The Authors 2017.

composites at higher temperature (1500 and 1650 ℃). For the composites with the SiC content less than 5 vol%, the formed oxide layer has limited glassy SiO_2, leading to the excessive oxidation of the carbon fibers and rupture of the oxide layer. The porous oxide layer possesses a limited protective effect and results in the further oxidation of the underneath material. For the C_f/ZrB_2–SiC with SiC content more than 15 vol%, dense borosilicate layer could be formed to the whole composites, leading to the improvement of the oxidation resistance (Fig. 25). Accordingly, C_f/ZrB_2–SiC composites with SiC content above 15 vol% is needed to get an ideal anti-oxidation property.

Y_2O_3 addition is expected to improve the oxidation resistance of C_f/ZrB_2–SiC through enhancing the sintering process and forming a denser ZrO_2 layer on the oxidation surface. The Y-based secondary phases promoted the growth of ZrO_2 grains at 1500 ℃. The large ZrO_2 grains are surrounded by yttrium borate on the surface, and the inner oxide layer is $ZrO_2/SiO_2/YBO_2$ phase. However, as the temperature rises to 1650 ℃, the outer oxide layer becomes porous due to the partial evaporation of low melting phases coupled with insufficient SiO_2 protective layer (Fig. 26). As a result, oxidation resistance degrades after adding Y_2O_3. But, the influence of the Y_2O_3 content on the oxidation resistance has not been well investigated, which is of significance to be analyzed in the further research [276].

Compared with ZrB_2–SiC matrix composites, UHTCMCs with ZrC–SiC matrix have a similar oxidation behavior. However, due to the lack of glassy phase and the release of CO, CO_2 by ZrC oxidation, the UHTCMCs with ZrC–SiC matrix have a more porous and less protective oxide layer below 1200 ℃. Therefore, C_f/ZrC–SiC has worse oxidation resistance than C_f/ZrB_2–SiC composites [5,251]. Adding 2 wt% La_2O_3 in ZrB_2– and HfB_2–20 vol%SiC matrix can increase the viscosity of glassy borosilicate melt and lower the oxygen diffusion coefficient at the temperature range of 1400–1600 ℃, leading to improved oxidation resistance [277].

TaC is another matrix component that is chosen to bear oxidation. Chen *et al.* [278] investigated the oxidation behavior of the C_f/C–TaC composites. After 40 min oxidation at 1200–1600 ℃, a smooth oxide layer (TaC_xO_y) with a large number of parallel self-healed cracks formed on the sample surface. Even the dense oxide layer has been formed, the oxidation process is controlled by surface kinetics of oxygen diffusion in the initial stage of 0–10 min. After oxidation for 10 min, the oxidation process is controlled by the diffusion of the oxygen in TaC_xO_y layer.

In particular, composites show anisotropic oxidation behavior due to the existence of reinforcement fibers. Carbon fibers are vulnerable when exposed to oxidation environment and can be oxidized violently. When the oxidation takes place along the fiber layer, the fibers are consumed and left the holes as oxygen diffusion

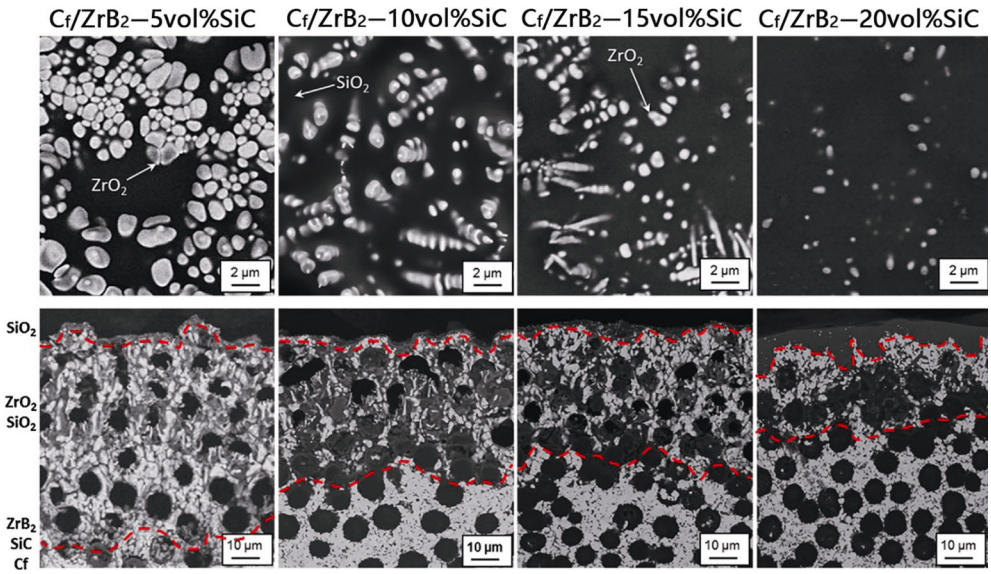

Fig. 25 Microstructure of the surface (top) and cross section (bottom) of C_f/ZrB_2–SiC with different SiC contents after oxidation at 1650 ℃. Reproduced with permission from Ref. [216], © Elsevier Ltd. 2018.

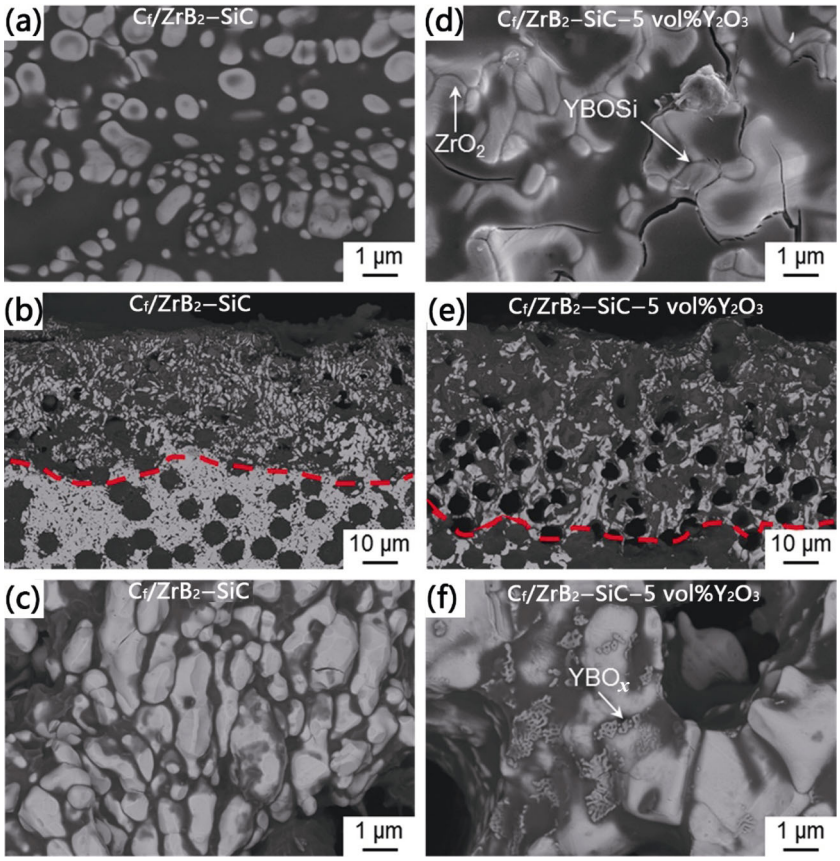

Fig. 26 Microstructures of C_f/ZrB_2–SiC and C_f/ZrB_2–SiC–5 vol%Y_2O_3 composites after oxidation at 1650 ℃ in air: surface morphology (a, d), cross-sections of the oxide layer (b, e), and detail of the oxide layer (c, f). Reproduced with permission from Ref. [276], © Elsevier Ltd. 2020.

channel which is negative to oxidation resistance. When the oxidation direction is perpendicular to the fibers layer, the fibers are oxidized fast and the ceramic matrix will be exposed. The ceramic matrix will be oxidized to denser oxide layer and resist the further oxidation [216].

(2) Ablation behavior and mechanisms of UHTCMCs

Partially due to temperature restriction of furnace, oxidation test mainly processed at a temperature below 2000 ℃. However, UHTCMCs are generally designed for applications at above 2000 ℃, which also need to withstand the vast scouring of corrosive/oxidative air. Therefore, more work is focused on the ablation behavior and mechanisms of UHTCMCs, which is closer to their service environments. The ablation test methods, such as oxyacetylene flame, oxypropane flame, plasma flame, arc jet, and wind tunnel, etc., are developed to simulate the service environments of UHTCMCs. Oxyacetylene and oxypropane tests are the most common and cheapest methods which provide similar temperature and heat flux conditions. However, the gas velocity is relatively slow. More researchers tend to use plasma flame test as it can provide more serious ablation conditions. In particular, arc jet and wind tunnel are the best methods to simulate the service environment of the UHTCMCs. However, these two techniques are quite expensive, which restrict their wide applications [257,279–282].

UHTCMCs show good ablation resistance and their ablation mechanisms are widely studied. Generally, the ablation resistance of UHTCMCs is realized by forming oxide layer with a high melting point [283–286]. Glassy phase is also needed to fill up the cracks and pores to form a dense oxide layer, which can prevent the inward diffusion of the oxygen. For the matrix with boride UHTCs, B_2O_3 evaporates violently during high-temperature ablation and cannot directly protect composites by forming borosilicate, due to the higher ablation temperature and the vast scouring of ablation flame. Some B_2O_3 may exist in the oxide scale due to the incomplete evaporation or the continued production of the B_2O_3 beneath the outer scale. It

should be noted that the evaporation of B_2O_3 can dissipate heat accumulation and alleviated the damage to the composites induced by heat flux [282].

SiC addition can improve the ablation resistance at medium and high temperature by forming a glassy SiO_2 phase. However, ablation resistance of the composites at ultra-high temperature will be degraded if the SiC volume fraction in the matrix is too high, where the glassy SiO_2 phase cannot exist stably under ultra-high temperature combustion gas scouring [287]. High melting point oxides from the UHTCs matrix are the key anti-ablative components for the ablation resistance of UHTCMCs at ultra-high temperature extreme conditions. The as-formed solid skeleton of oxides with a high melting point supports and retains the glassy SiO_2 phase. Taking C_f/ZrB_2–SiC composites as an example, high melting point oxide grains (ZrO_2 grains) are precipitated from the glassy SiO_2 phase, coarsened, and sintered via a quasi-liquid phase assisted route. The phase transition of ZrO_2 induces the formation of cracks in the oxide layer and decreases the ablation resistance of composites with the increase of ablation temperature (Fig. 27) [198].

The addition of rare earth elements, such as LaB_6, La_2O_3, and Y_2O_3, to ZrB_2 matrix has been studied and expected to stabilize the ZrO_2 and reduces the evaporation of the glass phase. High melting point (~2300 ℃) $La_2Zr_2O_7$ is expected to form. However, $La_2Zr_2O_7$ has not been detected after ablation at ~2500 ℃. Moreover, the addition of La^{3+} with lower valence cation to ZrB_2 increases the oxygen diffusion coefficient in the ZrO_2 oxide layer and lowers the eutectic temperature of the oxide scale. As a result, the oxidation of the composites with La addition is accelerated during ablation [288]. Luo *et al.* [218] added Y_2O_3 into the C_f/SiC–ZrC composites and tested the ablation properties by oxyacetylene torch under the heat flux of 4.2 $MW \cdot m^{-2}$. Due to the high ablation temperature (~3000 ℃), the glassy silica phase evaporates quickly during ablation and the Y_2O_3 and ZrO_2 are left in the oxide layer. The reaction between SiO_2 and Y_2O_3 may need long time or excessive silica. As a result, no trace of any reaction between Y_2O_3 and silica has been detected. Y_2O_3 neither reacted with ZrO_2 nor the phase transformation during the cooling stage suppressed. The vast evaporation of SiO_2 and the porous ZrO_2 leads to the exposure and further ablation of the underneath composites.

Zeng *et al.* [219] added TiC into the C_f/C–SiC–ZrC composites and compared the ablation properties with C_f/C–SiC and C_f/C–TiC. During ablation test at 2500 ℃, $Zr_{1-x}Ti_xO_2$ with high viscosity and low volatility is formed. With the evaporation of glassy SiO_2, the Ti-rich oxides can precipitate from the glassy SiO_2 and rebuild the protective scale with lower volatility against the erosion by the ultra-high temperature. Besides, the precipitation of Zr-rich oxides can further improve the viscosity of the oxide layer to withstand the flushing by ablation flame. As a result, the C_f/C–SiC–ZrC–TiC composites show a better ablation resistance than C_f/C–SiC and C_f/C–TiC.

Generally, Hf-based UHTCMCs present better ablation resistance than Zr-based composites as the HfO_2 has a higher melting point than ZrO_2. And HfB_2 shows better anti-ablation properties than HfC as the oxidation products are adherent to the composites (Fig. 28) [287,288]. Compared with Zr-based and Hf-based composites, the composites with TaC matrix show poor ablation resistance as the formed Ta_2O_5 has a low melting point of 1872 ℃, which results in the intense

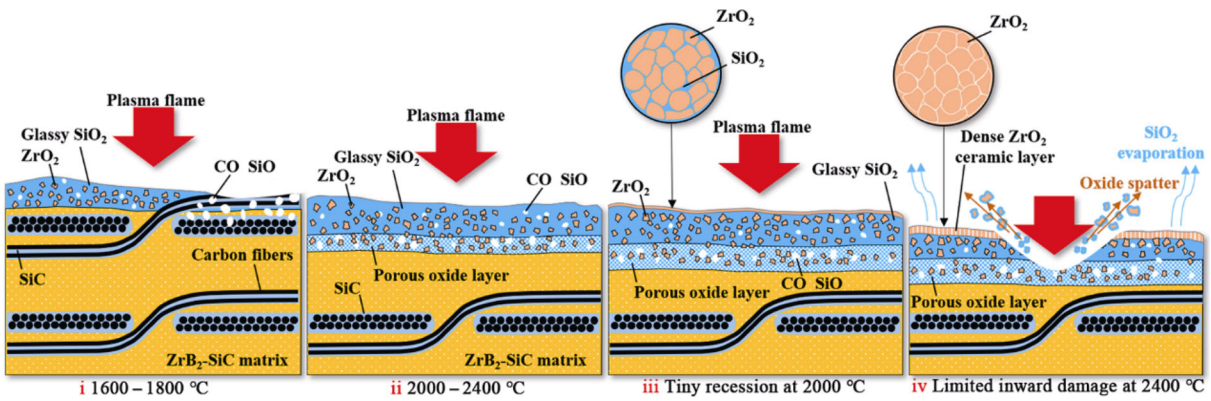

Fig. 27 Schematic diagram of the ablation mechanisms for 2D-C_f/ZrB_2–SiC composites at temperatures from 1600 to 2400 ℃. Reproduced with permission from Ref. [198], © Elsevier Ltd. 2020.

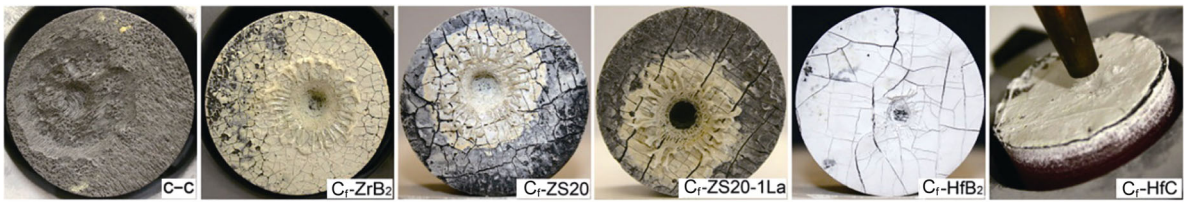

Fig. 28 Optical images of C/C and C_f/UHTCs composites after 60-s oxyacetylene torch test. Reproduced with permission from Ref. [288], © Elsevier Ltd. 2013.

mechanical denudation at temperatures above 2000 ℃ [195,215,287].

In addition to the composition, thermal properties also affect the ablation properties of the composites significantly. Chen *et al.* [239] compared the ablation behaviors of RMI-C_f/ZrC–SiC and PIP-C_f/ZrC–SiC composites with similar compositions. The results revealed that RMI-C_f/ZrC–SiC composites with higher thermal conductivity are more capable to transmit heat timely and reduce the ablation surface temperature effectively (Fig. 29(a)). As a result, the RMI-C_f/ZrC–SiC composites experience less heat damage and show a better ablation resistance (Figs. 29(b)–29(d)). Generally, heat is conducted mainly by phonon motion of the solid framework (crystal lattice vibration) in the composites. Phonons will be scattered at pores, grain boundaries, and phase boundaries, which result in the low thermal conductivity of the composites. Therefore, reducing porosity and establishing a dense continuous phase distribution are effective ways to increase the thermal conductivity for a better ablation resistance. Besides, carbon fibers are vulnerable during ablation and prefer to be oxidized to form oxygen diffusion channels [284]. Therefore, ablation resistance can be improved by optimizing the structure of fiber preform [198] or developing UHTC_f/UHTC composites [289,290].

4 UHTC coatings: Processing, microstructure, and performance

4. 1 Composition and microstructure design of UHTC coatings

In addition to bulk ceramics and composites, coating is another important application form of UHTCs. The

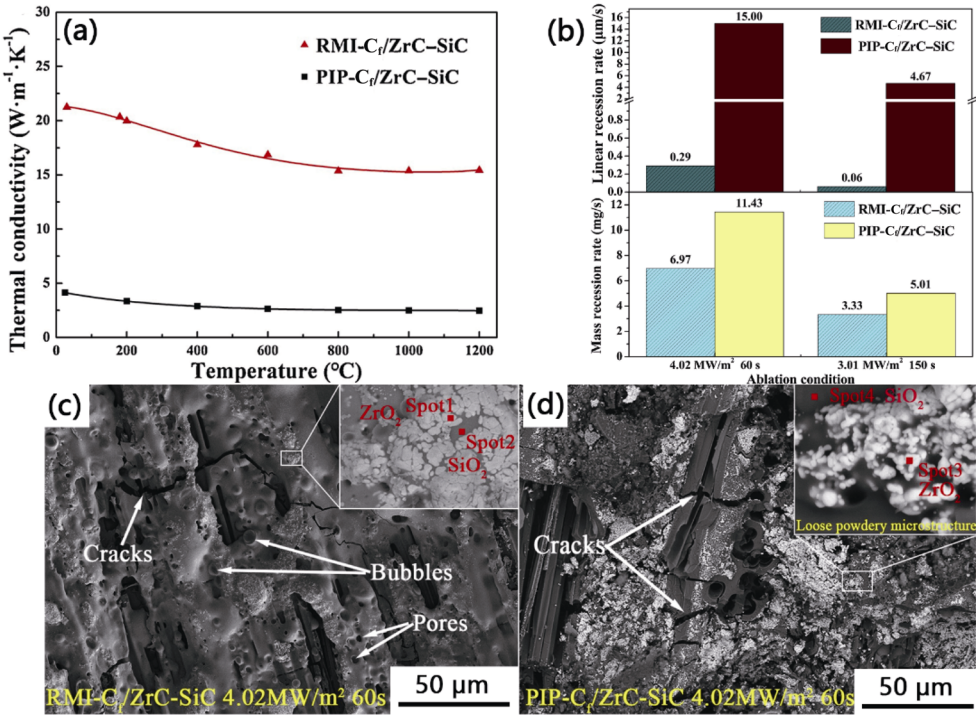

Fig. 29 Thermal conductivity of RMI-C_f/ZrC–SiC and PIP-C_f/ZrC–SiC composites (a), ablation recession rates (b), and the ablated surface microstructure of RMI-C_f/ZrC–SiC (c), and PIP-C_f/ZrC–SiC composites (d). Reproduced with permission from Ref. [239], © Elsevier Ltd. 2019.

UHTC coatings are designed to protect the substrates from the oxidation/ablation environments at ultra-high temperatures. The composition design rules of UHTC protective coatings are listed as below:

1) Chemical compatibility with the substrate, i.e., any detrimental reaction between the coating and substrate should be prevented.

2) Thermo-physical compatibility, which mainly related to a good match of thermal expansion coefficient (CTE).

3) Low oxygen permeability to prevent the inward diffusion of oxidized species.

4) Low volatility to prevent excessive ablation in high pressure/velocity gas streams.

Figure 30 summarizes possible compositions, processing, microstructures, and applications of the UHTC coatings. Each UHTC has its ideal working temperatures, and usually combines with silicides (SiC, $MoSi_2$, etc.). The addition of UHTC into silicides can overcome the deficiency of the traditional Si-based ceramic coatings, i.e., SiC easily takes place active oxidation at low oxygen partial pressures or temperatures higher than 1700 ℃ [5,291–293]. Various methods including pack cementation (PC) [292,294–299], CVD [300–311], plasma spray (PS) [293,312–316], slurry-sintering (SS) [317,318], and hot pressing (HP) [52,319,320] have been developed to prepare UHTC coatings. The selection of the UHTC coatings highly depends on the requirements of the target applications (aero-thermo-chemical demands) and the feasibilities of their processing routes (cost and specific shaping availability). With respect to the published reports, the microstructures of the UHTC coatings can be mainly divided into three types, that is, single-phase, multiphase, single-phase multilayer, and multiphase multilayer, as shown in Fig. 30. In addition to the above-mentioned design rules of UHTC coatings, the coating structure design should also consider the interfacial compatibility design, multi-phase synergistic protection, multi-scale toughening, and multi-processing route combination. Due to their high melting point, good oxidation performance, and ablation resistance, UHTC coatings can work under harsh aerospace environments, such as turbines and blades for aero engines, nozzles for rocket engines, and thermal protection systems (TPS) for hypersonic vehicles. The next section will introduce the different fabrication methods of the UHTC coatings and their feasibilities in detail, and then discuss the design purpose of different UHTC coating structures and their performances.

Microstructural designs of gradient and multilayer UHTC coating structure are adopted to realize the good interfacial compatibility. A well compatible coating with the substrate is commonly used as the inner layer to avoid spallation or even stress-induced cracking. Multi-phase synergistic protection means UHTC is used

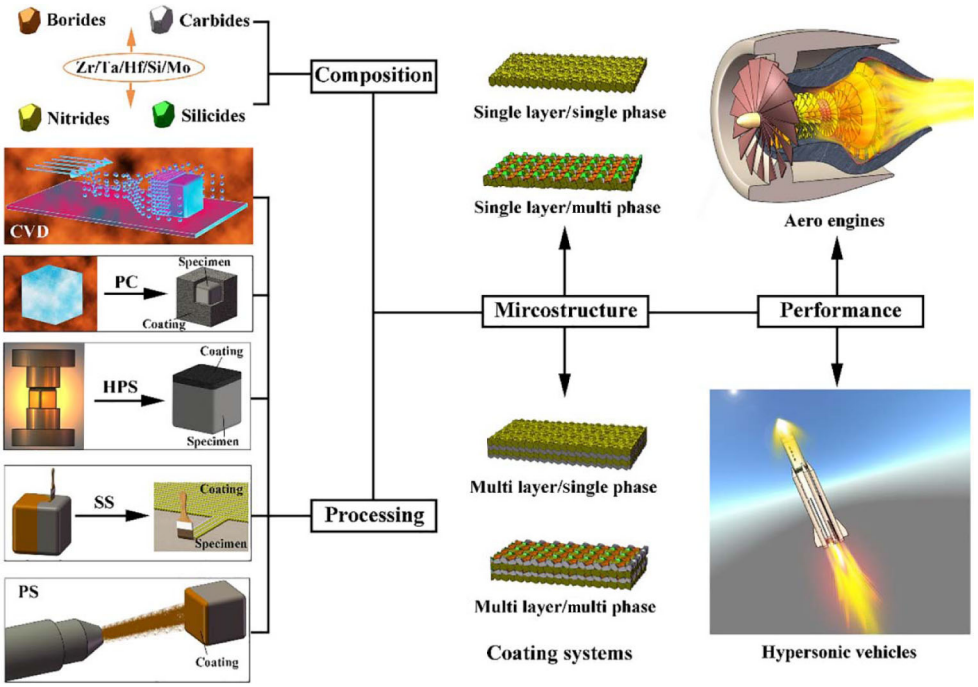

Fig. 30 Schematic diagram of the composition, processing, microstructure, and application of the UHTC coatings.

together with other materials. Multi-scale synergistic toughening is aimed to solve the intrinsic brittleness and low damage tolerance of the UHTC, where toughened phases are introduced. Multi-processing route is mainly targeted to enhance the coating/substrate interface bonding and eliminate the coating defects. Flexibly comprehensive use of these design rules is the key to ensure that the UHTC coatings possess desirable properties. Section 4.2 will introduce the different fabrication methods of the UHTC coatings and their feasibilities in detail, and then discuss the design purpose of different UHTC coating structures and their performances.

4. 2 Processing routes of UHTC coatings

Processing routes determine whether the tailored compositions and structures of the UHTC coatings could be achieved. For each method, its microstructure control, cost, and performance will be discussed as follows with its advantages/disadvantages.

(1) Pack cementation (PC)

PC is a relatively simple technique that consists of immersing the substrate in a powder mixture of coating materials. During heat-treatment at a high temperature, the molten pack materials will infiltrate into or react with the substrate to form the UHTC coatings. The temperature must be sufficiently high to ensure the diffusion will take place. The desired UHTC coatings are usually obtained by the reactions of the raw coating materials themselves. The main disadvantage of PC is that if the fabrication condition is not strictly controlled, performance degradation of the substrate will inevitably occur due to the high treatment temperature. Additionally, the coating thickness is difficult to control.

(2) Chemical vapor deposition (CVD)

CVD is a deposition method used to produce high-quality, high-performance solid materials. The process mainly consists of the dissociation and/or chemical reactions of gaseous reactants and the deposition of a stable solid product. Its main advantage is the low preparation temperature, at which the substrate can avoid being damaged or forming defects. Microstructures of the UHTC coatings can be tailored by changing temperature, pressure, and precursor injection rate. If the deposition process is controlled well, the deposited solid product can show a dense, fine-grained structure free from impurities. Another advantage is that, by adjusting the injection of precursors, both single phase and multiple composition coatings can be obtained. However, CVD is a slow process, which makes the product expensive. Another shortcoming is that it must be performed under a vacuum or protective atmosphere. CVD UHTC coatings are usually accompanied by the exhaust of unreacted precursor gases and the production of chemical byproducts (e.g., HCl and HF) [303,304,307,308], and therefore, requirements for equipment are relatively strict.

(3) Plasma spray (PS)

PS is a simple way to prepare coatings of refractories with high melting points. Diverse materials, such as metal and ceramics, can be applied as spray materials. During coating preparation, UHTC powders are injected into a very high temperature plasma flame, where they are rapidly heated and accelerated to a high velocity. The hot UHTC powders are injected to the substrate and rapidly cooled, forming a coating. However, various drawbacks, such as high porosity, poor bonding strength, high surface roughness, and lamellar stacking characteristics, could also occur. As a result, subsequent processing is usually required to eliminate the above defects [321].

(4) Slurry-sintering (SS)

SS is the most widely exploited coating technique in various fields. The slurry made of particles or organic precursor dispersed in a suitable solvent is brushed onto the substrate, then dried and finally heat-treated in an inert gas atmosphere. The solvent is usually removed in the drying stage. To achieve a high densification level of the UHTC coating, several brushing–dry–heat treatment cycles must be performed. Due to the limitation by the weak bonding of coating/substrate, this method is not used individually but is usually combined with other methods such as liquid and gas infiltration of Si [298,322–327].

(5) Hot pressing (HP)

Like other ceramics, restricted by their covalent bond and intrinsic brittleness, UHTC particles are difficult to be sintered [52,137]. Sinter-additives, which could transform into liquid phases and promote the solid-state reactions, are beneficial for the UHTC coating densification. When coatings are subjected to harsh service environments, since the metallic and intermetallic sinter additives can be easily softened and melt, they are generally not considered as sintering additives for UHTC coatings, whereas the Si-based ceramics such as SiC, $MoSi_2$, and $TaSi_2$ are frequently used [52,137,319,328–330]. Although sintering aids

could modify the sintering conditions, UHTC coating with a high densification level is not guaranteed, without the assistance of external pressure. HPS allows for versatile structure design; however, it is not applicative to the fabrication of UHTC coatings on the complex-shaped components.

4. 3 Microstructure and anti-oxidation/ablation properties of the UHTC coatings

The UHTCs are typically made of the carbide, nitride, and boride of the transition metals, among which Group IVB (Ti, Zr, Hf) carbides and borides together with TaC are usually used as the coating materials [292,294–297,302–304,311–313,320,325,331–339] due to the *in-situ* formed oxygen barrier layer, namely UHTC–oxides. The rational selection of the coating materials, the optimal design of the structure, and the accessible processing route are the key steps to obtain the UHTC coatings with good performances. As shown in Fig. 30, UHTC coatings are mainly divided into three types, that is, single-phase, multiphase, and multilayer (single-phase multilayer and multiphase multilayer) coatings. Recent progresses on these three types of coatings are discussed below.

(1) Single-phase UHTC coatings

Figure 31 shows the typical morphologies of the single-phase UHTC coatings. Among the coating fabrication methods, CVD and PS are the two most frequently adopted. UltraMet has prepared a series of CVD UHTC coatings [340], including HfC, ZrC, HfB_2, and ZrB_2 coatings. Domestic studies in this field have also been achieved. Zhang *et al.* [309] and Wang *et al.* [307] deposited HfC coatings on C/C composites by low-pressure chemical vapor deposition (LPCVD) using the $HfCl_4$–CH_4–H_2–Ar system (Fig. 31(a)). It is reported that a moderate HfC coating thickness (~40 μm) on C/C substrate could effectively release the thermal stress generated during the ablation [309] (Fig. 31(b)), which exhibited excellent ablation resistant performance after ablation for 60 s under the oxyacetylene flame. The mass and linear ablation rates were only 0.13 $mg \cdot s^{-1}$ and 0.09 $\mu m \cdot s^{-1}$, respectively.

Similar to the CVD–HfC coating, Zhu *et al.* [310] designed a dense cauliflower-shaped ZrB_2 coating by LPCVD based on the $ZrCl_4$–BCl_3–H_2–Ar system, and the corresponding deposition mechanism was discussed in detail. It was reported that the temperature and H_2 and BCl_3 fluxes significantly affect surface roughness, growth rate, and phase composition of the ZrB_2 coating. In addition to CVD, PS was also used to prepare HfC [316], ZrC [312,337] (Figs. 31(c) and 31(d)) and ZrB_2 [315] coatings. The oxidation/ablation properties of the single-phase UHTC coatings mainly depend on the oxidation products formed. The integrity of the formed oxidation scale on the coating surface is crucial for its service reliability. However, each UHTC has its

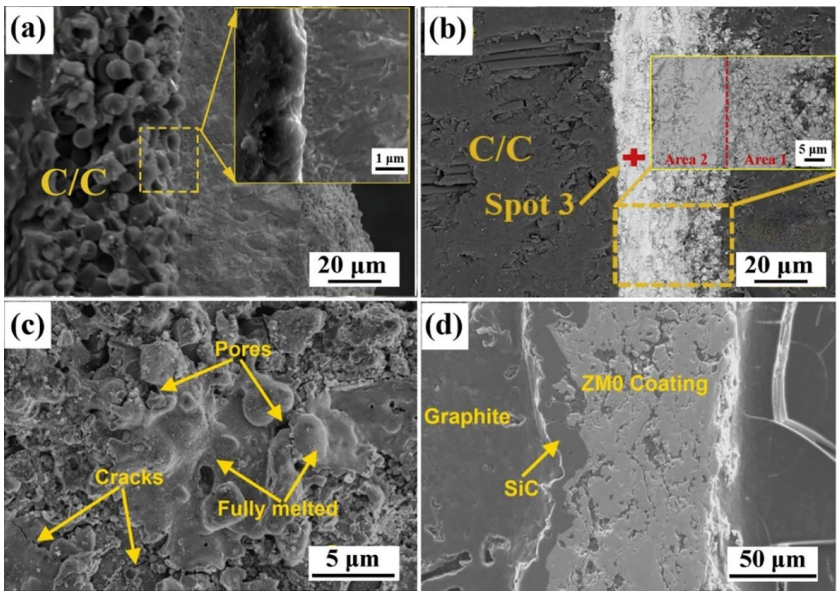

Fig. 31 Typical morphologies of the single UHTC coatings: cross-section of the CVD–HfC coating before ablation (a); cross-section of the CVD–HfC coating after ablation (b). Reproduced with permission from Ref. [309] , © Elsevier Ltd. 2020. Surface and cross-section of PS–ZrC coating (c, d). Reproduced with permission from Ref. [312], © Elsevier Ltd and Techna Group S.r.l. 2018.

working temperature range. Taking carbides for example, the ZrO_2 layer on the ZrC coating after oxidation usually presents loose structure due to the absence of self-sealed phases, and oxygen could easily pass through the channels by gaseous diffusion. Meanwhile, the thermal expansion mismatch between the oxidation layer and un-oxidized coating contributed to the occurrence of cracks during high-low temperature cycles. Compared with carbides, borides with ZrB_2 as an example, provide better protection below 1200 ℃ due to the formation of ZrO_2 containing a molten layer of boron oxide [5,295,296,331,332,341]. The liquid phase B_2O_3 could fill the cracks and holes. However, as the temperature further increases, vast volatilization of B_2O_3 degrades its performance.

(2) Multiphase UHTC coatings

The flight process of hypersonic vehicles requires a TPS with high resistance to oxidation/ablation. As discussed in the previous Section 3.4, the oxidation/ ablation resistant performances of single-phase UHTC coatings depend highly on the properties of the formed oxidation products that cover the surface, including the composition and the structure of the oxidized surface. According to the design rule of multi-phase synergistic protection, the integration of the different components could mitigate the limits of each single component. As a result, multiphase UHTC coatings were proposed. Table 5 summarizes the reported works of multiphase UHTC coatings, which can be mainly divided into two types, namely UHTC–silicide and multiphase UHTC. For UHTC–silicide coatings, Richet *et al.* [317] prepared a HfB_2–SiC coating and investigated its oxidation resistance. The results showed that the HfO_2 phase embedded borosilicate glass led to slower diffusion of oxygen at high temperatures. Lee *et al.* [311] utilized methyltrichlorosilane (MTS) and $ZrCl_4$ powder respectively as the precursors of SiC and ZrC to prepare a ZrC–SiC coating by CVD. Zhang *et al.* [297] successfully coated C/C composites with HfC–SiC, ZrB_2–SiC coatings by PC [296,299] (Fig. 32(a)). During ablation, the formed Zr–O–Si multiphase glass layer showed good thermal stability at high temperatures, thereby benefiting for withstanding the denudation of the combustion gas [296]. Zhang *et al.* [320] proposed SPS to prepare the HfB_2–SiC–$TaSi_2$ coating on graphite (Fig. 32(b)). It was reported that during oxidation at 1700 ℃, the $TaSi_2$ could inhibit the active oxidation of SiC, and its oxidation volume expansion could reduce the loosening effect of HfB_2. HfB_2–SiC–$MoSi_2$ coating was fabricated by Wang *et al.* [342]. After oxidation at 1500 ℃ for 408 h, the coating surface was oxidized to form a self-sealing silicate glass layer containing HfO_2 and $HfSiO_4$, which could hinder the crack propagation. In general, compared with the single-phase UHTC coatings, the good oxidation/ablation performances of the UHTC–silicide coatings are attributed to the synergistic effects of the different compositions, especially for the formation of the immiscible, multicomponent glass surface layers [292,294–296,303,312,317,320,322,323,325,330,347].

Table 5 Preparation methods and properties of various multiphase UHTC coatings

Coating	Preparation method	Test	Property	Ref.
ZrB_2–SiC–ZrC	PS+PC	Oxyacetylene, heat flux: 2.4 MW·m^{-2}, ablation 120 s	–0.16 mg·s^{-1}; 1.30 μm·s^{-1}	[321]
$MoSi_2$–$TaSi_2$	SS+PC	1700 ℃, oxidation 12 h	Without failure	[343]
HfB_2–SiC–Si	SS+gas infiltration Si	1500 ℃, oxidation 538 h	Mass loss 0.69%	[326]
HfB_2–SiC–$TaSi_2$	SPS	—	—	[320]
$Hf_{0.5}Ta_{0.5}B_2$–SiC–Si	SS+gas infiltration Si	900 ℃, oxidation 1320 h	Mass gain 0.14%	[325]
HfC–TaC	CVD	Oxyacetylene, heat flux: 2.4 MW·m^{-2}, ablation 120 s	0.97 mg·s^{-1} 1.32 μm·s^{-1}	[303]
HfC–ZrC	CVD	Oxyacetylene, heat flux: 2.4 MW·m^{-2}, ablation 120 s	0.63 mg·s^{-1} 0.21 μm·s^{-1}	[303]
TaB_2–SiC–Si	SS+gas infiltration Si	1550 ℃, oxidation 168 h	Mass gain 2.06%	[325]
ZrB_2–SiC	PS	—	—	[344]
ZrC–SiC	Thermal evaporation	3000 ℃, ablation 200 s	–0.46±0.15 mg·cm^{-2}·s^{-1} –1.00±0.04 μm·s^{-1}	[345]
Ta–Hf–C solid solution coating	PS	Oxyacetylene, heat flux: 4.18 MW·m^{-2}, ablation 30 s	–0.58 mg·s^{-1} –0.94 μm·s^{-1}	[346]
ZrC–SiC	CVD	—	—	[311]
HfB_2–SiC–$MoSi_2$	PC	1550 ℃, oxidation 408 h	Mass loss 0.76%	[342]

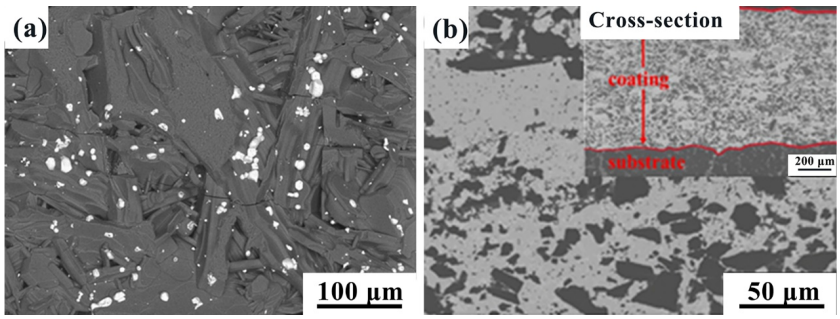

Fig. 32 Typical morphologies of the UHTC–silicide coatings: PC–ZrB_2–SiC coating [296] (a) and SPS–HfB_2–SiC–$TaSi_2$ coating [320] (b). Reproduced with permission from Ref. [296], © Elsevier Ltd. 2018; Ref. [320], © Elsevier Ltd. 2020.

The design of silicates modified UHTC coatings [291,296–298,304,317,320,324,326] is to enhance their long-term oxidation resistances, while multiphase UHTC coatings [303,307,308,327] are mainly to promote the ablation performances. Cui *et al.* [334] fabricated ZrB_2–ZrC composite coating on TC4 titanium alloy by PS. The atomic radii of Hf, Zr, and Ta are close, enabling the formation of solid solutions between each other at high temperatures. With these considerations, Li *et al.* [302,308] prepared a Hf(Ta)C coating by CVD based on the $HfCl_4$–$TaCl_5$–CH_4–H_2–Ar system. Ren *et al.* [303] have attempted to prepare HfC–ZrC coating by CVD using $HfCl_4$–$ZrCl_4$–CH_4–H_2–Ar system. Compared with the HfC coating, the HfC–ZrC coating exhibited better ablation performance due to the solid solution sintering between the HfO_2 and ZrO_2, and the formation of the dense protective oxide layer. After ablation for 120 s, the linear and mass ablation rates of the HfC–ZrC-coated C/C sample were only 0.21 $\mu m \cdot s^{-1}$ and 0.63 $mg \cdot s^{-1}$, respectively. The linear and mass ablation rates of HfC-coated C/C sample under the same condition were 1.48 $\mu m \cdot s^{-1}$ and 1.21 $mg \cdot s^{-1}$, respectively. In addition, compared to monolithic UHTC coatings, the addition of rare earth compounds was also reported to improve their oxidation performances [4,291,314,329,331]. For example, Sm dopant was proved to be a beneficial additive to ZrB_2–SiC coating, which could stabilize the tetragonal ZrO_2 phase at high temperatures [314,331].

(3) Multilayer UHTC coatings

Although the design of multiphase UHTC coatings is beneficial for eliminating the coating defects, it remains difficulty to obtain a UHTC coating with a dense structure. During the preparation, the cooling, or even the thermal shock cycle, the CTE mismatch between the UHTC coating and the substrate (C/C [296–298], C/SiC [317,336,348], or graphite [295,325]) will inevitably lead to the formation of pores and cracks, thereby influencing their oxidation/ablation resistances. According to the design rule of interfacial compatibility, multilayer structure could offer the UHTC coatings with multifunctional characteristics: lower residual stress, good adherence to the substrate, and improved hardness/toughness ratio. Different coating concepts can be combined in a multilayer structure and be tailored for specific application demands. Since the UHTC coatings are designed to serve at high temperatures and extreme environment, the multilayer structure design is mainly to alleviate the coating/substrate CTE mismatch, thereby enhancing its service reliability. As a result, a variety of researches are focused on the dense multilayer UHTC coatings accompanied by functionally gradient structures. Table 6 shows part of the reported multilayer UHTC coatings. It is summarized that the multilayer UHTC coatings can mainly be divided into two categories: single-phase UHTC/silicide coatings and multiphase UHTC/silicide coatings. Among the silicides, SiC is the most adopted bonding or transition layer between the substrates and the UHTC coatings, due to its good physical and chemical compatibility with the substrate. These two types of multilayer UHTC coatings are discussed respectively as follows.

(4) Single-phase UHTC/silicide multilayer coating

Taking advantage of the precise control of the CVD reaction precursor, HfC/SiC multilayers coated graphite, fiber, and C/C were prepared by Allemand *et al* [300] and Verdon *et al.* [305] (Fig. 33(a)) and Wang *et al.* [306]. The coating consists of 5–10 alternated layers of SiC and HfC with a total thickness of 20 or 40 μm [300]. C/C composites with SiC/TaC multilayer coated carbon fibers were prepared by Chen *et al.* [301]. In addition to carbide/silicide multilayer coatings, boride/silicide multilayer coatings have also been developed.

Table 6 Selected reports of various multilayer UHTC coatings

Coating	Preparation method	Test	Property	Ref.
SiC/ZrB_2	PC+PS	Oxyacetylene, 3000 ℃; ablation 120 s	4.8×10^{-4} g·cm^{-2}·s^{-1}	[313]
ZrB_2–SiC/SiC	PC+PS	Arc-heated wind tunnel 2200 ℃, 1000 s	-1.9×10^{-2} mg·cm^{-2}·s^{-1} 2.9×10^{-5} mm·s^{-1}	[349]
HfC/SiC HfC/TiC/SiC	PS	—	—	[333]
SiC/ZrB_2–SiC/SiC	SS+CVD	1100 ℃, 114 h; 1300 ℃, 114 h; 1500 ℃ for 68 h	Mass loss of 0.36, 1.65, and 3.45 mg·cm^{-2}	[336]
$WSi_2/ZrSi_2/Zr_xHf_{1-x}C$/SiC	Thermal evaporation	Oxyacetylene, 2600 ℃, 300 s	–0.122 mg·s^{-1}	[339]
HfC/SiC	CVD	—	—	[305]

$SiC/ZrB_2(HfB_2)$ multilayer coating was developed by Loehman and Corral [350] to compensate boron loss at high temperatures. Hu *et al.* [335] obtained a $ZrB_2/MoSi_2$ multilayer coating on the SiC coated C/C composite by PS (Fig. 33(b)). It was reported that the alternate design resulted in laminated stress distribution and then improved the ablation resistance of the coating. After ablation at a heat flux of 2.4 MW·m^{-2} for 30 s, its linear growth rate and mass gain rate were 1.67 μm·s^{-1} and 0.44 mg·s^{-1}, respectively.

Strong interfacial adhesion with the substrate and good resistance to the crack caused by the coating/substrate CTE mismatch are two general requirements for coating structure designs. Based on the design rule of multi-processing routes, two or more processing routes are often used synergistically to satisfy these demands. PC combined with PS or CVD is the most common method. Wang *et al.* [338] evaluated the ablation properties of TaC/SiC coating deposited on C/C by PC and PS (Fig. 33(c)). It was reported that at 2100 ℃, the oxides formed on the coating surface were easily blown away by the flame; however, as the ablation temperature decreased to 1900 and 1800 ℃, the coating exhibited excellent ablation performance.

(5) Multiphase UHTC/silicide multilayer coatings

Boron loss of the borides at high temperatures and the "pesting" oxidation of carbides, to a certain extent, limit the application of the single-phase UHTC/silicide multilayer coatings. The advantage of multiphase UHTC/silicide over single-phase UHTC/silicide coatings is that they can overcome the problems encountered by the single-phase UHTC and better exploit the synergetic oxidation/ablation effects of multiple components. The main processing routes for multiphase UHTC/silicide coatings can be classified into PC [292,295,298], PC+PS [293,313,327], and SS with liquid/gas infiltrated Si or CVD–SiC [298,322–326,348].

Zhang *et al.* [293] investigated the ablation performance of SiC/ZrB_2–SiC–ZrC multilayer coating for C/C composites prepared by PC+PS (Fig. 34(a)). After ablation for 120 s, the coating exhibited a three-layered structure consisting of a porous ZrO_2 layer, a ZrO_2–SiO_2 thin layer, and a SiC-depleted layer. The oxidation layers can act as a thermal barrier and inhibit the inward diffusion of oxygen. In addition to PC+PS, Xiang *et al.* [348] proposed SS combined with CVD to develop a $ZrC(ZrB_2)$–SiC/SiC coating on the C/SiC composites. In this process, ZrC (ZrB_2) powders with polycarbosilane-xylene were firstly pasted on the surface of C/SiC composites, and then CVD SiC was penetrated in the gaps of ZrC (ZrB_2) powders. Similarly, Hu *et al.* [336] investigated the oxidation resistance of SiC/ZrB_2–SiC/SiC coated C/SiC composites (Fig. 34(b)). Thanks to the synergistic protection effects

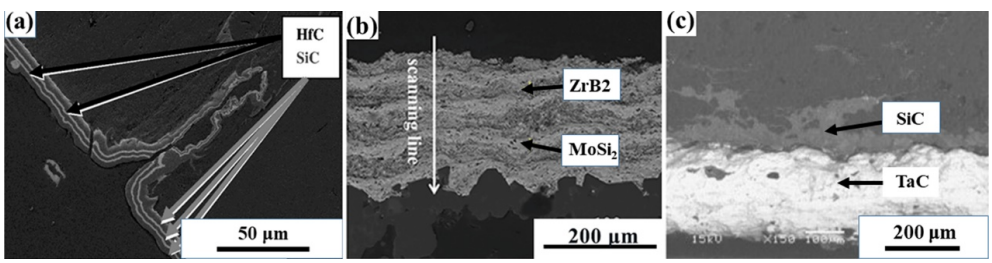

Fig. 33 Typical morphologies of the single UHTC/silicide multilayer coatings: CVD-HfC/SiC coated C/C [305] (a), PS–$ZrB_2/MoSi_2$ coated C/C [335] (b), and PC+PS TaC/SiC coated C/C [338] (c). Reproduced with permission from Ref. [305], © Elsevier B.V. 2013; Ref. [335], © Elsevier Ltd. 2020; Ref. [338], © Elsevier Ltd and Techna Group S.r.l. 2012.

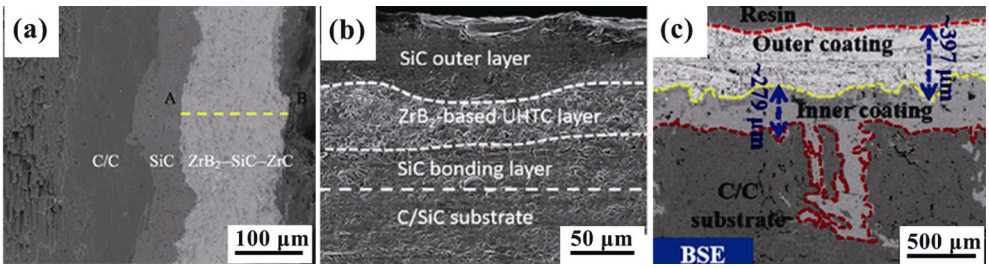

Fig. 34 Typical morphologies of multiphase UHTC/silicide multilayer coatings: SiC/ZrB_2–ZrC–SiC [293] (a), SiC/ZrB_2–SiC/SiC [336] (b), and HfB_2–$MoSi_2$/SiC–Si [324] (c). Reproduced with permission from Ref. [293], © Elsevier B.V. 2016; Ref. [336], © Elsevier Ltd. 2018; Ref. [324], © Elsevier B.V. 2020.

of the ZrB_2–SiC and SiC layers, after exposure to 1100 ℃ for 114 h, 1300 ℃ for 114 h, and 1500 ℃ for 68 h in air, the coated C/SiC only had a mass loss of 0.36, 1.65 and 3.45 mg·cm^{-2}, respectively. To further enhance the coating interfacial adhesion, SS combined with gas infiltration of Si were proposed by Zhou *et al.* [351], Zhou *et al.* [298], Zhang *et al.* [324], Jiang *et al.* [322], and Ren *et al.* [323]. For example, Zhang *et al.* [324] utilized this method to prepare HfB_2–$MoSi_2$/SiC–Si coating on the C/C composites (Fig. 34(c)). At 1700 ℃, the formed Hf–Si–O oxide scale showed good high-temperature stability and self-healing ability, which could protect the C/C substrate for 73 h.

As described above, the UHTC coatings play a crucial role in enhancing the oxidation/ablation performances of the underlying substrates. However, due to the intrinsic brittle fracture feature resulted from the strong covalent bonding nature of UHTC itself, when the UHTC coatings subjected to high–low temperature cycles or even harsh aero-thermal environment, they are prone to crack and debond [5,52,137,296,297,315,326,330–332]. To address this problem, according to the design rule of multi-scale synergistic toughening, researchers have proposed to introduce nanostructures (whiskers [352], nanowires [343,353], nanotubes [328], etc.) to toughen the UHTC coatings. The nanostructures mentioned above possess high strength/modulus and are often used in toughening the bulk ceramics [34,318,328,353], as described in Section 2. Among the nanostructures, ceramic whiskers and nanowires are mostly used. Wang and Luo [318] investigated the effect of SiC whiskers addition on the oxidation behavior of HfB_2–SiC–Si/SiC coating (Fig. 35(a)). The results showed that after oxidation for 468 h at 1500 ℃, the mass loss of the coating was decreased from 4.86% to 0.88%. Ren *et al.* [353] proposed HfC nanowires to toughen the ZrB_2–SiC/SiC coating. Due to the incorporation of HfC nanowires, hardness, elastic modulus, and fracture toughness of the coating were all improved. Cheng *et al.* [354] discovered that the existence of PyC layer played a positive role in stabilizing the structure and morphology of SiC nanowires at high temperatures (Figs. 35(b) and 35(c)). They utilized SiC/PyC core–shell nanowires to toughen the ZrB_2–SiC/SiC [327,332] and TaB_2–SiC coating [355] (Fig. 35(d)), which were proved beneficial for alleviating the thermal stress and increasing the coating toughness. In summary, proper processing route and careful microstructure tailor of the nanostructures reinforced UHTC coatings can enhance their crack propagation resistance effectively. The toughening mechanisms of the nanostructures can be mainly ascribed to the three aspects: 1) The nanostructured strengthening phase can induce the deflection of cracks at the crack tips, which can reduce the stress intensity factor and hinder the crack propagation. 2) The pulling out of the strengthening phase can produce new surfaces and consume more energy. 3) The strengthening phase can bridge the crack and resist the crack propagation.

4. 4 Oxidation/ablation mechanisms of the UHTC coatings

A substantial number of studies have described the oxidation and ablation mechanisms of the UHTC coatings [292–299,303,304,309,312–315,317,318,320, 322–326,330,332,333,335–339]. Oxidation/ablation performance manifests its resistance to the aggressive chemical environment that the UHTC coatings will encounter. However, the boron loss of the borides at high temperatures and the “pesting” oxidation of the carbides harm the service reliability of the single-phase UHTC coatings. According to the design rule of multi-phase synergistic protection, silicides are commonly

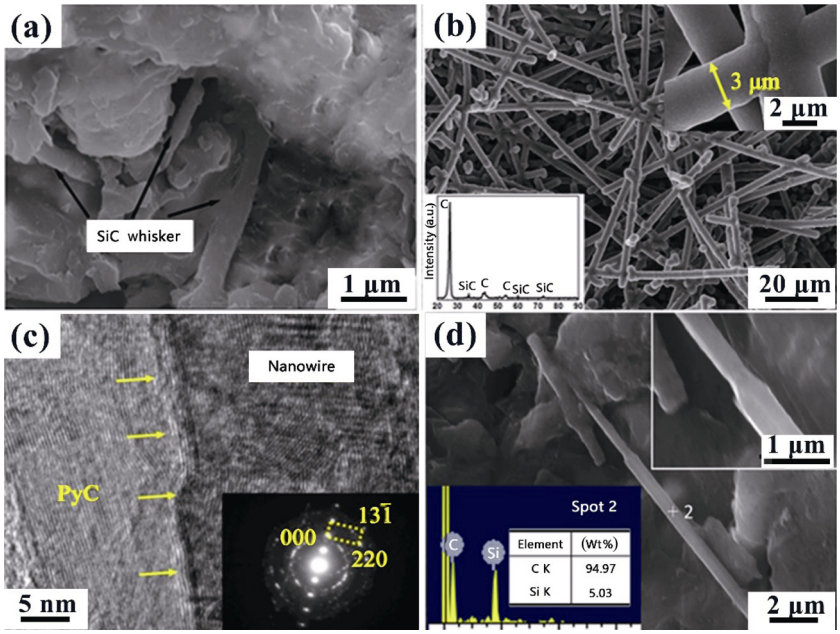

Fig. 35 Typical nanostructures used for UHTC coating toughening: SiC whiskers in the HfB_2–SiC–Si/SiC coating [318] (a), SiC/PyC core–shell nanowires [354] (b, c), and SiC/PyC core–shell nanowires in the TaB_2–SiC coating [355] (d). Reproduced with permission from Ref. [318], © Elsevier Ltd and Techna Group S.r.l. 2018; Ref. [354], © The American Ceramic Society 2018; Ref. [355], © Elsevier Ltd. 2018.

used to improve the oxidation resistance of the UHTC coatings in which SiC and $MoSi_2$ stand out [5,292, 293,295–297,299,305,306,314,315,317–320,322–324, 331,332,334,336,338,342,348,353]. The SiC and $MoSi_2$ improve the oxidation resistance of UHTC coatings via the formed silica-rich scales. The silica-rich scales show high fluidities and thus self-sealing behaviors that can reduce oxidation defects, making them ideal barriers for oxygen diffusion [291–293,295–297,299, 305,306,314,315,317,318,320,322–324,331,335,336,342]. The oxide layers could limit the oxygen inward diffusion and lower oxygen partial pressures for the inner coatings, so UHTC–silicide multiphase coatings could form different grades of oxide layer. Taking ZrB_2–SiC–ZrC coating as an example, ZrO_2–SiO_2 thin layer and a SiC-depleted layer are observed from the cross-section image of the ZrB_2–SiC–ZrC coating [293], as shown in Fig. 36. The external ZrO_2–SiO_2 glassy layer is effective in limiting the diffusion of oxygen into the inner coating. Beneath the ZrO_2–SiO_2 layer, the SiC-depleted layer is formed, due to the active oxidation of SiC under low oxygen partial pressure.

It is noted that borate and silicate glasses containing transition or rare earth metal oxides present strong tendency for phase separation due to immiscibility. The immiscibility could raise the liquidus temperature and increase the viscosity of the glass [356]. In this sense, Zr could be incorporated in the glasses network, which in turn helps to stabilize the O atoms in Si–O network (Fig. 37(a)). Based on the Stoke–Einstein relation, the high viscosity glass could also decrease the oxygen diffusion rate, which explains the good thermal stability of the Zr–Si–O glass layer [357]. Meanwhile, ZrO_2 can also be embedded in SiO_2 glass, and part ZrO_2 can react with SiO_2 to form $ZrSiO_4$. The pinning effect of $ZrSiO_4$ and ZrO_2 will resist the crack propagation of the Zr–Si–O glass layer during thermal shock and further improve the stability. The integrity of Zr–Si–O glass layer could in turn suppress the borate evaporation and the escape of gas by-products derived from the active oxidation of the inner coating. These are the main origins for the good oxidation resistance of ZrC–SiC, ZrB_2–SiC, or ZrB_2–ZrC–SiC coatings, which can also be observed in other UHTC–silicide multiphase coating systems such as Ta–Si–O glass layer for TaB_2–SiC coating [294] (Fig. 37(b)), synergistic effects of Hf–Si–O glass layer, $HfSiO_4$, and HfO_2 for HfC–SiC coating [304] (Fig. 37(c)), and synergistic effects of Hf–Ta–B–Si–O glass layer, $HfSiO_4$, and HfO_2 for HfB_2–SiC–$TaSi_2$ coating [320] (Fig. 37(d)).

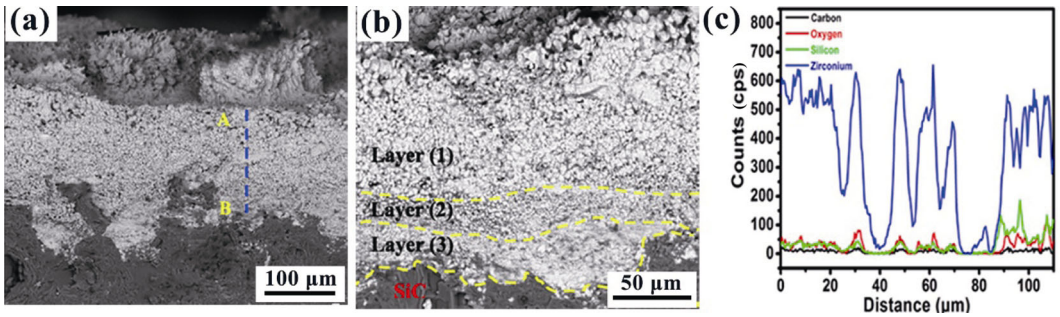

Fig. 36 Cross-section micrograph and element line analysis of the ZrB_2–SiC–ZrC coating after ablation. Reproduced with permission from Ref. [293], © Elsevier B.V. 2016.

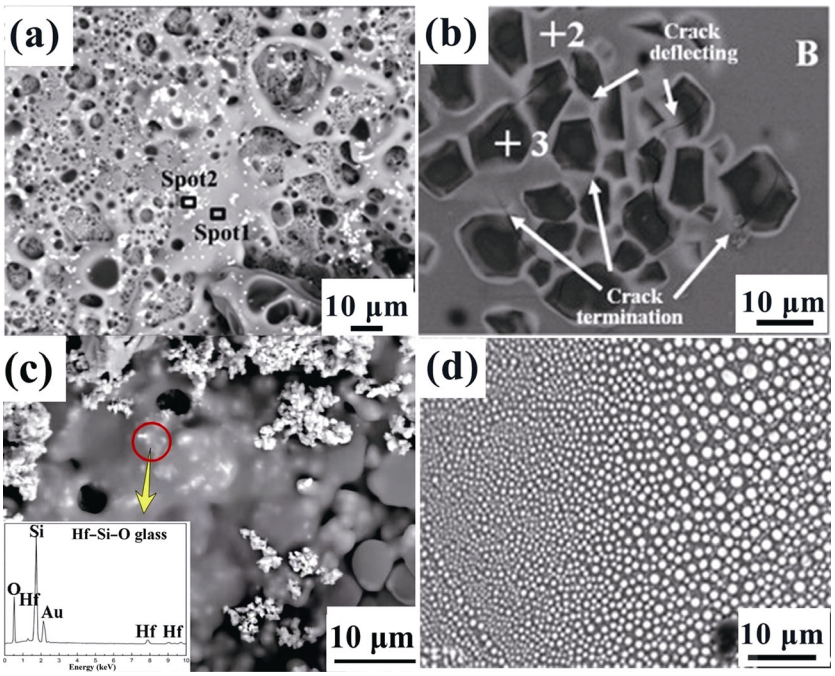

Fig. 37 Microstructures of glassy protective layers formed on the UHTC–silicide coatings: morphology and element analysis of Zr–Si–O glass [296] (a), Ta–Si–O glass [294] (b), Hf–Si–O glass [304] (c), and Hf–Ta–B–Si–O glass [320] (d). Reproduced with permission from Ref. [296], © Elsevier Ltd. 2018; Ref. [294], © Elsevier Ltd. 2014; Ref. [304], © Elsevier Ltd. 2018; Ref. [320], © Elsevier Ltd. 2020.

Introducing silicides could improve the oxidation resistance of the UHTC coatings; however, the formed silica scales show limited applicable temperature ranges (usually below 1700 ℃). In addition to the oxidation test, the UHTC coatings will be subjected to harsher aerodynamic loads and higher temperatures during ablation test. In such extreme environments, more gas byproducts will be generated through the active oxidation of SiC which are likely to break through the top glassy layer due to the increased vapor pressure, resulting in the formation of "island" structures on the surface of UHTC–silicide coatings which destroy the continuality of the glass protective layer [292,295]. As a result, when the ablation temperature is higher than 2000 ℃, the ablation performance of the coating mainly relies on the transition metal (TM) oxides (for example ZrO_2 and HfO_2). In other words, the stability of the TM oxides determines the ablation performances of the UHTC coatings. However, it is not only the consumption of glass phase caused by the evaporation and the denudation of high-velocity steam, but also the volume change resulted from the phase transformation of TM oxides (tetragonal to monoclinic HfO_2 or ZrO_2) that lead to the integrity degradation and even peeling off of the TM oxides layer. The addition of rare earth (RE) compounds can react with TM oxides and promote the formation of RETM oxides such as $La_2Zr_2O_7$ [337] to

stabilize their tetragonal phases, thereby contributing to the improvement of ablation performances. In addition, the solid solution sintering between the Hf/Zr/Ta oxides can also lead to the formation of dense oxide protective layer [302,303,308]. These are the main reasons for the ablation resistance improvements of RE modified UHTC–silicide coatings and UHTC–UHTC coatings.

The aerospace development is putting higher requirements for UHTC coatings, that is they can service longer time and have better resistance to higher temperature/stronger scouring. To meet these demands, research efforts should direct to further improving the coating cohesion, alleviating the UHTC/substrate CTE mismatch, optimizing the type and quantity of glass-forming elements, and enhancing the thermal stability of TM oxides (stabilize the phase and promote the sintering).

5 High-entropy UHTCs: An emerging direction for the development of ultra-high temperature materials

5. 1 Introduction of high-entropy UHTCs

The concept of high-entropy alloys inspires the development of high-entropy ceramics. High-entropy alloys consisted of five or more metal elements in equimolar or near-equimolar, which make the material have high configurational entropy (> 1.5*R*, *R* is the gas constant) and favor to form single-phase solid solution with simple crystal structures such as BCC, FCC, and HCP [358]. Some high-entropy alloys exhibited excellent properties, including high strength, high plasticity, high corrosion resistance, etc. As a result, the concept of high-entropy materials attracts more and more attention from researchers all over the world. A number of rules for the formation of high-entropy phase are proposed based on the atomic size difference, valence electron concentration, and the related thermal dynamic parameters such as enthalpy of mixing and entropy of mixing. These rules play an effective role in the design of high-entropy alloys and help researchers to understand the relationship between the chemical composition and phase structure of high-entropy alloys. However, there are many exceptions beyond these rules.

Recently, the concept of high-entropy alloys was expanded to the field of ceramics, leading to the fast development of high-entropy ceramics [359]. Many kinds of high-entropy ceramics were reported, such as high-entropy oxides [360,361], high-entropy borides [362–368], high-entropy carbides [369–372], high-entropy silicides [373,374], and high-entropy fluorides [375]. Among them, the high-entropy diborides and carbides whose related individual components are UHTCs such as ZrB_2, HfB_2, ZrC, HfC, and TaC are also called high-entropy UHTCs.

According to the published references, single-phase ceramics with equimolar or near-equimolar compositions (5–35 at%) of five or more principal cations/anions which often have > 1.5*R* per mol. of cations/anions ideal configuration entropy can be called high-entropy ceramics. Wright *et al.* [361] expanded the concept from high-entropy ceramics to compositionally-complex ceramics. The compositionally-complex ceramics contain high-entropy ceramics, entropy-stabilized ceramics, medium-entropy ceramics and/or single-phase ceramics with non-equimolar 3–4 principal (5–35 at%) cations or 1–1.5*R* per mol of cations ideal configuration entropy. Some high-entropy ceramics are also entropy-stabilized. For example, Rost *et al.* [360] prepared the first high-entropy ceramic—(Mg,Co,Ni,Cu,Zn)O in 2015. This high-entropy (Mg,Co,Ni,Cu,Zn)O ceramic is also entropy-stabilized because it shows an entropy-dominated reversible phase transition during heating and cooling cycles.

Gild *et al.* [362] reported the first high-entropy boride in 2016. And then, Sarker *et al.* [369], Castle *et al.* [370], and Yan *et al.* [376] prepared high-entropy carbides in 2018. Till now, a serious of high-entropy UHTCs have been prepared successfully, such as $(Ti_{0.2}Zr_{0.2}Hf_{0.2}Nb_{0.2}Ta_{0.2})B_2$, $(Ti_{0.2}Zr_{0.2}Hf_{0.2}Nb_{0.2}Mo_{0.2})B_2$, $(Ti_{0.2}Zr_{0.2}Hf_{0.2}Nb_{0.2}Ta_{0.2})C$, and $(Ti_{0.2}Zr_{0.2}Hf_{0.2}Ta_{0.2}W_{0.2})C$ [362–372,376–389]. All the synthesized high-entropy diborides show hexagonal crystal structure, while the developed high-entropy carbides have FCC crystal structure. Up to now, the main works are focused on the crystal structure, phase formation ability and the related theoretical model, powder synthesis, densification, mechanical properties, thermal conductivity, and oxidation resistance of high-entropy UHTCs. Besides, up to now there is no report to point out that the developed high-entropy UHTCs show any entropy-stabilized reversible phase transformation phenomenon.

5. 2 Preparation of high-entropy UHTCs

(1) Synthesis of high-entropy UHTC powders

Ceramic powders with high purity, fine particle size,

specialized particle size distribution, as well as good shaping behavior and sinterability are critical issues for producing ceramic products. Accordingly, it is believed that the synthesis of pure and fine high-entropy UHTC powders is essential for the preparation of high-performance high-entropy UHTCs.

Table 7 summarized the typical methods for high-entropy UHTC powder synthesis. Combination reaction between the transition metal mixture and boron element and boro/carbothermal of the mixture of transition metal oxides are the main routes for the synthesis of high-entropy diboride powders. The synthesis of $(Ti_{0.2}Hf_{0.2}Nb_{0.2}Ta_{0.2}Mo_{0.2})B_2$ powders via combination reaction route by self-propagating high-temperature synthesis (SHS) technique presents high efficiency, but the resulted powder often contains other boride phases [377]. Borothermal and boro/carbothermal reduction of the mixture of transition metal oxides are effective ways for the synthesis of pure high-entropy diboride powders. To completely remove the oxides by boro/carbothermal reduction, excessive boron sources are often needed, and 1550–1650 ℃ is usually required for the synthesis temperature, leading to particle sizes of 0.2–1.5 μm [363–365].

The synthesis methods of high-entropy carbide powder mainly include mechanical alloying, SHS, liquid precursor method, direct solid soluting from monocarbide, and carbothermal reduction of the mixture of the related oxides. Among these methods, SHS is the most time-saving technique. Mechanical alloying and liquid precursor methods are favorable to prepare high-entropy carbide powder with particle size less than 500 nm. Direct solid solution from monocarbides and the carbothermal reduction of the mixture of transition metal oxides are suitable for the synthesis of sub-micron/micron-sized high-entropy carbides powder in batch production at temperatures higher than 1600 ℃.

As mentioned above, many ways have been developed successfully for the synthesis of high-entropy UHTC powders. However, investigations on adjusting the characteristics of high-entropy UHTC powders and understanding the relationship between their characteristics and the compactibility and sinterability are still very needed.

(2) Preparation of bulk high-entropy UHTCs

As a new family member of UHTCs, the sintering techniques, such as PLS, HP, SPS, and reactive spark plasma sintering (RSPS) used to prepare UHTCs can also be applied to high-entropy UHTCs. HP is widely applied for the preparation of high-entropy UHTCs, such as $(Ti_{0.2}Zr_{0.2}Hf_{0.2}Nb_{0.2}Ta_{0.2})C$ [385], $(Ti_{0.2}Zr_{0.2}Hf_{0.2}Nb_{0.2}Ta_{0.2})B_2$ [368,386], and $(Ti_{0.2}Zr_{0.2}Hf_{0.2}Nb_{0.2}Ta_{0.2})B_2$–SiC ceramics [368]. The sintering temperature for HP is often higher than 1800 ℃, resulting in dense high-entropy UHTCs. Feng *et al.* [385] fabricated $(Ti_{0.2}Zr_{0.2}Hf_{0.2}Nb_{0.2}Ta_{0.2})C$ ceramic with a relative density of 99.3% by HP at 1900 ℃ under a uniaxial pressure of 32 MPa.

Compared to PLS and HP, SPS is the most commonly sintering technique used for dense high-entropy UHTCs due to its advantage of time-saving. The first high-entropy boride ceramic was fabricated by SPS at 2000 ℃ for 5 min using high-energy ball-milled transition metal diboride powders as starting material [362]. Lu *et al.* [372] prepared dense $(Ti_{0.2}Zr_{0.2}Hf_{0.2}Nb_{0.2}Ta_{0.2})C$ and $(Ti_{0.2}Zr_{0.2}Hf_{0.2}Nb_{0.2}Ta_{0.2})C$–SiC ceramics with high relative densities by SPS at 1800 ℃ using a dual-phase high-entropy carbide powder synthesized via

Table 7 Methods for the synthesis of high-entropy UHTC powders

High-entropy UHTC powders	Synthesis method		Particle size (μm)	Ref.
$(Ti_{0.2}Hf_{0.2}Nb_{0.2}Ta_{0.2}Mo_{0.2})B_2$	M+B	SHS+ball milling	1.94	[377]
$(Ti_{0.2}Zr_{0.2}Hf_{0.2}Nb_{0.2}Mo_{0.2})B_2$	MO_x+B	Borothermal reduction	0.36	[363]
$(Ti_{0.2}Zr_{0.2}Hf_{0.2}Nb_{0.2}Ta_{0.2})B_2$	MO_x+B_4C MO_x+B_4C+C	Boro/carbothermal reduction	0.2–1.5	[364,368,379,380]
$(Ti_{0.2}Zr_{0.2}Hf_{0.2}V_{0.2}Nb_{0.2})C$	M+C	Mechanical alloying	0.1–0.3	[381]
$(Ti_{0.2}Hf_{0.2}Nb_{0.2}Ta_{0.2}Mo_{0.2})C$	M+C	SHS	—	[382]
	MCl_x	Liquid precursor method	0.132	[383]
$(Ti_{0.2}Zr_{0.2}Hf_{0.2}Nb_{0.2}Ta_{0.2})C$	MC	Direct solid soluting	2	[378]
	MO_x+C	Carbothermal reduction	0.5–1.5	[384]

*M, MO_x, and MCl_x are the mixture of five transition metal elements, five transition metal oxides, and the mixture of five transition metal chlorides, respectively.

carbothermal reduction route. Wei *et al.* [371] prepared dense $(Ti_{0.2}Zr_{0.2}Hf_{0.2}Nb_{0.2}Ta_{0.2})C$ ceramics by RSPS via three different routes: the mixture of metal elements and carbon, the mixture of five individual carbides and the mixture of oxides and carbon, respectively. The obtained ceramics through the different routes showed different microstructure features. Gild *et al.* [387] developed a new method based on RSPS and flash sintering technique, which is called reactive flash SPS (ReaFSPS) for the fast densification of high-entropy UHTCs. Dense $(Ti_{0.2}Zr_{0.2}Hf_{0.2}Nb_{0.2}Ta_{0.2})B_2$ and $(Ti_{0.2}Zr_{0.2}Hf_{0.2}Nb_{0.2}Ta_{0.2})C$ ceramics with 3 wt% graphite addition can be achieved in 120 s by ReaFSPS.

Although dense high-entropy UHTCs can be successfully prepared by advanced sintering techniques, the sintering temperature is often higher than 1800 ℃. Such high temperature not only causes high energy consumption but also results in a coarse microstructure. Chen *et al.* [367] prepared porous high-entropy $(Ti_{0.2}Zr_{0.2}Hf_{0.2}Nb_{0.2}Ta_{0.2})B_2$ ceramics by an *in-situ* boro/carbothermal reduction combined with a partial PLS process. The thermal conductivity of this material is as low as 0.51 $W\cdot m^{-1}\cdot K^{-1}$, which making it a proper UHTCs thermal insulating candidate.

How to decrease the sintering temperature is still challenge in the field of high-entropy UHTCs. Moreover, the microstructure tailoring by the design of composition and processing remains needing systematically studies.

5. 3 Properties of high-entropy UHTCs

Like other ceramic materials, the mechanical properties of high-entropy UHTCs are also susceptible to the microstructure of the ceramics. For example, the four-point bending strength of hot-pressed $(Ti_{0.2}Zr_{0.2}Hf_{0.2}Nb_{0.2}Ta_{0.2})B_2$ ceramic with a relative density of 99.8% and average grain size of 4.06 μm is about 339 MPa. With the addition of 20 vol% SiC, the average grain size of $(Ti_{0.2}Zr_{0.2}Hf_{0.2}Nb_{0.2}Ta_{0.2})B_2$ matrix phase decreases to 2.70 μm, which makes bending strength of $(Ti_{0.2}Zr_{0.2}Hf_{0.2}Nb_{0.2}Ta_{0.2})B_2$–20 vol%SiC increased to about 447 MPa. Besides, the fracture toughness of $(Ti_{0.2}Zr_{0.2}Hf_{0.2}Nb_{0.2}Ta_{0.2})B_2$–20 vol%SiC ceramic measured by SENB (single-edge notched beam) method is also higher than that of the single-phase $(Ti_{0.2}Zr_{0.2}Hf_{0.2}Nb_{0.2}Ta_{0.2})B_2$ [368]. Dense high-entropy UHTCs often show Vickers hardness $HV_{0.2}$ of about 20–35 GPa, which is higher than that of the average performances of the individual metal diborides or carbides [362–372,388–390]. The hardness of high-entropy UHTCs is not only controlled by their average grain size but also strongly affected by their composition. Qin *et al.* [391] found that high-entropy borides containing W and Mo elements have higher hardness than $(Ti_{0.2}Zr_{0.2}Hf_{0.2}Nb_{0.2}Ta_{0.2})B_2$ ceramic.

As the strong phonon scattering by the serious lattice distortion, the thermal conductivity of dense high-entropy UHTC is lower than their related individual metal diborides and carbides. The thermal conductivities of $(Ti_{0.2}Zr_{0.2}Hf_{0.2}Nb_{0.2}Ta_{0.2})B_2$, $(Ti_{0.2}Zr_{0.2}Hf_{0.2}Ta_{0.2}Mo_{0.2})B_2$, and $(Ti_{0.2}Zr_{0.2}Hf_{0.2}Ta_{0.2}Cr_{0.2})B_2$ ceramics are about 24.8, 15.2, and 12.6 $W\cdot m^{-1}\cdot K^{-1}$, respectively, which are much lower than those (~100 $W\cdot m^{-1}\cdot K^{-1}$) of ZrB_2 and HfB_2 ceramics [392–394]. The thermal conductivity of high-entropy UHTC can be affected by its oxygen impurity content. The addition of graphite can effectively remove the oxygen impurity in $(Ti_{0.2}Zr_{0.2}Hf_{0.2}Nb_{0.2}Ta_{0.2})C$ ceramics and improve their thermal conductivity [395].

Oxidation resistance is another important property of high-entropy UHTCs [362,396–398]. The oxidation resistance of high-entropy diboride is better than that of the average performances of the individual metal diborides [362]. Backman *et al.* [396] pointed out that the composition diversity of high-entropy ceramics provides an opportunity to improve the oxidation resistance of the material based on the oxidation resistance order of its individual metal diborides and carbides. Moreover, the addition of SiC in $(Ti_{0.2}Zr_{0.2}Hf_{0.2}Nb_{0.2}Ta_{0.2})C$ ceramic can enhance its oxidation resistance through the formation of $Hf(Zr)SiO_4$ and $Hf(Zr)TiO_4$ protective oxide layer [396].

Previous works mainly focus on the mechanical properties at room temperature, thermal conductivity, and oxidation resistance of high-entropy UHTCs. However, as one candidate for ultra-high temperature applications, the high-temperature strength, ablation resistance, thermal shock resistance, as well as melting points are critical, which need intensive studies in the future.

5. 4 Applications of high-entropy UHTCs

Like conventional UHTCs, high-entropy UHTCs also have several application forms, such as bulk ceramics, ceramic matrix for fiber-reinforced ceramic composite, and ceramic coatings. Compared to the bulk high-entropy UHTCs, fiber-reinforced high-entropy UHTCs are expected to have higher mechanical reliability and the

high-entropy UHTC coatings can take full advantage of the high oxidation resistance of high-entropy UHTCs. Investigations on fiber-reinforced high-entropy UHTC composites and high-entropy UHTC coatings are very important. Just recently, Cai *et al.* [399] reported $C_f/(Ti_{0.2}Zr_{0.2}Hf_{0.2}Nb_{0.2}Ta_{0.2})C$–SiC high-entropy UHTC composite for the first time, which shows outstanding bending strength (322 MPa), fracture toughness (8.24 $MPa \cdot m^{1/2}$), and linear recession rate of 2.89 $\mu m \cdot s^{-1}$ at a heat flux density of 5 $MW \cdot m^{-2}$. However, studies on high-entropy UHTC composites and high-entropy UHTC coatings are very scarce till now.

In a summary, high-entropy UHTC is a new kind of UHTCs. It shows a series of good properties and is a potential candidate for ultra-high temperature applications. However, systematical investigations on the relationship among the composition, processing, microstructure, and property of high-entropy UHTCs are urgently needed. For the powder synthesis, adjusting the characteristics of high-entropy UHTC powders and understanding the relationship between their characteristics and the formability and sinterability are key issues in further work. For the preparation of high-entropy UHTCs, new sintering technologies and microstructure controlling approaches are important research interests. Fiber-reinforced high-entropy UHTC composites and high-entropy UHTC coatings will be hot topics in the future. For the properties, high-temperature strength, ablation resistance, thermal shock resistance, and even the melting points of high-entropy UHTCs and their composites are very worth to be studied.

6 Summary and outlook

UHTCs are generally referred to the carbides, nitrides, and borides of the transition metals, with the Group IVB compounds (Zr & Hf) and TaC as the main focus. Carbide and nitride UHTCs commonly have a face-centered cubic structure, while boride UHTCs have the AlB_2 structure (*P*6/*mmm*) composed of alternating planes of hexagonally close-packed metal atoms and graphite-like B atoms. The strong covalent structure endows the UHTCs with ultra-high melting points, excellent mechanical properties, and ablation resistance at elevated temperatures. These unique combinations of properties make UHTCs leading candidates for extremely environmental structural applications in rocket and hypersonic vehicles. Generally, bulk UTHCs are severely limited by their low fracture toughness and poor thermal shock resistance, hindering their direct use as external thermal protection systems on leading edges and propulsion systems. Although various toughening methods, such as particles, whiskers, carbon nanotubes, and graphene, have been developed, the reliability of bulk UHTCs still cannot meet the requirements of engineering applications. To solve the intrinsic brittleness of bulk ceramics fundamentally, coatings and fibers reinforced ceramic matrix composites are developed as the main application forms for UHTCs. This review presents the advances of processing approaches, composition and microstructure design, properties and mechanisms of UHTCs including from bulk materials to composites and coatings. In particular, the relationships among composition–processing–structure–properties of UHTCs are discussed. In the past few years, high-entropy UHTCs are developed rapidly as an emerging direction for ultra-high temperature materials, which has also been discussed in this review.

For the further development of UHTCs, there are still quite a few challenges should be considered. Technically and economically successful fabrication of the UHTCs and their high-performance retentions in extremely environmental conditions remain challenging.

1) Carbon fibers are the most commonly used reinforcements for UHTCMCs. However, the poor anti-oxidation properties of carbon fibers intrinsically restrict the performance of UHTCMCs under more extreme conditions. Development of UHTC fibers and $UHTC_f$/UHTCs can improve the performance of UHTCMCs fundamentally. Currently, only the US Matech GSM has reported the development of UHTC fibers, such as HfC fibers, TaC fibers, and $UHTC_f$/UHTC composites. There is still a long way to go before the commercialization and application of the UHTC fibers and $UHTC_f$/ UHTC composites.

2) Generally, property requirements of UHTC thermal structures at different areas are quite different. Therefore, composition and microstructure generally need to be designed to satisfy the specific requirements at different regions of the thermal structure. Joining the different parts as an integrity and its reliability under extreme service conditions are another big challenge for

UHTCs. More efforts need to be taken toward technology breakthroughs such as cost-effective preparation, improved interphase quality, especially good thermal expansion compatibility between different parts, and enhanced ultra-high temperature stability in aggressive aero-thermo-chemical environments.

3) Characterizations of the UHTCs at real or near-real extreme service conditions are critical to reveal their actual failure mechanisms during service. This can provide a more accurate direction for material design to achieve high performance and long service life. Although various techniques have been developed, new and ever-more realistic testing is still required. In particular, tests that can be done rapidly and at low cost and which provide excellent guidance on the performance of the UHTCs and components under real or near real environmental conditions are needed.

4) Multiscale modelling, from Density Functional Theory (DFT) to Finite Element Analysis (FEA) and Computational Fluid Dynamics (CFD) will become essential. Integrated computational models which link across among composition, microstructure, processing, and properties are strongly required to be created and validated based on extensive experimental work and characterization. Although it is not easy, it will significantly reduce the costs for developing new UHTCs that offer the required properties.

Acknowledgements

The financial support from the National Natural Science Foundation of China (52032001, 52022072, 52032003, 51972243, 92060202, 51872239, 51872059, 51772061, 52061135102, 52002321, 50632070, 51272266, and 52102093), bilateral project of NSFC–JSPS (51111140017 and 51611140121), China Postdoctoral Science Foundation (2021M690817), Fundamental Research Funds for the Central Universities (G2020KY05125), Key Research Program of Frontier Sciences, CAS (QYZDY-SSW-JSC031), the projects supported by the State Key Laboratory of Advanced Technology for Materials Synthesis and Processing, Wuhan University of Technology (2021-KF-5), and the State Key Laboratory for Modification of Chemical Fibers and Polymer Materials, Donghua University (KF2116) are greatly acknowledged. The authors also would like to thank Prof. Shi C. Zhang (Missouri University of Science and Technology, Rolla, Missouri, USA) for language proofreading and helpful suggestions.

References

[1] Telle R, Sigl LS, Takagi K. Boride-based hard materials. In *Handbook of Ceramic Hard Materials*. Weinheim, Germany: Wiley-VCH Verlag GmbH, 2000: 802–945.

[2] Fahrenholtz WG, Hilmas GE. Oxidation of ultra-high temperature transition metal diboride ceramics. *Int Mater Rev* 2012, **57**: 61–72.

[3] Eakins E, Jayaseelan DD, Lee WE. Toward oxidation-resistant ZrB_2–SiC ultra high temperature ceramics. *Metall Mater Trans A* 2011, **42**: 878–887.

[4] Guo SQ. Densification of ZrB_2-based composites and their mechanical and physical properties: A review. *J Eur Ceram Soc* 2009, **29**: 995–1011.

[5] Binner J, Porter M, Baker B, *et al*. Selection, processing, properties and applications of ultra-high temperature ceramic matrix composites, UHTCMCs—A review. *Int Mater Rev* 2020, **65**: 389–444.

[6] Liu PC, Zhang PC, Pang XX, *et al*. A study on fabrication technique of ZrB_2 target. *Procedia Eng* 2012, **27**: 1305–1312.

[7] Nasseri MM. Comparison of HfB_2 and ZrB_2 behaviors for using in nuclear industry. *Ann Nucl Energy* 2018, **114**: 603–606.

[8] Middleburgh SC, Parfitt DC, Blair PR, *et al*. Atomic scale modeling of point defects in zirconium diboride. *J Am Ceram Soc* 2011, **94**: 2225–2229.

[9] Glaser FW, Post B. System zirconium-boron. *JOM* 1953, **5**: 1117–1118.

[10] Rogl P, Potter PE. A critical review and thermodynamic calculation of the binary system: Zirconium-boron. *Calphad* 1988, **12**: 191–204.

[11] Mchale AE. *Phase Diagrams for Ceramists Volume X: Borides*, *Carbides*, *and Nitrides*. Westerville, OH, USA: The American Ceramic Society, 1994.

[12] Opeka MM, Talmy IG, Wuchina EJ, *et al*. Mechanical, thermal, and oxidation properties of refractory hafnium and zirconium compounds. *J Eur Ceram Soc* 1999, **19**: 2405–2414.

[13] Kaplan FS, Kalyada TL, Gaenko NS, *et al*. Porous structure of the periclase plates of steel-teeming ladle slide gates. *Refractories* 1982, **23**: 625–630.

[14] Opila E, Levine S, Lorincz J. Oxidation of ZrB_2- and HfB_2-based ultra-high temperature ceramics: Effect of Ta additions. *J Mater Sci* 2004, **39**: 5969–5977.

[15] Venkateswaran T, Basu B, Raju GB, *et al*. Densification and properties of transition metal borides-based cermets via spark plasma sintering. *J Eur Ceram Soc* 2006, **26**: 2431–2440.

[16] Chamberlain AL, Fahrenholtz WG, Hilmas GE, *et al*. High-strength zirconium diboride-based ceramics. *J Am Ceram Soc* 2004, **87**: 1170–1172.

[17] Cotton J. Ultra-high-temperature ceramics. *Adv Mater Process* 2010, **168**: 26–28.

[18] Fahrenholtz WG, Hilmas GE, Talmy IG, *et al*. Refractory

diborides of zirconium and hafnium. *J Am Ceram Soc* 2007, **90**: 1347–1364.

[19] Hwang SS, Vasiliev AL, Padture NP. Improved processing an oxidation-resistance of ZrB_2 ultra-high temperature ceramics containing SiC nanodispersoids. *Mater Sci Eng A* 2007, **464**: 216–224.

[20] Rueschhoff LM, Carney CM, Apostolov ZD, *et al*. Processing of fiber-reinforced ultra-high temperature ceramic composites: A review. *Int J Ceram Eng Sci* 2020, **2**: 22–37.

[21] Rubio V, Ramanujam P, Cousinet S, *et al*. Thermal properties and performance of carbon fiber-based ultra-high temperature ceramic matrix composites (C_f-UHTCMCs). *J Am Ceram Soc* 2020, **103**: 3788–3796.

[22] Ding Q, Ni DW, Wang Z, *et al*. 3D C_f/SiBCN composites prepared by an improved polymer infiltration and pyrolysis. *J Adv Ceram* 2018, **7**: 266–275.

[23] Chen BW, Ding Q, Ni DW, *et al*. Microstructure and mechanical properties of 3D C_f/SiBCN composites fabricated by polymer infiltration and pyrolysis. *J Adv Ceram* 2021, **10**: 28–38.

[24] Tang SF, Deng JY, Wang SJ, *et al*. Fabrication and characterization of an ultra-high-temperature carbon fiber-reinforced ZrB_2–SiC matrix composite. *J Am Ceram Soc* 2007, **90**: 3320–3322.

[25] Sayir A. Carbon fiber reinforced hafnium carbide composite. *J Mater Sci* 2004, **39**: 5995–6003.

[26] Cecere A, Savino R, Allouis C, *et al*. Heat transfer in ultra-high temperature advanced ceramics under high enthalpy arc-jet conditions. *Int J Heat Mass Transf* 2015, **91**: 747–755.

[27] Murthy TSRC, Reeman L, Zou J, *et al*. Role of rare earth oxide particles on the oxidation behaviour of silicon carbide coated 2.5D carbon fibre preforms. *Open Ceram* 2020, **2**: 100018.

[28] Zou J, Zhang GJ, Kan YM. Formation of tough interlocking microstructure in ZrB_2–SiC-based ultrahigh-temperature ceramics by pressureless sintering. *J Mater Res* 2009, **24**: 2428–2434.

[29] Zou J, Ma HB, Liu JJ, *et al*. Nanoceramic composites with duplex microstructure break the strength–toughness tradeoff. *J Mater Sci Technol* 2020, **58**: 1–9.

[30] Pazhouhanfar Y, Sabahi Namini A, Shaddel S, *et al*. Combined role of SiC particles and SiC whiskers on the characteristics of spark plasma sintered ZrB_2 ceramics. *Ceram Int* 2020, **46**: 5773–5778.

[31] Jin H, Meng SH, Xie WH, *et al*. HfB_2–CNTs composites with enhanced mechanical properties prepared by spark plasma sintering. *Ceram Int* 2017, **43**: 2170–2173.

[32] Zhou P, Hu P, Zhang XH, *et al*. R-curve behavior of laminated ZrB_2–SiC ceramic with strong interfaces. *Int J Refract Met Hard Mater* 2015, **52**: 12–16.

[33] Sciti D, Pienti L, Fabbriche DD, *et al*. Combined effect of SiC chopped fibers and SiC whiskers on the toughening of ZrB_2. *Ceram Int* 2014, **40**: 4819–4826.

[34] Silvestroni L, Sciti D, Melandri C, *et al*. Toughened ZrB_2-based ceramics through SiC whisker or SiC chopped fiber additions. *J Eur Ceram Soc* 2010, **30**: 2155–2164.

[35] Silvestroni L, Dalle Fabbriche D, Melandri C, *et al*. Relationships between carbon fiber type and interfacial domain in ZrB_2-based ceramics. *J Eur Ceram Soc* 2016, **36**: 17–24.

[36] Pulci G, Tului M, Tirillò J, *et al*. High temperature mechanical behavior of UHTC coatings for thermal protection of Re-entry vehicles. *J Therm Spray Technol* 2011, **20**: 139–144.

[37] Corral EL, Walker LS. Improved ablation resistance of C-C composites using zirconium diboride and boron carbide. *J Eur Ceram Soc* 2010, **30**: 2357–2364.

[38] Li SP, Li KZ, Li HJ, *et al*. Effect of HfC on the ablative and mechanical properties of C/C composites. *Mater Sci Eng*: *A* 2009, **517**: 61–67.

[39] Pavese M, Fino P, Badini C, *et al*. HfB_2/SiC as a protective coating for 2D Cf/SiC composites: Effect of high temperature oxidation on mechanical properties. *Surf Coat Technol* 2008, **202**: 2059–2067.

[40] Corral EL, Loehman RE. Ultra-high-temperature ceramic coatings for oxidation protection of carbon–carbon composites. *J Am Ceram Soc* 2008, **91**: 1495–1502.

[41] Blum YD, Marschall J, Hui D, *et al*. Thick protective UHTC coatings for SiC-based structures: Process establishment. *J Am Ceram Soc* 2008, **91**: 1453–1460.

[42] Cheng LF, Xu YD, Zhang LT, *et al*. Oxidation behavior from room temperature to 1500 ℃ of 3D-C/SiC composites with different coatings. *J Am Ceram Soc* 2004, **85**: 989–991.

[43] Ushakov SV, Navrotsky A, Hong QJ, *et al*. Carbides and nitrides of zirconium and hafnium. *Materials* 2019, **12**: 2728.

[44] Mei ZG, Bhattacharya S, Yacout AM. First-principles study of fracture toughness enhancement in transition metal nitrides. *Surf Coat Technol* 2019, **357**: 903–909.

[45] Kuo CC, Lin YT, Chan A, *et al*. High temperature wear behavior of titanium nitride coating deposited using high power impulse magnetron sputtering. *Coatings* 2019, **9**: 555.

[46] Demirskyi D, Solodkyi I, Nishimura T, *et al*. Fracture and property relationships in the double diboride ceramic composites by spark plasma sintering of TiB_2 and NbB_2. *J Am Ceram Soc* 2019, **102**: 4259–4271.

[47] Jin XC, Fan XL, Lu CS, *et al*. Advances in oxidation and ablation resistance of high and ultra-high temperature ceramics modified or coated carbon/carbon composites. *J Eur Ceram Soc* 2018, **38**: 1–28.

[48] Harrison RW, Lee WE. Processing and properties of ZrC, ZrN and ZrCN ceramics: A review. *Adv Appl Ceram* 2016, **115**: 294–307.

[49] Harrison RW, Lee WE. Mechanism and kinetics of oxidation of ZrN ceramics. *J Am Ceram Soc* 2015, **98**: 2205–2213.

[50] Li D, Tian FB, Duan DF, *et al*. Mechanical and metallic properties of tantalum nitrides from first-principles calculations. *RSC Adv* 2014, **4**: 10133.

[51] Tallon C, Franks GV. Near-net-shaping of ultra-high temperature ceramics. In *Ultra-High Temperature Ceramics*. Hoboken, NJ, USA: John Wiley & Sons, Inc, 2014: 83–111.

[52] Zapata-Solvas E, Jayaseelan DD, Lin HT, *et al*. Mechanical properties of ZrB_2- and HfB_2-based ultra-high temperature ceramics fabricated by spark plasma sintering. *J Eur Ceram Soc* 2013, **33**: 1373–1386.

[53] Information on https://hal.archives-ouvertes.fr/hal-01183657/document.

[54] Wuchina E, Opila E, Opeka M, *et al*. UHTCs: Ultra-high temperature ceramic materials for extreme environment applications. *Electrochem Soc Interface* 2007, **16**: 30–36.

[55] Matsushita J, Hwang GC, Shim KB. Oxidation behavior of tantalum boride ceramics. *Solid State Phenom* 2007, **124–126**: 819–822.

[56] Basu B, Raju GB, Suri AK. Processing and properties of monolithic TiB_2 based materials. *Int Mater Rev* 2006, **51**: 352–374.

[57] Koh YH, Lee SY, Kim HE. Oxidation behavior of titanium boride at elevated temperatures. *J Am Ceram Soc* 2001, **84**: 239–241.

[58] Lévy F, Hones P, Schmid PE, *et al*. Electronic states and mechanical properties in transition metal nitrides. *Surf Coat Technol* 1999, **120–121**: 284–290.

[59] Yu RM, Sun EM, Jiao LG, *et al*. Crystal structures of transition metal pernitrides predicted from first principles. *RSC Adv* 2018, **8**: 36412–36421.

[60] Barraud E, Bégin-Colin S, Le Caër G, *et al*. Mechanically activated solid-state synthesis of hafnium carbide and hafnium nitride nanoparticles. *J Alloys Compd* 2008, **456**: 224–233.

[61] Ibidunni AO, Masaitis RL, Opila RL, *et al*. Characterization of the oxidation of tantalum nitride. *Surf Interface Anal* 1993, **20**: 559–564.

[62] Voitovich RF, Pugach ÉA. High-temperature oxidation characteristics of the carbides of the Group VI transition metals. *Sov Powder Metall Met Ceram* 1973, **12**: 314–318.

[63] Karwal S, Verheijen MA, Arts K, *et al*. Plasma-assisted ALD of highly conductive HfN_x: On the effect of energetic ions on film microstructure. *Plasma Chem Plasma Process* 2020, **40**: 697–712.

[64] Lu HP, Ran YJ, Zhao SJ, *et al*. Effects of assisting ions on the structural and plasmonic properties of ZrN_x thin films. *J Phys D*: *Appl Phys* 2019, **52**: 245102.

[65] Wu YY, Kohn A, Eizenberg M. Structures of ultra-thin atomic-layer-deposited TaN_x films. *J Appl Phys* 2004, **95**: 6167–6174.

[66] Fleurence A, Friedlein R, Ozaki T, *et al*. Experimental evidence for epitaxial silicene on diboride thin films. *Phys Rev Lett* 2012, **108**: 245501.

[67] Sciti D, Silvestroni L, Bellosi A. Fabrication and properties of HfB_2–$MoSi_2$ composites produced by hot pressing and spark plasma sintering. *J Mater Res* 2006, **21**: 1460–1466.

[68] Monteverde F, Bellosi A. Beneficial effects of AlN as sintering aid on microstructure and mechanical properties of hot-pressed ZrB_2. *Adv Eng Mater* 2003, **5**: 508–512.

[69] Wang MF, Wang CG, Zhang XH. Effects of SiC platelet and $ZrSi_2$ additive on sintering and mechanical properties of ZrB_2-based ceramics by hot-pressing. *Mater Des* 2012, **34**: 293–297.

[70] Sciti D, Silvestroni L, Celotti G, *et al*. Sintering and mechanical properties of ZrB_2–$TaSi_2$ and HfB_2–$TaSi_2$ ceramic composites. *J Am Ceram Soc* 2008, **91**: 3285–3291.

[71] Wang XG, Liu JX, Kan YM, *et al*. Effect of solid solution formation on densification of hot-pressed ZrC ceramics with MC (M = V, Nb, and Ta) additions. *J Eur Ceram Soc* 2012, **32**: 1795–1802.

[72] Wang XG, Guo WM, Kan YM, *et al*. Densification behavior and properties of hot-pressed ZrC ceramics with Zr and graphite additives. *J Eur Ceram Soc* 2011, **31**: 1103–1111.

[73] Medri V, Monteverde F, Balbo A, *et al*. Comparison of ZrB_2–ZrC–SiC composites fabricated by spark plasma sintering and hot-pressing. *Adv Eng Mater* 2005, **7**: 159–163.

[74] Vafa NP, Shahedi Asl M, Jaberi Zamharir M, *et al*. Reactive hot pressing of ZrB_2-based composites with changes in ZrO_2/SiC ratio and sintering conditions. Part I: Densification behavior. *Ceram Int* 2015, **41**: 8388–8396.

[75] Wang XG, Zhang GJ, Xue JX, *et al*. Reactive hot pressing of ZrC–SiC ceramics at low temperature. *J Am Ceram Soc* 2013, **96**: 32–36.

[76] Guo WM, Yang ZG, Zhang GJ. Comparison of ZrB_2–SiC ceramics with Yb_2O_3 additive prepared by hot pressing and spark plasma sintering. *Int J Refract Met Hard Mater* 2011, **29**: 452–455.

[77] Qu Q, Zhang XH, Meng SH, *et al*. Reactive hot pressing and sintering characterization of ZrB_2–SiC–ZrC composites. *Mater Sci Eng*: *A* 2008, **491**: 117–123.

[78] Wu WW, Zhang GJ, Kan YM, *et al*. Synthesis and microstructural features of ZrB_2–SiC-based composites by reactive spark plasma sintering and reactive hot pressing. *Scripta Mater* 2007, **57**: 317–320.

[79] Monteverde F. Ultra-high temperature HfB_2–SiC ceramics consolidated by hot-pressing and spark plasma sintering. *J Alloys Compd* 2007, **428**: 197–205.

[80] Yan YJ, Huang ZR, Dong SM, *et al*. Pressureless sintering of high-density ZrB_2–SiC ceramic composites. *J Am Ceram Soc* 2006, **89**: 3589–3592.

[81] Chamberlain AL, Fahrenholtz WG, Hilmas GE. Pressureless sintering of zirconium diboride. *J Am Ceram Soc* 2006, **89**: 450–456.

[82] Fahrenholtz WG, Hilmas GE, Zhang SC, *et al*. Pressureless sintering of zirconium diboride: Particle size and additive effects. *J Am Ceram Soc* 2008, **91**: 1398–1404.

[83] Liu JX, Kan YM, Zhang GJ. Pressureless sintering of tantalum carbide ceramics without additives. *J Am Ceram Soc* 2010, **93**: 370–373.

[84] Liu JX, Kan YM, Zhang GJ. Synthesis of ultra-fine hafnium carbide powder and its pressureless sintering. *J Am Ceram Soc* 2010, **93**: 980–986.

[85] Wang XG, Guo WM, Zhang GJ. Pressureless sintering mechanism and microstructure of ZrB_2–SiC ceramics doped with boron. *Scripta Mater* 2009, **61**: 177–180.

[86] Zhang SC, Hilmas GE, Fahrenholtz WG. Pressureless densification of zirconium diboride with boron carbide additions. *J Am Ceram Soc* 2006, **89**: 1544–1550.

[87] Dole SL, Prochazka S, Doremus RH. Microstructural coarsening during sintering of boron carbide. *J Am Ceram Soc* 1989, **72**: 958–966.

[88] Liu JX, Zhang GJ, Xu FF, *et al*. Densification, microstructure evolution and mechanical properties of WC doped HfB_2–SiC ceramics. *J Eur Ceram Soc* 2015, **35**: 2707–2714.

[89] Zou J, Zhang GJ, Kan YM, *et al*. Hot-pressed ZrB_2–SiC ceramics with VC addition: Chemical reactions, microstructures, and mechanical properties. *J Am Ceram Soc* 2009, **92**: 2838–2846.

[90] Monteverde F, Grohsmeyer RJ, Stanfield AD, *et al*. Densification behavior of ZrB_2–$MoSi_2$ ceramics: The formation and evolution of core–shell solid solution structures. *J Alloys Compd* 2019, **779**: 950–961.

[91] Sun X, Han WB, Liu Q, *et al*. ZrB_2-ceramic toughened by refractory metal Nb prepared by hot-pressing. *Mater Des* 2010, **31**: 4427–4431.

[92] Wang HL, Chen DL, Wang CA, *et al*. Preparation and characterization of high-toughness ZrB_2/Mo composites by hot-pressing process. *Int J Refract Met Hard Mater* 2009, **27**: 1024–1026.

[93] Liu Q, Han WB, Hu P. Microstructure and mechanical properties of ZrB_2–SiC nanocomposite ceramic. *Scripta Mater* 2009, **61**: 690–692.

[94] Li WJ, Zhang XH, Hong CQ, *et al*. Microstructure and mechanical properties of zirconia-toughened ZrB_2–$MoSi_2$ composites prepared by hot-pressing. *Scripta Mater* 2009, **60**: 100–103.

[95] Han WB, Li G, Zhang XH, *et al*. Effect of AlN as sintering aid on hot-pressed ZrB_2–SiC ceramic composite. *J Alloys Compd* 2009, **471**: 488–491.

[96] Guo SQ, Kagawa Y, Nishimura T. Mechanical behavior of two-step hot-pressed ZrB_2-based composites with $ZrSi_2$. *J Eur Ceram Soc* 2009, **29**: 787–794.

[97] Zhang XH, Xu L, Du SY, *et al*. Thermal shock behavior of SiC-whisker-reinforced diboride ultrahigh-temperature ceramics. *Scripta Mater* 2008, **59**: 55–58.

[98] Monteverde F, Guicciardi S, Bellosi A. Advances in microstructure and mechanical properties of zirconium diboride based ceramics. *Mater Sci Eng*: *A* 2003, **346**: 310–319.

[99] Meléndez-Martínez JJ, Domínguez-Rodríguez A, Monteverde F, *et al*. Characterisation and high temperature mechanical properties of zirconium boride-based materials. *J Eur Ceram Soc* 2002, **22**: 2543–2549.

[100] Andrievskii RA, Korolev LA, Klimenko VV, *et al*. Effect of zirconium carbide and carbon additions on some physicomechanical properties of zirconium diboride. *Sov Powder Metall Met Ceram* 1980, **19**: 93–94.

[101] Čech B, Oliverius P, Sejbal J. Sintering of zirconium boride with activating additions. *Powder Metall* 1965, **8**: 142–151.

[102] Kislyi PS, Kuzenkova MA. Regularities of sintering of zirconium–diboride–molybenum alloys. *Sov Powder Metall Met Ceram* 1966, **5**: 360–365.

[103] Einarsrud MA, Hagen E, Pettersen G, *et al*. Pressureless sintering of titanium diboride with nickel, nickel boride, and iron additives. *J Am Ceram Soc* 1997, **80**: 3013–3020.

[104] Sciti D, Brach M, Bellosi A. Oxidation behavior of a pressureless sintered ZrB_2–$MoSi_2$ ceramic composite. *J Mater Res* 2005, **20**: 922–930.

[105] Rodríguez-Sánchez J, Sánchez-González E, Guiberteau F, *et al*. Contact-mechanical properties at intermediate temperatures of ZrB_2 ultra-high-temperature ceramics pressureless sintered with Mo, Ta, or Zr disilicides. *J Eur Ceram Soc* 2015, **35**: 3179–3185.

[106] Zhu SM, Fahrenholtz WG, Hilmas GE, *et al*. Pressureless sintering of zirconium diboride using boron carbide and carbon additions. *J Am Ceram Soc* 2007, **90**: 3660–3663.

[107] Ma HB, Zou J, Lu P, *et al*. Oxygen contamination on the surface of ZrB_2 powders and its removal. *Scripta Mater* 2017, **127**: 160–164.

[108] Zou J, Zhang GJ, Sun SK, *et al*. ZrO_2 removing reactions of Groups IV–VI transition metal carbides in ZrB_2 based composites. *J Eur Ceram Soc* 2011, **31**: 421–427.

[109] Ni DW, Liu JX, Zhang GJ. Pressureless sintering of HfB_2–SiC ceramics doped with WC. *J Eur Ceram Soc* 2012, **32**: 3627–3635.

[110] Zou J, Sun SK, Zhang GJ, *et al*. Chemical reactions, anisotropic grain growth and sintering mechanisms of self-reinforced ZrB_2–SiC doped with WC. *J Am Ceram Soc* 2011, **94**: 1575–1583.

[111] Zou J, Zhang GJ, Kan YM. Formation of tough interlocking microstructure in ZrB_2–SiC-based ultrahigh-temperature ceramics by pressureless sintering. *J Mater Res* 2009, **24**: 2428–2434.

[112] Krishnarao RV, Sankarasubramanian R. Thermite assisted synthesis of ZrB_2 and ZrB_2–SiC through B_4C reduction of ZrO_2 and $ZrSiO_4$ in air. *J Adv Ceram* 2017, **6**: 139–148.

[113] Jafari S, Bavand-Vandchali M, Mashhadi M, *et al*. Effects of HfB_2 addition on pressureless sintering behavior and microstructure of ZrB_2–SiC composites. *Int J Refract Met Hard Mater* 2021, **94**: 105371.

[114] Zhang GJ, Deng ZY, Kondo N, *et al*. Reactive hot pressing of ZrB_2–SiC composites. *J Am Ceram Soc* 2004, **83**: 2330–2332.

[115] Wu WW, Zhang GJ, Kan YM, *et al*. Reactive hot pressing of ZrB_2–SiC–ZrC ultra high-temperature ceramics at 1800 ℃. *J Am Ceram Soc* 2006, **89**: 2967–2969 .

[116] Zhao Y, Wang LJ, Zhang GJ, *et al*. Preparation and microstructure of a ZrB_2–SiC composite fabricated by the spark plasma sintering-reactive synthesis (SPS–RS) method. *J Am Ceram Soc* 2007, **90**: 4040–4042.

[117] Zhao H, He Y, Jin ZZ. Preparation of zirconium boride powder. *J Am Ceram Soc* 1995, **78**: 2534–2536.

[118] Kannan R, Rangaraj L. Densification, mechanical, and tribological properties of ZrB_2–ZrC_x composites produced by reactive hot pressing. *J Am Ceram Soc* 2020, **103**: 6120–6135.

[119] Zhang XH, Hu P, Du SY, *et al*. Research progress on ultra-high temperature ceramic composites. *Chin Sci Bull* 2015, **60**: 257–266.

[120] Kim S, Chae JM, Lee SM, *et al*. Change in microstructures and physical properties of ZrB_2–SiC ceramics hot-pressed with a variety of SiC sources. *Ceram Int* 2014, **40**: 3477–3483.

[121] Zhang SC, Hilmas GE, Fahrenholtz WG. Mechanical properties of sintered ZrB_2–SiC ceramics. *J Eur Ceram Soc* 2011, **31**: 893–901.

[122] Zhang XH, Qu Q, Han JC, *et al*. Microstructural features and mechanical properties of ZrB_2–SiC–ZrC composites fabricated by hot pressing and reactive hot pressing. *Scripta Mater* 2008, **59**: 753–756.

[123] Zhang XH, Xu L, Du SY, *et al*. Spark plasma sintering and hot pressing of ZrB_2–SiCW ultra-high temperature ceramics. *J Alloys Compd* 2008, **466**: 241–245.

[124] Wang Z, Hong CQ, Zhang XH, *et al*. Microstructure and thermal shock behavior of ZrB_2–SiC–graphite composite. *Mater Chem Phys* 2009, **113**: 338–341.

[125] Chen DJ, Li WJ, Zhang XH, *et al*. Microstructural feature and thermal shock behavior of hot-pressed ZrB_2–SiC–ZrO_2 composite. *Mater Chem Phys* 2009, **116**: 348–352.

[126] Guo QL, Li JG, Shen Q, *et al*. Toughening of ZrB_2–SiC ceramics with the microstructure ZrB_2/Zr–Al–C fibrous monolith. *Scripta Mater* 2012, **66**: 296–299.

[127] Zhou P, Hu P, Zhang XH, *et al*. Laminated ZrB_2–SiC ceramic with improved strength and toughness. *Scripta Mater* 2011, **64**: 276–279.

[128] Fahrenholtz WG, Hilmas GE, Chamberlain AL, *et al*. Processing and characterization of ZrB_2-based ultra-high temperature monolithic and fibrous monolithic ceramics. *J Mater Sci* 2004, **39**: 5951–5957.

[129] Hu P, Wang Z. Flexural strength and fracture behavior of ZrB_2–SiC ultra-high temperature ceramic composites at 1800 ℃. *J Eur Ceram Soc* 2010, **30**: 1021–1026.

[130] Zou J, Zhang GJ, Vleugels J, *et al*. High temperature strength of hot pressed ZrB_2–20 vol%SiC ceramics based on ZrB_2 starting powders prepared by different carbo/boro-thermal reduction routes. *J Eur Ceram Soc* 2013, **33**: 1609–1614.

[131] Zou J, Zhang GJ, Hu CF, *et al*. Strong ZrB_2–SiC–WC ceramics At 1600 ℃. *J Am Ceram Soc* 2012, **95**: 874–878.

[132] Zou J, Ma HB, D'Angio A, *et al*. Tungsten carbide: A versatile additive to get trace alkaline-earth oxide impurities out of ZrB_2 based ceramics. *Scripta Mater* 2018, **147**: 40–44.

[133] Ma HB, Zou J, Zhu JT, *et al*. Segregation of tungsten atoms at ZrB_2 grain boundaries in strong ZrB_2–SiC–WC ceramics. *Scripta Mater* 2018, **157**: 76–80.

[134] Hu DL, Gu H, Zou J, *et al*. Core–rim structure, bi-solubility and a hierarchical phase relationship in hot-pressed ZrB_2–SiC–MC ceramics (M = Nb, Hf, Ta, W). *J Materiomics* 2021, **7**: 69–79.

[135] Dai FZ, Zhou YC, Sun W. Segregation of solute atoms (Y, Nb, Ta, Mo and W) in ZrB_2 grain boundaries and their effects on grain boundary strengths: A first-principles investigation. *Acta Mater* 2017, **127**: 312–318.

[136] Dai FZ, Wen B, Xiang HM, *et al*. Grain boundary strengthening in ZrB_2 by segregation of W: Atomistic simulations with deep learning potential. *J Eur Ceram Soc* 2020, **40**: 5029–5036.

[137] Bellosi A, Monteverde F, Sciti D. Fast densification of ultra-high-temperature ceramics by spark plasma sintering. *Int J Appl Ceram Technol* 2006, **3**: 32–40.

[138] Li WG, Yang F, Fang DN. The temperature-dependent fracture strength model for ultra-high temperature ceramics. *Acta Mech Sin* 2010, **26**: 235–239.

[139] Wang RZ, Li WG, Ji BH, *et al*. Fracture strength of the particulate-reinforced ultra-high temperature ceramics based on a temperature dependent fracture toughness model. *J Mech Phys Solids* 2017, **107**: 365–378.

[140] Wang RZ, Li WG, Li DY, *et al*. A new temperature dependent fracture strength model for the ZrB_2–SiC composites. *J Eur Ceram Soc* 2015, **35**: 2957–2962.

[141] Wang Y, Liang J, Han WB, *et al*. Mechanical properties and thermal shock behavior of hot-pressed ZrB_2–SiC–AlN composites. *J Alloys Compd* 2009, **475**: 762–765.

[142] Hasselman DPH. Strength behavior of polycrystalline alumina subjected to thermal shock. *J Am Ceram Soc* 1970, **53**: 490–495.

[143] Hasselman DP. Thermal stress resistance parameters for brittle refractory ceramics: A compendium. *Am Ceram Soc Bull* 1970, **49**: 1033–1037.

[144] Zimmermann JW, Hilmas GE, Fahrenholtz WG. Thermal shock resistance and fracture behavior of ZrB_2-based fibrous monolith ceramics. *J Am Ceram Soc* 2009, **92**: 161–166.

[145] Ritchie RO. The conflicts between strength and toughness. *Nat Mater* 2011, **10**: 817–822.

[146] Zhao J, Xue JX, Liu HT, *et al*. ZrC ceramics incorporated with different-sized SiC particles. *Adv Appl Ceram* 2018, **117**: 383–388.

[147] Asl MS, Kakroudi MG, Noori S. Hardness and toughness of hot pressed ZrB_2–SiC composites consolidated under relatively low pressure. *J Alloys Compd* 2015, **619**: 481–487.

[148] Rezaie A, Fahrenholtz WG, Hilmas GE. Effect of hot pressing time and temperature on the microstructure and mechanical properties of ZrB_2–SiC. *J Mater Sci* 2007, **42**: 2735–2744.

[149] Yuan LJ, Zhang PJ, Zuo F, *et al*. Comparison of sintering behavior and reinforcing mechanisms between 3Y-TZP/$Al_2O_{3(w)}$ and 12Ce-TZP/$Al_2O_{3(w)}$ composites: Combined effects of lanthanide stabilizer and Al_2O_3 whisker length. *J Eur Ceram Soc* 2021, **41**: 706–718.

[150] Li JP, Meng SH, Wang ZB, *et al*. Study on ZrC–20 vol.%SiC_w ultrahigh temperature ceramics by hot pressing. *Adv Mater Res* 2012, **557–559**: 772–775.

[151] Zhang XH, Xu L, Du SY, *et al*. Fabrication and mechanical properties of ZrB_2–SiCw ceramic matrix composite. *Mater Lett* 2008, **62**: 1058–1060.

[152] Iijima S. Helical microtubules of graphitic carbon. *Nat* 1991, **354**: 56–58.

[153] Tian WB, Kan YM, Zhang GJ, *et al*. Effect of carbon nanotubes on the properties of ZrB_2–SiC ceramics. *Mater Sci Eng*: *A* 2008, **487**: 568–573.

[154] Lin J, Huang Y, Zhang H, *et al*. Microstructure and mechanical properties of multiwalled carbon nanotube toughened spark plasma sintered ZrB_2 composites. *Adv Appl Ceram* 2016, **115**: 308–312.

[155] Li L, Zhang D, Deng JP, *et al*. Review—Progress of research on the preparation of graphene oxide via electrochemical approaches. *J Electrochem Soc* 2020, **167**: 155519.

[156] Ocak BC, Yavas B, Akin I, *et al*. Spark plasma sintered ZrC–TiC–GNP composites: Solid solution formation and mechanical properties. *Ceram Int* 2018, **44**: 2336–2344.

[157] Cheng YH, Hu P, Zhou SB, *et al*. Using macroporous graphene networks to toughen ZrC–SiC ceramic. *J Eur Ceram Soc* 2018, **38**: 3752–3758.

[158] Rama Rao GA, Venugopal V. Kinetics and mechanism of the oxidation of ZrC. *J Alloys Compd* 1994, **206**: 237–242.

[159] Voitovich RF, Pugach ÉA. High-temperature oxidation of ZrC and HfC. *Sov Powder Metall Met Ceram* 1973, **12**: 916–921.

[160] Florez R, Crespillo ML, He XQ, *et al*. Early stage oxidation of ZrC under 10 MeV Au^{3+} ion-irradiation at 800 ℃. *Corros Sci* 2020, **169**: 108609.

[161] Zhang XH, Hu P, Meng SH, *et al*. Microstructure and mechanical properties of ZrB_2-based ceramics. *Key Eng Mater* 2006, **312**: 287–292.

[162] Hu P, Gui K, Yang Y, *et al*. Effect of SiC content on the ablation and oxidation behavior of ZrB_2-based ultra high temperature ceramic composites. *Materials*: *Basel* 2013, **6**: 1730–1744.

[163] Zhang DY, Hu P, Dong S, *et al*. Microstructures and mechanical properties of C_f/ZrB_2–SiC composite fabricated by nano slurry brushing combined with low-temperature hot pressing. *J Alloys Compd* 2019, **789**: 755–761.

[164] Fahrenholtz WG. Thermodynamic analysis of ZrB_2–SiC oxidation: Formation of a SiC-depleted region. *J Am Ceram Soc* 2007, **90**: 143–148.

[165] Darihaki F, Balak Z, Eatemadi R. Effect of nano and micro SiC particles on the microstructure and fracture toughness of ZrB_2–SiC nanocomposite produced by SPS method. *Mater Res Express* 2019, **6**: 095608.

[166] Zhao LY. Effect of SiC and LaB_6 on mechanical properties and oxidation resistance of ZrC ceramic. Ph.D. Thesis. Harbin (China): Harbin Institute of Technology, 2012. (in Chinese)

[167] He RJ, Zhang XH, Hu P, *et al*. Aqueous gelcasting of ZrB_2–SiC ultra high temperature ceramics. *Ceram Int* 2012, **38**: 5411–5418.

[168] Parthasarathy TA, Rapp RA, Opeka M, *et al*. A model for the oxidation of ZrB_2, HfB_2 and TiB_2. *Acta Mater* 2007, **55**: 5999–6010.

[169] Ping H, Wang GL, Zhi W. Oxidation mechanism and resistance of ZrB_2–SiC composites. *Corros Sci* 2009, **51**: 2724–2732.

[170] Zhang XH, Hu P, Han JC. Structure evolution of ZrB_2–SiC during the oxidation in air. *J Mater Res* 2008, **23**: 1961–1972.

[171] Han WB, Hu P, Zhang XH, *et al*. High-temperature oxidation at 1900 ℃ of $ZrB_{2-x}SiC$ ultrahigh-temperature ceramic composites. *J Am Ceram Soc* 2008, **91**: 3328–3334.

[172] Li Y, Yang X, Wang W, *et al*. Reaction behavior, microstructure, and radiative properties of *in situ* ZrB_2–SiC ceramic composites from a Si–Zr–B_4C system. *J Mater Eng Perform* 2020, **29**: 4822–4829.

[173] Ni DW, Zhang GJ, Xu FF, *et al*. Initial stage of oxidation process and microstructure analysis of HfB_2–20 vol.% SiC composite at 1500 ℃. *Scripta Mater* 2011, **64**: 617–620.

[174] Lu Y, Zou J, Xu FF, *et al*. Volatility diagram of ZrB_2–SiC–ZrC system and experimental validation. *J Am Ceram Soc* 2018, **101**: 3627–3635.

[175] Han JC, Hu P, Zhang XH, *et al*. Oxidation-resistant ZrB_2–SiC composites at 2200 ℃. *Compos Sci Technol* 2008, **68**: 799–806.

[176] Hu P, Zhang DY, Dong S, *et al*. A novel vibration-assisted slurry impregnation to fabricate C_f/ZrB_2–SiC composite with enhanced mechanical properties. *J Eur Ceram Soc* 2019, **39**: 798–805.

[177] Gui KX, Liu FY, Wang G, *et al*. Microstructural evolution and performance of carbon fiber-toughened ZrB_2 ceramics with SiC or $ZrSi_2$ additive. *J Adv Ceram* 2018, **7**: 343–351.

[178] Shojaie-Bahaabad M, Hasani-Arefi A. Ablation properties of ZrC–SiC–HfB_2 ceramic with different

amount of carbon fiber under an oxyacetylene flame. *Mater Res Express* 2020, **7**: 025604.

[179] Baharvandi HR, Mashayekh S. Effects of SiC content on the densification, microstructure, and mechanical properties of HfB_2–SiC composites. *Int J Appl Ceram Technol* 2020, **17**: 449–458.

[180] Simonenko EP, Simonenko NP, Gordeev AN, *et al*. The effects of subsonic and supersonic dissociated air flow on the surface of ultra-high-temperature HfB_2–30 vol% SiC ceramics obtained using the Sol-gel method. *J Eur Ceram Soc* 2020, **40**: 1093–1102.

[181] Weng L, Zhang XH, Han WB, *et al*. Fabrication and evaluation on thermal stability of hafnium diboride matrix composite at severe oxidation condition. *Int J Refract Met Hard Mater* 2009, **27**: 711–717.

[182] Monteverde F, Bellosi A. Microstructure and properties of an HfB_2–SiC composite for ultra high temperature applications. *Adv Eng Mater* 2004, **6**: 331–336.

[183] Zhang SC, Hilmas GE, Fahrenholtz WG. Oxidation of zirconium diboride with tungsten carbide additions. *J Am Ceram Soc* 2011, **94**: 1198–1205.

[184] Ni DW, Zhang GJ, Kan YM, *et al*. Textured HfB_2-based ultrahigh-temperature ceramics with anisotropic oxidation behavior. *Scripta Mater* 2009, **60**: 913–916.

[185] Ni DW, Zhang GJ, Kan YM, *et al*. Highly textured ZrB_2-based ultrahigh temperature ceramics via strong magnetic field alignment. *Scripta Mater* 2009, **60**: 615–618.

[186] Zhang GJ, Ni DW, Zou J, *et al*. Inherent anisotropy in transition metal diborides and microstructure/property tailoring in ultra-high temperature ceramics–A review. *J Eur Ceram Soc* 2018, **38**: 371–389.

[187] Liu HT, Zou J, Ni DW, *et al*. Anisotropy oxidation of textured ZrB_2–$MoSi_2$ ceramics. *J Eur Ceram Soc* 2012, **32**: 3469–3476.

[188] Li F, Kang Z, Huang X, *et al*. Fabrication of zirconium carbide nanofibers by electrospinning. *Ceram Int* 2014, **40**: 10137–10141.

[189] She J, Zhan YZ, Pang MJ, *et al*. *In situ* synthesized (ZrB_2+ZrC) hybrid short fibers reinforced Zr matrix composites for nuclear applications. *Int J Refract Met Hard Mater* 2011, **29**: 401–404.

[190] Ren JC, Zhang YL, Hu H, *et al*. Oxidation resistance and mechanical properties of HfC nanowire-toughened ultra-high temperature ceramic coating for SiC-coated C/C composites. *Appl Surf Sci* 2016, **360**: 970–978.

[191] Sciti D, Pienti L, Natali Murri A, *et al*. From random chopped to oriented continuous SiC fibers–ZrB_2 composites. *Mater Des* 2014, **63**: 464–470.

[192] Pienti L, Sciti D, Silvestroni L, *et al*. Effect of milling on the mechanical properties of chopped SiC fiber-reinforced ZrB_2. *Materials* 2013, **6**: 1980–1993.

[193] Sciti D, Guicciardi S, Silvestroni L. SiC chopped fibers reinforced ZrB_2: Effect of the sintering aid. *Scripta Mater* 2011, **64**: 769–772.

[194] Failla S, Galizia P, Zoli L, *et al*. Toughening effect of non-periodic fiber distribution on crack propagation energy of UHTC composites. *J Alloys Compd* 2019, **777**: 612–618.

[195] Chen SA, Hu HF, Zhang YD, *et al*. Effects of TaC amount on the properties of 2D C/SiC–TaC composites prepared via precursor infiltration and pyrolysis. *Mater Des* 2013, **51**: 19–24.

[196] Rubio V, Binner J, Cousinet S, *et al*. Materials characterisation and mechanical properties of C_f-UHTC powder composites. *J Eur Ceram Soc* 2019, **39**: 813–824.

[197] Rueschhoff LM, Carney CM, Apostolov ZD, *et al*. Processing of fiber-reinforced ultra-high temperature ceramic composites: A review. *Int J Ceram Eng Sci* 2020, **2**: 22–37.

[198] Chen BW, Ni DW, Liao CJ, *et al*. Long-term ablation behavior and mechanisms of 2D-C_f/ZrB_2–SiC composites at temperatures up to 2400 ℃. *Corros Sci* 2020, **177**: 108967.

[199] Zhou HJ, Yang JS, Le G, *et al*. Effect of ZrC amount and distribution on the thermomechanical properties of C_f/SiC–ZrC composites. *Int J Appl Ceram Technol* 2019, **16**: 1321–1328.

[200] Ding Q, Chen BW, Ni DW, *et al*. Improved ablation resistance of 3D-C_f/SiBCN composites with $(PyC/SiC)_3$ multi-layers as interphase. *J Eur Ceram Soc* 2021, **41**: 1114–1120.

[201] Xie J, Li KZ, Sun GD, *et al*. Effects of surface structure unit of 2D needled carbon fiber preform on the microstructure and ablation properties of C/C–ZrC–SiC composites. *Ceram Int* 2019, **45**: 11912–11919.

[202] Li QG, Dong SM, Wang Z, *et al*. Microstructures and mechanical properties of 3D 4-directional, C_f/ZrC–SiC composites using ZrC precursor and polycarbosilane. *Mater Sci Eng*: *B* 2013, **178**: 1186–1190.

[203] Ogasawara T, Aoki T, Hassan MSA, *et al*. Ablation behavior of SiC fiber/carbon matrix composites under simulated atmospheric reentry conditions. *Compos A*: *Appl Sci Manuf* 2011, **42**: 221–228.

[204] Zhu GX, Dong SM, Ni DW, *et al*. Microstructure, mechanical properties and oxidation resistance of SiC_f/SiC composites incorporated with boron nitride nanotubes. *RSC Adv* 2016, **6**: 83482–83492.

[205] Zhu GX, Dong SM, Hu JB, *et al*. *In situ* growth behavior of boron nitride nanotubes on the surface of silicon carbide fibers as hierarchical reinforcements. *RSC Adv* 2016, **6**: 14112–14119.

[206] Boitier G, Darzens S, Chermant JL, *et al*. Microstructural investigation of interfaces in CMCs. *Compos A*: *Appl Sci Manuf* 2002, **33**: 1467–1470.

[207] Kerans RJ, Hay RS, Parthasarathy TA, *et al*. Interface design for oxidation-resistant ceramic composites. *J Am Ceram Soc* 2002, **85**: 2599–2632.

[208] Yun HM, Dicarlo JA. Comparison of the tensile, creep, and rupture strength properties of stoichiometric SiC

fibers. Ustundag E, Fischman G, eds. In *23rd Annual Conference on Composites*, *Advanced Ceramics*, *Materials*, *and StructuresCeramic Engineering and Science Proceedings*, *Volume 20*. Westerville, OH, USA: 1999, 259–272.

[209] Ni DW, Wang JX, Dong SM, *et al*. Fabrication and properties of C_f/ZrC–SiC-based composites by an improved reactive melt infiltration. *J Am Ceram Soc* 2018, **101**: 3253–3258.

[210] Zeng Y, Wang DN, Xiong X, *et al*. Ablation-resistant carbide $Zr_{0.8}Ti_{0.2}C_{0.74}B_{0.26}$ for oxidizing environments up to 3,000 ℃. *Nat Commun* 2017, **8**: 15836.

[211] Zhang JP, Fu QG, Tong MD, *et al*. Microstructure, ablation behavior and thermal retardant ability of C/C–HfB_2 composites prepared by precursor infiltration pyrolysis combined with chemical vapor infiltration. *J Alloys Compd* 2018, **742**: 123–129.

[212] Yan CL, Liu RJ, Zhang CR, *et al*. Effects of SiC/HfC ratios on the ablation and mechanical properties of 3D C_f/HfC–SiC composites. *J Eur Ceram Soc* 2017, **37**: 2343–2351.

[213] Paul A, Binner J, Vaidhyanathan B. UHTC composites for hypersonic applications. In *Ultra-high Temperature Ceramics*. Hoboken, New Jersey, USA: John Wiley & Sons, 2014, 144–166.

[214] Chen ZK, Xiong X. Microstructure, mechanical properties and oxidation behavior of carbon fiber reinforced PyC/C–TaC/PyC layered-structure ceramic matrix composites prepared by chemical vapor infiltration. *Mater Chem Phys* 2013, **141**: 613–619.

[215] Pienti L, Sciti D, Silvestroni L, *et al*. Ablation tests on HfC- and TaC-based ceramics for aeropropulsive applications. *J Eur Ceram Soc* 2015, **35**: 1401–1411.

[216] Vinci A, Zoli L, Sciti D. Influence of SiC content on the oxidation of carbon fibre reinforced ZrB_2/SiC composites at 1500 and 1650 ℃ in air. *J Eur Ceram Soc* 2018, **38**: 3767–3776.

[217] Patra N, Al Nasiri N, Jayaseelan DD, *et al*. Thermal properties of C_f/HfC and C_f/HfC–SiC composites prepared by precursor infiltration and pyrolysis. *J Eur Ceram Soc* 2018, **38**: 2297–2303.

[218] Luo L, Liu JP, Duan LY, *et al*. Multiple ablation resistance of La_2O_3/Y_2O_3-doped C/SiC–ZrC composites. *Ceram Int* 2015, **41**: 12878–12886.

[219] Zeng Y, Wang DN, Xiong X, *et al*. Ultra-high-temperature ablation behavior of SiC–ZrC–TiC modified carbon/carbon composites fabricated via reactive melt infiltration. *J Eur Ceram Soc* 2020, **40**: 651–659.

[220] Pan XH, Niu YR, Xu XT, *et al*. Long time ablation behaviors of designed ZrC–SiC–TiC ternary coatings for environments above 2000 ℃. *Corros Sci* 2020, **170**: 108645.

[221] Ding Q, Ni DW, Ni N, *et al*. Thermal damage and microstructure evolution mechanisms of C_f/SiBCN composites during plasma ablation. *Corros Sci* 2020, **169**: 108621.

[222] Liang B, Yang ZH, Li YT, *et al*. Ablation behavior and mechanism of SiC_f/C_f/SiBCN ceramic composites with improved thermal shock resistance under oxyacetylene combustion flow. *Ceram Int* 2015, **41**: 8868–8877.

[223] Li DX, Yang ZH, Jia DC, *et al*. Ablation behavior of graphene reinforced SiBCN ceramics in an oxyacetylene combustion flame. *Corros Sci* 2015, **100**: 85–100.

[224] Wang JY, Duan XM, Yang ZH, *et al*. Ablation mechanism and properties of SiC_f/SiBCN ceramic composites under an oxyacetylene torch environment. *Corros Sci* 2014, **82**: 101–107.

[225] Rubio V, Ramanujam P, Binner J. Ultra-high temperature ceramic composite. *Adv Appl Ceram* 2018, **117**: s56–s61.

[226] Tang SF, Hu CL. Design, preparation and properties of carbon fiber reinforced ultra-high temperature ceramic composites for aerospace applications: A review. *J Mater Sci Technol* 2017, **33**: 117–130.

[227] Wang HD, Feng Q, Wang Z, *et al*. Microstructure evolution and high-temperature mechanical properties of SiC_f/SiC composites in liquid fluoride salt environment. *Corros Sci* 2017, **124**: 131–137.

[228] Baker B, Rubio V, Ramanujam P, *et al*. Development of a slurry injection technique for continuous fibre ultra-high temperature ceramic matrix composites. *J Eur Ceram Soc* 2019, **39**: 3927–3937.

[229] Servadei F, Zoli L, Galizia P, *et al*. Development of UHTCMCs via water based ZrB_2 powder slurry infiltration and polymer infiltration and pyrolysis. *J Eur Ceram Soc* 2020, **40**: 5076–5084.

[230] Yan CL, Liu RJ, Cao YB, *et al*. Fabrication and properties of PIP 3D C_f/ZrC–SiC composites. *Mater Sci Eng*: *A* 2014, **591**: 105–110.

[231] Yan CL, Liu RJ, Cao YB, *et al*. Preparation and properties of 3D needle-punched C/ZrC–SiC composites by polymer infiltration and pyrolysis process. *Ceram Int* 2014, **40**: 10961–10970.

[232] Duan LY, Luo L, Liu LP, *et al*. Ablation of C/SiC–HfC composite prepared by precursor infiltration and pyrolysis in plasma wind tunnel. *J Adv Ceram* 2020, **9**: 393–402.

[233] Wang Z, Dong SM, Zhang XY, *et al*. Fabrication and properties of C_f/SiC–ZrC composites. *J Am Ceram Soc* 2008, **91**: 3434–3436.

[234] Chen SA, Zhang YD, Zhang CR, *et al*. Effects of SiC interphase by chemical vapor deposition on the properties of C/ZrC composite prepared via precursor infiltration and pyrolysis route. *Mater Des* 2013, **46**: 497–502.

[235] Li QG, Dong SM, Wang Z, *et al*. Fabrication and properties of 3-D C_f/ZrB_2–ZrC–SiC composites via polymer infiltration and pyrolysis. *Ceram Int* 2013, **39**: 5937–5941.

[236] Zhang MY, Li KZ, Shi XH, *et al*. Effects of SiC interphase on the mechanical and ablation properties of C/C–ZrC–ZrB_2–SiC composites prepared by precursor infiltration and pyrolysis. *Mater Des* 2017, **122**: 322–329.

[237] Hu P, Cheng Y, Zhang DY, *et al*. From ferroconcrete to

C_f/UHTC–SiC: A totally novel densification method and mechanism at 1300 ℃ without pressure. *Compos B*: *Eng* 2019, **174**: 107023.

[238] Zou LH, Wali N, Yang JM, *et al*. Microstructural development of a C_f/ZrC composite manufactured by reactive melt infiltration. *J Eur Ceram Soc* 2010, **30**: 1527–1535.

[239] Chen BW, Ni DW, Wang JX, *et al*. Ablation behavior of C_f/ZrC–SiC-based composites fabricated by an improved reactive melt infiltration. *J Eur Ceram Soc* 2019, **39**: 4617–4624.

[240] Zhao ZG, Li KZ, Li W, *et al*. Ablation behavior of C/C–ZrC–SiC composites prepared by reactive melt infiltration under oxyacetylene torch at two heat fluxes. *Ceram Int* 2018, **44**: 17345–17358.

[241] Wing BL, Halloran JW. Microstress in the matrix of a melt-infiltrated SiC/SiC ceramic matrix composite. *J Am Ceram Soc* 2017, **100**: 5286–5294.

[242] Tong YG, Bai SX, Chen K. C/C–ZrC composite prepared by chemical vapor infiltration combined with alloyed reactive melt infiltration. *Ceram Int* 2012, **38**: 5723–5730.

[243] Chen XW, Feng Q, Gao L, *et al*. Interphase degradation of three-dimensional C_f/SiC–ZrC–ZrB_2 composites fabricated via reactive melt infiltration. *J Am Ceram Soc* 2017, **100**: 4816–4826.

[244] Vinci A, Zoli L, Galizia P, *et al*. Reactive melt infiltration of carbon fibre reinforced ZrB_2/B composites with Zr_2Cu. *Compos A*: *Appl Sci Manuf* 2020, **137**: 105973.

[245] Levenspiel O. *Ingeniería de las Reacciones Químicas*. 2nd edn. Barcelona: Wiley, 1990. (in Spanish)

[246] Chen XW, Feng Q, Kan YM, *et al*. Effects of preform pore structure on infiltration kinetics and microstructure evolution of RMI-derived C_f/ZrC–ZrB_2–SiC composite. *J Eur Ceram Soc* 2020, **40**: 2683–2690.

[247] Li L, Qiao HW, Li QG, *et al*. *In situ* fabrication and characterization of laminated C/ZrC ceramic via filter papers and zirconia powders. *Ceram Int* 2017, **43**: 5607–5615.

[248] Zoli L, Vinci A, Silvestroni L, *et al*. Rapid spark plasma sintering to produce dense UHTCs reinforced with undamaged carbon fibres. *Mater Des* 2017, **130**: 1–7.

[249] Zoli L, Sciti D. Efficacy of a ZrB_2–SiC matrix in protecting C fibres from oxidation in novel UHTCMC materials. *Mater Des* 2017, **113**: 207–213.

[250] Zoli L, Vinci A, Galizia P, *et al*. Is spark plasma sintering suitable for the densification of continuous carbon fibre-UHTCMCs? *J Eur Ceram Soc* 2020, **40**: 2597–2603.

[251] Yao JJ, Pang SY, Hu CL, *et al*. Mechanical, oxidation and ablation properties of C/(C–SiC)CVI-(ZrC–SiC)PIP composites. *Corros Sci* 2020, **162**: 108200.

[252] Zhang DY, Hu P, Feng JX, *et al*. Characterization and mechanical properties of C_f/ZrB_2–SiC composites fabricated by a hybrid technique based on slurry impregnation, polymer infiltration and pyrolysis and low-temperature hot pressing. *Ceram Int* 2019, **45**: 5467–5474.

[253] Zhang DY, Hu P, Dong S, *et al*. Oxidation behavior and ablation mechanism of C_f/ZrB_2–SiC composite fabricated by vibration-assisted slurry impregnation combined with low-temperature hot pressing. *Corros Sci* 2019, **161**: 108181.

[254] Wang YG, Liu W, Cheng LF, *et al*. Preparation and properties of 2D C/ZrB_2–SiC ultra high temperature ceramic composites. *Mater Sci Eng*: *A* 2009, **524**: 129–133.

[255] Ouyang HB, Zhang YL, Li CY, *et al*. Effects of ZrC/SiC ratios on mechanical and ablation behavior of C/C–ZrC–SiC composites prepared by carbothermal reaction of hydrothermal co-deposited oxides. *Corros Sci* 2020, **163**: 108239.

[256] Yan CL, Liu RJ, Zhang CR, *et al*. Effect of PyC interphase thickness on mechanical and ablation properties of 3D C_f/ZrC–SiC composite. *Ceram Int* 2016, **42**: 12756–12762.

[257] Li QG, Dong SM, Wang Z, *et al*. Fabrication and properties of 3-D C_f/SiC–ZrC composites, using ZrC precursor and polycarbosilane. *J Am Ceram Soc* 2012, **95**: 1216–1219.

[258] Li HJ, He QC, Wang CC, *et al*. Effects of precursor feeding rate on the microstructure and ablation resistance of gradient C/C–ZrC–SiC composites prepared by chemical liquid-vapor deposition. *Vacuum* 2019, **164**: 265–277.

[259] Chen BW, Ni DW, Lu J, *et al*. Multi-cycle and long-term ablation behavior of C_f/ZrB_2–SiC composites at 2500 ℃. *Corros Sci* 2021, **184**: 109385.

[260] Wu XW, Su ZA, Huang QZ, *et al*. Effect of ZrC particle distribution on the ablation resistance of C/C–SiC–ZrC composites fabricated using precursor infiltration pyrolysis. *Ceram Int* 2020, **46**: 16062–16067.

[261] Wang Z, Dong SM, Ding YS, *et al*. Mechanical properties and microstructures of C_f/SiC–ZrC composites using T700SC carbon fibers as reinforcements. *Ceram Int* 2011, **37**: 695–700.

[262] Kannan R, Rangaraj L. Properties of C_f/SiC–ZrB_2–Ta_xCy composite produced by reactive hot pressing and polymer impregnation pyrolysis (RHP/PIP). *J Eur Ceram Soc* 2019, **39**: 2257–2265.

[263] Jia Y, Chen SA, Li Y, *et al*. High-temperature mechanical properties and microstructure of C/C–ZrC–SiC–ZrB_2 composites prepared by a joint process of precursor infiltration and pyrolysis and slurry infiltration. *J Alloys Compd* 2019, **811**: 151953.

[264] Sciti D, Zoli L, Vinci A, *et al*. Effect of PAN-based and pitch-based carbon fibres on microstructure and properties of continuous C_f/ZrB_2–SiC UHTCMCs. *J Eur Ceram Soc* 2021, **41**: 3045–3050.

[265] Vinci A, Zoli L, Sciti D, *et al*. Mechanical behaviour of carbon fibre reinforced TaC/SiC and ZrC/SiC composites

up to 2100 ℃. *J Eur Ceram Soc* 2019, **39**: 780–787.
[266] Silvestroni L, Pienti L, Guicciardi S, *et al*. Strength and toughness: The challenging case of TaC-based composites. *Compos B*: *Eng* 2015, **72**: 10–20.
[267] Gui KX, Hu P, Hong WH, *et al*. Microstructure, mechanical properties and thermal shock resistance of ZrB_2–SiC–C_f composite with inhibited degradation of carbon fibers. *J Alloys Compd* 2017, **706**: 16–23.
[268] Hu P, Cheng Y, Xie MS, *et al*. Damage mechanism analysis to the carbon fiber and fiber-ceramic interface tailoring of C_f/ZrC–SiC using PyC coating. *Ceram Int* 2018, **44**: 19038–19043.
[269] Hu CL, Pang SY, Tang SF, *et al*. An integrated composite with a porous C_f/C–ZrB_2–SiC core between two compact outer layers of C_f/C–ZrB_2–SiC and C_f/C–SiC. *J Eur Ceram Soc* 2015, **35**: 1113–1117.
[270] Hu CL, Pang SY, Tang SF, *et al*. Ablation and mechanical behavior of a sandwich-structured composite with an inner layer of C_f/SiC between two outer layers of C_f/SiC–ZrB_2–ZrC. *Corros Sci* 2014, **80**: 154–163.
[271] Chen XW, Dong SM, Kan YM, *et al*. Microstructure and mechanical properties of three dimensional C_f/SiC–ZrC–ZrB_2 composites prepared by reactive melt infiltration method. *J Eur Ceram Soc* 2016, **36**: 3969–3976.
[272] Chen SA, Ji HL, Li Y, *et al*. Effects of high-temperature annealing on the microstructure and properties of C/ZrC composites prepared by reactive melt infiltration. *Mater Sci Eng*: *A* 2017, **686**: 41–45.
[273] Chen SA, Zhang CR, Zhang YD, *et al*. Effects of polymer derived SiC interphase on the properties of C/ZrC composites. *Mater Des* 2014, **58**: 102–107.
[274] Das J, Kesava BC, Reddy JJ, *et al*. Microstructure, mechanical properties and oxidation behavior of short carbon fiber reinforced ZrB_2–20v/oSiC–2v/oB_4C composite. *Mater Sci Eng*: *A* 2018, **719**: 206–226.
[275] Vinci A, Zoli L, Landi E, *et al*. Oxidation behaviour of a continuous carbon fibre reinforced ZrB_2–SiC composite. *Corros Sci* 2017, **123**: 129–138.
[276] Vinci A, Zoli L, Galizia P, *et al*. Influence of Y_2O_3 addition on the mechanical and oxidation behaviour of carbon fibre reinforced ZrB_2/SiC composites. *J Eur Ceram Soc* 2020, **40**: 5067–5075.
[277] Guo SQ. Oxidation and strength retention of HfB_2−SiC composite with La_2O_3 additives. *Adv Appl Ceram* 2020, **119**: 218–223.
[278] Chen ZK, Wu Y, Chen YH, *et al*. Preparation and oxidation behavior of C_f/C–TaC composites. *Mater Chem Phys* 2020, **254**: 123428.
[279] Mungiguerra S, di Martino GD, Cecere A, *et al*. Arc-jet wind tunnel characterization of ultra-high-temperature ceramic matrix composites. *Corros Sci* 2019, **149**: 18–28.
[280] Ni C, Li KZ, Liu L, *et al*. Ablation mechanism of SiC coated C/C composites at 0° angle in two flame conditions under an oxyacetylene flame. *Corros Sci* 2014, **84**: 1–10.
[281] Ma Y, Li QG, Dong SM, *et al*. Microstructures and ablation properties of 3D 4-directional Cf/ZrC–SiC composite in a plasma wind tunnel environment. *Ceram Int* 2014, **40**: 11387–11392.
[282] Tang SF, Deng JY, Wang SJ, *et al*. Comparison of thermal and ablation behaviors of C/SiC composites and C/ZrB_2–SiC composites. *Corros Sci* 2009, **51**: 54–61.
[283] Tong YG, Hu YL, Liang XB, *et al*. Carbon fiber reinforced ZrC based ultra-high temperature ceramic matrix composite subjected to laser ablation: Ablation resistance, microstructure and damage mechanism. *Ceram Int* 2020, **46**: 14408–14415.
[284] Zhou HJ, Ni DW, He P, *et al*. Ablation behavior of C/C–ZrC and C/SiC–ZrC composites fabricated by a joint process of slurry impregnation and chemical vapor infiltration. *Ceram Int* 2018, **44**: 4777–4782.
[285] Li QG, Dong SM, Wang Z, *et al*. Ablation behavior and mechanism of 3D C_f/ZrC–SiC composites in a plasma wind tunnel environment. *J Asian Ceram Soc* 2015, **3**: 377–382.
[286] Yan CL, Liu RJ, Zhang CR, *et al*. Ablation and mechanical properties of 3D braided C/ZrC–SiC composites with various SiC/ZrC ratios. *Ceram Int* 2016, **42**: 19019–19026.
[287] Tang SF, Deng JY, Wang SJ, *et al*. Ablation behaviors of ultra-high temperature ceramic composites. *Mater Sci Eng*: *A* 2007, **465**: 1–7.
[288] Paul A, Venugopal S, Binner JGP, *et al*. UHTC–carbon fibre composites: Preparation, oxyacetylene torch testing and characterisation. *J Eur Ceram Soc* 2013, **33**: 423–432.
[289] Zhou YC, Xiang HM, Feng ZH, *et al*. Electronic structure and mechanical properties of NiB: A promising interphase material for future UHTC_f/UHTC composites. *J Am Ceram Soc* 2016, **99**: 2110–2119.
[290] Zhou YC, Wang XF, Xiang HM, *et al*. Theoretical prediction, preparation, and mechanical properties of YbB_6, a candidate interphase material for future UHTC_f/UHTC composites. *J Eur Ceram Soc* 2016, **36**: 3571–3579.
[291] Jayaseelan DD, Zapata-Solvas E, Brown P, *et al*. *In situ* formation of oxidation resistant refractory coatings on SiC-reinforced ZrB_2 ultra high temperature ceramics. *J Am Ceram Soc* 2012, **95**: 1247–1254.
[292] Wang P, Zhou CL, Zhang XH, *et al*. Oxidation protective ZrB_2–SiC coatings with ferrocene addition on SiC coated graphite. *Ceram Int* 2016, **42**: 2654–2661.
[293] Zhang YL, Hu H, Zhang PF, *et al*. SiC/ZrB_2–SiC–ZrC multilayer coating for carbon/carbon composites against ablation. *Surf Coat Technol* 2016, **300**: 1–9.
[294] Ren XR, Li HJ, Fu QG, *et al*. Oxidation protective TaB_2–SiC gradient coating to protect SiC–Si coated carbon/carbon composites against oxidation. *Compos B*: *Eng* 2014, **66**: 174–179.
[295] Wang P, Zhou SB, Hu P, *et al*. Ablation resistance of ZrB_2–SiC/SiC coating prepared by pack cementation for graphite. *J Alloys Compd* 2016, **682**: 203–207.

[296] Zhang JP, Fu QG. The effects of carbon/carbon composites blasting treatment and modifying SiC coatings with SiC/ZrB_2 on their oxidation and cyclic ablation performances. *Corros Sci* 2018, **140**: 134–142.

[297] Zhang JP, Fu QG, Wang YJ. Interface design and HfC additive to enhance the cyclic ablation performance of SiC coating for carbon/carbon composites from 1750 ℃ to room temperature under vertical oxyacetylene torch. *Corros Sci* 2017, **123**: 139–146.

[298] Zhou L, Fu QG, Hu D, *et al*. Oxidation protective SiC–Si coating for carbon/carbon composites by gaseous silicon infiltration and pack cementation: A comparative investigation. *J Eur Ceram Soc* 2021, **41**: 194–203.

[299] Zou X, Fu QG, Liu L, *et al*. ZrB_2-SiC coating to protect carbon/carbon composites against ablation. *Surf Coat Technol* 2013, **226**: 17–21.

[300] Allemand A, Szwedek O, Epherre J F, *et al.* Procédé pour revêtir une pièce d'un revêtement de protection contre l'oxydation par une technique de dépôt chimique en phase vapeur, et revêtement et pièce. EP patent 2782886, Oct. 2014.

[301] Chen ZK, Xiong X, Li GD, *et al*. Ablation behaviors of carbon/carbon composites with C–SiC–TaC multi-interlayers. *Appl Surf Sci* 2009, **255**: 9217–9223.

[302] Li ZH, Wang YL, Xiong X, *et al*. Microstructure and growth behavior of Hf(Ta)C ceramic coating synthesized by low pressure chemical vapor deposition. *J Alloys Compd* 2017, **705**: 79–88.

[303] Ren JC, Feng ER, Zhang YL, *et al*. Microstructure and anti-ablation performance of HfC–TaC and HfC–ZrC coatings synthesized by CVD on C/C composites. *Ceram Int* 2020, **46**: 10147–10158.

[304] Tong MD, Fu QG, Zhou L, *et al*. Ablation behavior of a novel HfC–SiC gradient coating fabricated by a facile one-step chemical vapor co-deposition. *J Eur Ceram Soc* 2018, **38**: 4346–4355.

[305] Verdon C, Szwedek O, Jacques S, *et al*. Hafnium and silicon carbide multilayer coatings for the protection of carbon composites. *Surf Coat Technol* 2013, **230**: 124–129.

[306] Wang YJ, Li HJ, Fu QG, *et al*. SiC/HfC/SiC ablation resistant coating for carbon/carbon composites. *Surf Coat Technol* 2012, **206**: 3883–3887.

[307] Wang YL, Li ZH, Xiong X, *et al*. Action mechanism of hydrogen gas on deposition of HfC coating using $HfCl_4$–CH_4–H_2–Ar system. *Appl Surf Sci* 2016, **390**: 903–908.

[308] Wang YL, Xiong X, Li GD, *et al*. Preparation and ablation properties of Hf(Ta)C co-deposition coating for carbon/carbon composites. *Corros Sci* 2013, **66**: 177–182.

[309] Zhang J, Zhang YL, Fu YQ, *et al*. Ablation behavior of HfC coating with different thickness for carbon/carbon composites at ultra-high temperature. *J Eur Ceram Soc* 2021, **41**: 1769–1778.

[310] Zhu Y, Cheng LF, Li MX, *et al*. The synthesis and characterization of CVD ZrB_2 coating from $ZrCl_4$–BCl_3–H_2–Ar system. *Ceram Int* 2018, **44**: 2002–2010.

[311] Lee HG, Kim D, Park JY, *et al*. Microstructure of SiC–ZrC composite coatings on TRISO particles via fluidized bed chemical vapor deposition. *Ceram Int* 2019, **45**: 24001–24006.

[312] Liu T, Niu YR, Li C, *et al*. Effect of $MoSi_2$ addition on ablation behavior of ZrC coating fabricated by vacuum plasma spray. *Ceram Int* 2018, **44**: 8946–8954.

[313] Torabi S, Valefi Z, Ehsani N. Ablation behavior of SiC/ZrB_2 ultra-high temperature ceramic coatings by solid shielding shrouded plasma spray for high-temperature applications (temperature above 2000 ℃). *Surf Coat Technol* 2020, **403**: 126271.

[314] Tan W, Adducci M, Trice R. Evaluation of rare-earth modified ZrB_2–SiC ablation resistance using an oxyacetylene torch. *J Am Ceram Soc* 2014, **97**: 2639–2645.

[315] Xu XT, Pan XH, Niu YR, *et al*. Difference evaluation on ablation behaviors of ZrC-based and ZrB_2-based UHTCs coatings. *Corros Sci* 2021, **180**: 109181.

[316] Yoo HI, Kim HS, Hong BG, *et al*. Hafnium carbide protective layer coatings on carbon/carbon composites deposited with a vacuum plasma spray coating method. *J Eur Ceram Soc* 2016, **36**: 1581–1587.

[317] Richet N, Lespade P, Goursat P, *et al*. Oxidation resistance of HfB_2–SiC coatings for protection of carbon fiber based composites. *Key Eng Mater* 2004, **264–268**: 1047–1050.

[318] Wang TY, Luo RY. Oxidation protection and mechanism of the HfB_2–SiC–Si/SiC coatings modified by *in situ* strengthening of SiC whiskers for C/C composites. *Ceram Int* 2018, **44**: 12370–12380.

[319] Zapata-Solvas E, Gómez-García D, Domínguez-Rodríguez A, *et al*. High temperature creep of 20 vol%. SiC–HfB_2 UHTCs up to 2000 ℃ and the effect of La_2O_3 addition. *J Eur Ceram Soc* 2018, **38**: 47–56.

[320] Zhang ML, Ren XR, Chu H, *et al*. Oxidation inhibition behaviors of the HfB_2–SiC–$TaSi_2$ coating for carbon structural materials at 1700 ℃. *Corros Sci* 2020, **177**: 108982.

[321] Zhang YL, Wang HH, Li T, *et al*. Ultra-high temperature ceramic coating for carbon/carbon composites against ablation above 2000 K. *Ceram Int* 2018, **44**: 3056–3063.

[322] Jiang Y, Liu WL, Wang N, *et al*. Multiphase composite $Hf_{0.8}Ti_{0.2}B_2$–SiC–Si coating providing oxidation and ablation protection for graphite under different high temperature oxygen-containing environments. *Ceram Int* 2021, **47**: 1903–1916.

[323] Ren Y, Qian YH, Xu JJ, *et al*. Oxidation and cracking/spallation resistance of ZrB_2–SiC–$TaSi_2$–Si coating on siliconized graphite at 1500 ℃ in air. *Ceram Int* 2020, **46**: 6254–6261.

[324] Zhang P, Fu QG, Cheng CY, *et al*. Comparing oxidation behaviors at 1773 K and 1973 K of HfB_2–$MoSi_2$/SiC–Si coating prepared by a combination method of pack cementation, slurry painting and *in situ* synthesis. *Surf*

Coat Technol 2020, **403**: 126418.

[325] Jiang Y, Liu T, Ru HQ, *et al*. Oxidation and ablation protection of multiphase $Hf_{0.5}Ta_{0.5}B_2$–SiC–Si coating for graphite prepared by dipping-pyrolysis and reactive infiltration of gaseous silicon. *Appl Surf Sci* 2018, **459**: 527–536.

[326] Zhang P, Fu QG, Hu D, *et al*. Oxidation behavior of SiC–HfB_2–Si coating on C/C composites prepared by slurry dipping combined with gaseous Si infiltration. *Surf Coat Technol* 2020, **385**: 125335.

[327] Zhuang L, Fu QG, Li HJ. SiCnw/PyC core–shell networks to improve the bonding strength and oxyacetylene ablation resistance of ZrB_2–ZrC coating for C/C–ZrB_2–ZrC–SiC composites. *Carbon* 2017, **124**: 675–684.

[328] Nisar A, Ariharan S, Venkateswaran T, *et al*. Effect of carbon nanotube on processing, microstructural, mechanical and ablation behavior of ZrB_2–20SiC based ultra-high temperature ceramic composites. *Carbon* 2017, **111**: 269–282.

[329] Zapata-Solvas E, Jayaseelan DD, Brown PM, *et al*. Thermal properties of La_2O_3-doped ZrB_2- and HfB_2-based ultra-high temperature ceramics. *J Eur Ceram Soc* 2013, **33**: 3467–3472.

[330] Zhang XH, Hu P, Han JC, *et al*. Ablation behavior of ZrB_2–SiC ultra high temperature ceramics under simulated atmospheric re-entry conditions. *Compos Sci Technol* 2008, **68**: 1718–1726.

[331] Brenner AE, Peña AA, Phuah XL, *et al*. Cyclic ablation of high-emissivity Sm-doped ZrB_2/SiC coatings on alumina substrates. *J Eur Ceram Soc* 2018, **38**: 1136–1142.

[332] Cheng CY, Li HJ, Fu QG, *et al*. A SiCnw/PyC-toughened ZrB_2–SiC coating for protecting Si–SiC coated C/C composites against oxidation. *Appl Surf Sci* 2018, **457**: 360–366.

[333] Chinnaraj RK, Hong SM, Kim HS, *et al*. Ablation experiments of ultra-high-temperature ceramic coating on carbon–carbon composite using ICP plasma wind tunnel. *Int J Aeronaut Space Sci* 2020, **21**: 889–905.

[334] Cui YH, Guo MY, Shao YX, *et al*. Effects of SiC on microstructure and properties of plasma sprayed ZrB_2–ZrC composite coating. *Ceram Int* 2021, **47**: 12753–12761.

[335] Hu D, Fu QG, Liu T, *et al*. Structural design and ablation performance of ZrB_2/$MoSi_2$ laminated coating for SiC coated carbon/carbon composites. *J Eur Ceram Soc* 2020, **40**: 212–219.

[336] Hu CL, Tang SF, Pang SY, *et al*. Long-term oxidation behaviors of C/SiC composites with a SiC/UHTC/SiC three-layer coating in a wide temperature range. *Corros Sci* 2019, **147**: 1–8.

[337] Jia YJ, Li HJ, Yao XY, *et al*. Long-time ablation protection of carbon/carbon composites with different-La_2O_3-content modified ZrC coating. *J Eur Ceram Soc* 2018, **38**: 1046–1058.

[338] Wang YJ, Li HJ, Fu QG, *et al*. Ablation behaviour of a TaC coating on SiC coated C/C composites at different temperatures. *Ceram Int* 2013, **39**: 359–365.

[339] Xu JJ, Sun W, Xu YL, *et al*. Microstructures and ablation resistance of WSi_2/$ZrSi_2$/$Zr_xHf_{1-x}C$/SiC coating based on a pattern strengthening one-step method. *J Eur Ceram Soc* 2021, **41**: 38–53.

[340] Information on https://Ultramet.Com/Chemical-Vapor-Deposition/#Materials-Deposited-Cvd.

[341] Kuriakose AK, Margrave JL. The oxidation kinetics of zirconium diboride and zirconium carbide at high temperatures. *J Electrochem Soc* 1964, **111**: 827.

[342] Wang PP, Li HJ, Ren XR, *et al*. HfB_2–SiC–$MoSi_2$ oxidation resistance coating fabricated through *in situ* synthesis for SiC coated C/C composites. *J Alloys Compd* 2017, **722**: 69–76.

[343] Cai ZY, Zhang DX, Chen XX, *et al*. A novel ultra-high-temperature oxidation protective $MoSi_2$–$TaSi_2$ ceramic coating for tantalum substrate. *J Eur Ceram Soc* 2019, **39**: 2277–2286..

[344] Tului M, Lionetti S, Pulci G, *et al*. Effects of heat treatments on oxidation resistance and mechanical properties of ultra high temperature ceramic coatings. *Surf Coat Technol* 2008, **202**: 4394–4398.

[345] Xu YL, Sun W, Xiong X, *et al*. Ablation characteristics of mosaic structure ZrC–SiC coatings on low-density, porous C/C composites. *J Mater Sci Technol* 2019, **35**: 2785–2798.

[346] Tan ZY, Zhu W, Yang L, *et al*. Microstructure, mechanical properties and ablation behavior of ultra-high-temperature Ta–Hf–C solid solution coating prepared by a step-by-step plasma solid solution method. *Surf Coat Technol* 2020, **403**: 126405.

[347] Zhang JP, Fu QG, Qu JL, *et al*. Surface modification of carbon/carbon composites and *in situ* grown SiC nanowires to enhance the thermal cycling performance of Si–Mo–Cr coating under parallel oxyacetylene torch. *Corros Sci* 2016, **111**: 667–674.

[348] Xiang Y, Li W, Wang S, *et al*. Preparation of UHTC based coatings for C–SiC composites by slurry and CVD. *Mater Technol* 2012, **27**: 257–260.

[349] Xu L, Cheng J, Li XC, *et al*. Preparation of carbon/carbon-ultra high temperature ceramics composites with ultra high temperature ceramics coating. *J Am Ceram Soc* 2018, **101**: 3830–3836.

[350] Loehman RE, Corral EL. Multilayer ultra-high-temperature ceramic coatings. U.S. patent 8 137 802, 2012.

[351] Zhou HJ, Gao L, Wang Z, *et al*. ZrB_2–SiC oxidation protective coating on C/C composites prepared by vapor silicon infiltration process. *J Am Ceram Soc* 2010, **93**: 915–919.

[352] Fu QG, Li HJ, Li KZ, *et al*. SiC whisker-toughened $MoSi_2$–SiC–Si coating to protect carbon/carbon composites against oxidation. *Carbon* 2006, **44**: 1866–1869.

[353] Ren JC, Zhang YL, Zhang PF, *et al*. UHTC coating reinforced by HfC nanowires against ablation for C/C composites. *Surf Coat Technol* 2017, **311**: 191–198.

[354] Cheng CY, Li HJ, Fu QG, *et al*. Effects of pyrocarbon on morphology stability of SiC nanowires at high temperatures. *J Am Ceram Soc* 2018, **101**: 3694–3702.

[355] Zhuang L, Fu QG, Ma WH, *et al*. Oxidation protection of C/C composites: Coating development with thermally stabile SiC@PyC nanowires and an interlocking TaB_2–SiC structure. *Corros Sci* 2019, **148**: 307–316.

[356] Vogel W. *Glass Chemistry*. Berlin: Springer-Verlag, Berlin Heidelberg, 1994.

[357] Atkins P, Paula J. *Atkins' Physical Chemistry.* Oxford: Oxford University Press, 2006: 783–827.

[358] George EP, Raabe D, Ritchie RO. High-entropy alloys. *Nat Rev Mater* 2019, **4**: 515–534.

[359] Xiang HM, Xing Y, Dai FZ, *et al*. High-entropy ceramics: Present status, challenges, and a look forward. *J Adv Ceram* 2021, **10**: 385–441.

[360] Rost CM, Sachet E, Borman T, *et al*. Entropy-stabilized oxides. *Nat Commun* 2015, **6**: 8485.

[361] Wright AJ, Wang QY, Huang CY, *et al*. From high-entropy ceramics to compositionally-complex ceramics: A case study of fluorite oxides. *J Eur Ceram Soc* 2020, **40**: 2120–2129.

[362] Gild J, Zhang YY, Harrington T, *et al*. High-entropy metal diborides: A new class of high-entropy materials and a new type of ultrahigh temperature ceramics. *Sci Rep* 2016, **6**: 37946.

[363] Zhang Y, Guo WM, Jiang ZB, *et al*. Dense high-entropy boride ceramics with ultra-high hardness. *Scripta Mater* 2019, **164**: 135–139.

[364] Shen XQ, Liu JX, Li F, *et al*. Preparation and characterization of diboride-based high entropy $(Ti_{0.2}Zr_{0.2}Hf_{0.2}Nb_{0.2}Ta_{0.2})B_2$–SiC particulate composites. *Ceram Int* 2019, **45**: 24508–24514.

[365] Gu JF, Zou J, Sun SK, *et al*. Dense and pure high-entropy metal diboride ceramics sintered from self-synthesized powders via boro/carbothermal reduction approach. *Sci China Mater* 2019, **62**: 1898–1909.

[366] Failla S, Galizia P, Fu S, *et al*. Formation of high entropy metal diborides using arc-melting and combinatorial approach to study quinary and quaternary solid solutions. *J Eur Ceram Soc* 2020, **40**: 588–593.

[367] Chen H, Xiang HM, Dai FZ, *et al*. Porous high entropy $(Zr_{0.2}Hf_{0.2}Ti_{0.2}Nb_{0.2}Ta_{0.2})B_2$: A novel strategy towards making ultrahigh temperature ceramics thermal insulating. *J Mater Sci Technol* 2019, **35**: 2404–2408.

[368] Liu JX, Shen XQ, Wu Y, *et al*. Mechanical properties of hot-pressed high-entropy diboride-based ceramics. *J Adv Ceram* 2020, **9**: 503–510.

[369] Sarker P, Harrington T, Toher C, *et al*. High-entropy high-hardness metal carbides discovered by entropy descriptors. *Nat Commun* 2018, **9**: 4980.

[370] Castle E, Csanádi T, Grasso S, *et al*. Processing and properties of high-entropy ultra-high temperature carbides. *Sci Rep* 2018, **8**: 8609.

[371] Wei XF, Liu JX, Li F, *et al*. High entropy carbide ceramics from different starting materials. *J Eur Ceram Soc* 2019, **39**: 2989–2994.

[372] Lu K, Liu JX, Wei XF, *et al*. Microstructures and mechanical properties of high-entropy $(Ti_{0.2}Zr_{0.2}Hf_{0.2}Nb_{0.2}Ta_{0.2})C$ ceramics with the addition of SiC secondary phase. *J Eur Ceram Soc* 2020, **40**: 1839–1847.

[373] Qin Y, Liu JX, Li F, *et al*. A high entropy silicide by reactive spark plasma sintering. *J Adv Ceram* 2019, **8**: 148–152.

[374] Gild J, Braun J, Kaufmann K, *et al*. A high-entropy silicide: $(Mo_{0.2}Nb_{0.2}Ta_{0.2}Ti_{0.2}W_{0.2})Si_2$. *J Materiomics* 2019, **5**: 337–343.

[375] Chen XQ, Wu YQ. High-entropy transparent fluoride laser ceramics. *J Am Ceram Soc* 2020, **103**: 750–756.

[376] Yan XL, Constantin L, Lu YF, *et al*. $(Hf_{0.2}Zr_{0.2}Ta_{0.2}Nb_{0.2}Ti_{0.2})C$ high-entropy ceramics with low thermal conductivity. *J Am Ceram Soc* 2018, **101**: 4486–4491.

[377] Tallarita G, Licheri R, Garroni S, *et al*. Novel processing route for the fabrication of bulk high-entropy metal diborides. *Scripta Mater* 2019, **158**: 100–104.

[378] Zhou JY, Zhang JY, Zhang F, *et al*. High-entropy carbide: A novel class of multicomponent ceramics. *Ceram Int* 2018, **44**: 22014–22018.

[379] Feng L, Fahrenholtz WG, Hilmas GE. Two-step synthesis process for high-entropy diboride powders. *J Am Ceram Soc* 2020, **103**: 724–730.

[380] Feng L, Fahrenholtz WG, Hilmas GE. Processing of dense high-entropy boride ceramics. *J Eur Ceram Soc* 2020, **40**: 3815–3823.

[381] Chicardi E, García-Garrido C, Gotor FJ. Low temperature synthesis of an equiatomic $(TiZrHfVNb)C_5$ high entropy carbide by a mechanically-induced carbon diffusion route. *Ceram Int* 2019, **45**: 21858–21863.

[382] Sedegov A, Vorotilo S, Tsybulin V, *et al*. Synthesis and study of high-entropy ceramics based on the carbides of refractory metals. *IOP Conf Ser*: *Mater Sci Eng* 2019, **558**: 012043.

[383] Li F, Lu Y, Wang XG, *et al*. Liquid precursor-derived high-entropy carbide nanopowders. *Ceram Int* 2019, **45**: 22437–22441.

[384] Feng L, Fahrenholtz WG, Hilmas GE, *et al*. Synthesis of single-phase high-entropy carbide powders. *Scripta Mater* 2019, **162**: 90–93.

[385] Feng L, Fahrenholtz WG, Hilmas GE. Low-temperature sintering of single-phase, high-entropy carbide ceramics. *J Am Ceram Soc* 2019, **102**: 7217–7224.

[386] Monteverde F, Saraga F, Gaboardi M. Compositional disorder and sintering of entropy stabilized (Hf, Nb, Ta, Ti, Zr)B_2 solid solution powders. *J Eur Ceram Soc* 2020, **40**: 3807–3814.

[387] Gild J, Kaufmann K, Vecchio K, *et al*. Reactive flash spark plasma sintering of high-entropy ultrahigh temperature ceramics. *Scripta Mater* 2019, **170**: 106–110.

[388] Zhang Y, Jiang ZB, Sun SK, *et al*. Microstructure and mechanical properties of high-entropy borides derived from boro/carbothermal reduction. *J Eur Ceram Soc* 2019, **39**: 3920–3924.

[389] Chen L, Wang K, Su WT, *et al*. Research progress of transition metal non-oxide high-entropy ceramics. *J Inorg Mater* 2020, **35**: 748–758.

[390] Wang K, Chen L, Xu CG, *et al*. Microstructure and mechanical properties of (TiZrNbTaMo)C high-entropy ceramic. *J Mater Sci Technol* 2020, **39**: 99–105.

[391] Qin M, Gild J, Wang HR, *et al*. Dissolving and stabilizing soft WB_2 and MoB_2 phases into high-entropy borides via boron-metals reactive sintering to attain higher hardness. *J Eur Ceram Soc* 2020, **40**: 4348–4353.

[392] Gild J, Wright A, Quiambao-Tomko K, *et al*. Thermal conductivity and hardness of three single-phase high-entropy metal diborides fabricated by borocarbothermal reduction and spark plasma sintering. *Ceram Int* 2020, **46**: 6906–6913.

[393] McClane DL, Fahrenholtz WG, Hilmas GE. Thermal properties of $(Zr,TM)B_2$ solid solutions with TM = Hf, Nb, W, Ti, and Y. *J Am Ceram Soc* 2014, **97**: 1552–1558.

[394] Wuchina E, Opeka M, Causey S, *et al*. Designing for ultrahigh-temperature applications: The mechanical and thermal properties of HfB_2, HfC_x, HfN_x and Hf(N). *J Mater Sci* 2004, **39**: 5939–5949.

[395] Wei XF, Liu JX, Bao WC, *et al*. High-entropy carbide ceramics with refined microstructure and enhanced thermal conductivity by the addition of graphite. *J Eur Ceram Soc* 2021, **41**: 4747–4754.

[396] Backman L, Gild J, Luo J, *et al*. Part I: Theoretical predictions of preferential oxidation in refractory high entropy materials. *Acta Mater* 2020, **197**: 20–27.

[397] Wang HX, Cao YJ, Liu W, *et al*. Oxidation behavior of $(Hf_{0.2}Ta_{0.2}Zr_{0.2}Ti_{0.2}Nb_{0.2})C$–$x$SiC ceramics at high temperature. *Ceram Int* 2020, **46**: 11160–11168.

[398] Ye BL, Wen TQ, Liu D, *et al*. Oxidation behavior of $(Hf_{0.2}Zr_{0.2}Ta_{0.2}Nb_{0.2}Ti_{0.2})C$ high-entropy ceramics at 1073–1473 K in air. *Corros Sci* 2019, **153**: 327–332.

[399] Cai FY, Ni DW, Chen BW, *et al*. Fabrication and properties of $C_f/(Ti_{0.2}Zr_{0.2}Hf_{0.2}Nb_{0.2}Ta_{0.2})C$–SiC high-entropy ceramic matrix composites via precursor infiltration and pyrolysis. *J Eur Ceram Soc* 2021, **41**: 5863–5871.